

**MASS DIFFUSION AND CHEMICAL KINETIC DATA FOR  
JET FUEL SURROGATES**

by

Kyungchan Chae

A dissertation submitted in partial fulfillment  
of the requirements for the degree of  
Doctor of Philosophy  
(Mechanical Engineering)  
in the University of Michigan  
2010

Doctoral Committee:

Associate Professor Angela Violi, Chair  
Professor Margaret S. Wooldridge  
Associate Professor Hong G. Im  
Associate Professor Christian M. Lastoskie  
Research Fellow Paolo Elvati

***Success is a journey not a destination.***

***The way you react to change will greatly affect your trip.***

Erik Olesen

***One who fears failure limits its activities.***

***Failure is only the opportunity to begin again more intelligently.***

Henry Ford

© Kyungchan Chae

2010

## **Acknowledgements**

First of all, I would like to express my deepest appreciation to Professor Angela Violi for giving me a wonderful chance to work on new scientific research and for the knowledgeable advice.

I also would like to thank my doctoral committee members, Professor Margaret S. Wooldridge, Professor Hong G. Im, Professor Christian M. Lastoskie and Dr. Paolo Elvati.

The advice from Dr. Elvati on my thesis was invaluable. I am really grateful for his help.

The help from all former and current group members, Dr. Steve Fiedler, Dr. Seungho Choi, Dr. Lam Huynh, Dr. Wendung Hsu, Dr. Hairong Tao, Dr. Soumik Banerjee, Seung-hyun Chung, Kuang-chuan Lin, Jason Lai, Adaleena Mookerjee, was indispensable.

All of my family members gave me their love and support.

Most of all, I would like to express my greatest appreciation to my wife, Soojin Kim. This dissertation would not have been possible without her support and patience.

Finally, I would like to thank Dr. Julian M. Tishkoff and U. S. Air Force Office of Scientific Research for their support and grant for this research.

## Table of Contents

<b>Acknowledgements</b>	ii
<b>List of Figures</b>	vii
<b>List of Tables</b>	xiv
<b>List of Appendices</b>	xv
<b>Abstract</b>	xvi
<b>Chapter</b>	1
<b>1. Introduction</b>	1
1.1 Fuel surrogates	1
1.2 Mass diffusion	4
1.2.1 The effect of mass diffusion on flame modeling	5
1.2.2 Approach for diffusion of polyatomic molecules	7
1.3 Kinetic mechanisms	8
1.4 Outline	10
<b>2. Mutual diffusion coefficients of hydrocarbons in nitrogen</b>	13
2.1 Investigation of mass diffusion	13
2.1.1 Gas kinetic theory	13

2.1.2	Green-Kubo formula and MD simulations	17
2.2	Computational method: Molecular Dynamics simulations	19
2.2.1	All-atom Force field	19
2.2.2	Potential model	21
2.2.3	Simulation method	23
2.2.4	The effect of the thermostat	23
2.2.5	Velocity correlation	26
2.3	Benchmark of computational approaches	27
2.3.1	The effect of system size	27
2.3.2	The effect of concentration	28
2.3.3	Validity of atomistic force field for high temperature gas mixture	29
2.4	Diffusion coefficients of heptane isomers	31
2.4.1	Configurations of heptane isomers	31
2.4.2	Simulation results	32
2.5	Diffusion coefficients of hydrocarbon molecules	39
2.5.1	Linear alkanes	40
2.5.2	Cycloalkanes	44
2.5.3	Aromatic molecules	48
2.6	Comparison with gas kinetic theory	56
2.6.1	Thermodynamic properties and potential parameters	57

2.6.2	Linear alkanes	57
2.6.3	Cycloalkanes	60
2.6.4	Aromatic molecules	61
2.7	The effect of molecular configurations	63
2.7.1	Linear alkanes	65
2.7.2	Cycloalkanes	68
2.7.3	Aromatic molecules	70
2.8	Conclusions	72
<b>3.</b>	<b>The equivalent single body potentials of polyatomic molecules</b>	<b>74</b>
3.1	The effect of potentials on diffusion	74
3.2	Thermodynamic properties from MD simulations	75
3.2.1	Chemical potentials	76
3.2.2	Simulation method	79
3.2.3	Equilibrium vapor pressure and densities	82
3.2.4	Computed thermodynamic properties	85
3.3	Equivalent single body potentials of all atom potentials	86
3.4	Comparison with the C-E equation and MD simulations	87
3.4.1	Linear alkanes	87
3.4.2	Cycloalkanes	91
3.4.3	Aromatic molecules	92

3.5 Conclusions	94
<b>4. Breakdown mechanisms of Decalin</b>	96
4.1 Decalin	96
4.2 Computational method	98
4.2.1 Electronic structure calculations	98
4.2.2 Reaction rates	98
4.3 Reaction pathways	100
4.3.1 Carbon – carbon bond cleavage reactions	101
4.3.2 Hydrogen abstraction reactions	102
4.3.3 Reaction pathways from 1-decalyl radical	103
4.3.4 Reaction pathways from 2-decalyl radical	110
4.3.5 Reaction pathways from 9-decalyl radical	112
4.4 Kinetic modeling	115
4.5 Conclusions	117
<b>5. Conclusions</b>	118
<b>Appendices</b>	122
<b>References</b>	152



## List of Figures

<b>Figure 2.1</b> Comparison of velocity auto-correlation functions of $n\text{-C}_7\text{H}_{16}$ with NVE and NVT ensembles with 1.0 ps coupling parameter at 1 atm and (a) 500K, (b) 1000K. ....	25
<b>Figure 2.2</b> Normalized velocity correlation functions of $n\text{-C}_7\text{H}_{16}$ in the mixture at 1 atm and (a) 500K, (b) 1000K. ....	26
<b>Figure 2.3</b> Mutual diffusion coefficients of $n\text{-C}_7\text{H}_{16}/\text{N}_2$ mixtures at 1 atm for different system sizes with error bars obtained from MD simulations.....	27
<b>Figure 2.4</b> Mutual diffusion coefficients of $n\text{-C}_3\text{H}_8/\text{N}_2$ and $n\text{-C}_4\text{H}_{10}/\text{N}_2$ mixture at 1 atm (MD: Molecular Dynamics simulations, EXP: experiment).....	30
<b>Figure 2.5</b> Molecular configurations of the six heptane isomers.....	32
<b>Figure 2.6</b> Radial distribution functions of $n\text{-C}_7\text{H}_{16}/\text{N}_2$ mixture at 500K, 1 atm.....	33
<b>Figure 2.7</b> Mutual diffusion coefficients of heptane isomers in nitrogen with error bars at two different temperatures and 1 atm: Isomers – (1: $n\text{-C}_7\text{H}_{16}$ , 2: $2\text{-C}_7\text{H}_{16}$ , 3: $2,2\text{-C}_7\text{H}_{16}$ , 4: $2,3\text{-C}_7\text{H}_{16}$ , 5: $3,3\text{-C}_7\text{H}_{16}$ , 6: $2,2,3\text{-C}_7\text{H}_{16}$ ) .....	35

<b>Figure 2.8</b> Mutual diffusion coefficients of heptane isomers in nitrogen versus the square inverse of radius of gyration ( $R_g$ ) of the isomers at 1 atm and (a) 500K and (b) 1000K.....	37
<b>Figure 2.9</b> Mutual diffusion coefficients of three heptane isomers in nitrogen as a function of temperature at 1 atm. Symbols: MD results; Curves: least mean square curve fittings of MD results.....	39
<b>Figure 2.10</b> Mutual diffusion coefficients of linear alkanes in nitrogen at 1 atm as a function of temperature. The curves correspond to the least mean square curve fittings of MD results. ....	40
<b>Figure 2.11</b> Mutual diffusion coefficients of linear alkanes in nitrogen at 1 atm, scaled with $1/T^{1.5}$ to remove the temperature effect.....	41
<b>Figure 2.12</b> Self diffusion coefficients of (a) linear alkanes and (b) nitrogen in the mixtures, at 1atm. The curves correspond to the least mean square curve fittings of MD results.....	43
<b>Figure 2.13</b> Mutual diffusion coefficients of cycloalkanes in nitrogen as a function of temperature, at 1 atm. ....	45
<b>Figure 2.14</b> Self diffusion coefficients of (a) cycloalkanes and (b) nitrogen in the mixtures, at 1 atm. The curves correspond to the least square curve fittings of MD results.....	46

<b>Figure 2.15</b> Mutual diffusion coefficients of normal alkanes ( $C_7H_{16} \sim C_{14}H_{30}$ ) and cycloalkanes ( $C_7H_{14} \sim C_{14}H_{28}$ ) in nitrogen, 1 atm. The curves correspond to the least square curve fittings of MD results.....	47
<b>Figure 2.16</b> Mutual diffusion coefficients of aromatic molecules in nitrogen as a function of temperature, at 1 atm. The curves correspond to the least mean square curve fittings of MD results.....	50
<b>Figure 2.17</b> Self diffusion coefficients of (a) aromatic molecules and (b) nitrogen in the mixtures, at 1 atm. The curves correspond to the least mean square curve fittings of MD results. ....	51
<b>Figure 2.18</b> Mutual diffusion coefficients of isomers of aromatic hydrocarbons in nitrogen, at 1 atm (a) two ring aromatic molecules (b) four ring aromatic molecules. ....	53
<b>Figure 2.19</b> Mutual diffusion coefficients of aromatic isomers in nitrogen at 1000K, 1 atm versus their eccentricity of (a) two ring aromatics and (b) four ring aromatics. ....	55
<b>Figure 2.20</b> Mutual diffusion coefficients of linear alkanes in nitrogen as a function of temperature, at 1 atm obtained from the C-E equation.....	58
<b>Figure 2.21</b> Comparison of mutual diffusion coefficients of (a) $C_2H_6/N_2$ , (b) $C_6H_{14}/N_2$ , (c) $C_{12}H_{26}/N_2$ , and (d) $C_{16}H_{34}/N_2$ , at 1 atm (MD: Molecular dynamics simulations, C-E: the Chapman-Enskog equation). ....	59

<b>Figure 2.22</b> Mutual diffusion coefficients of cycloalkanes in nitrogen as a function of temperature, at 1 atm obtained from the C-E equation.....	60
<b>Figure 2.23</b> Comparison of mutual diffusion coefficients of (a) C <sub>7</sub> H <sub>14</sub> /N <sub>2</sub> and (b) C <sub>14</sub> H <sub>28</sub> /N <sub>2</sub> , at 1 atm (MD: Molecular dynamics simulations, C-E: Chapman-Enskog equation).....	61
<b>Figure 2.24</b> Mutual diffusion coefficients of aromatic molecules in nitrogen as a function of temperature at 1 atm obtained from the C-E equation.....	62
<b>Figure 2.25</b> Comparison of mutual diffusion coefficients of (a) C <sub>6</sub> H <sub>6</sub> /N <sub>2</sub> and (b) C <sub>18</sub> H <sub>12-a</sub> /N <sub>2</sub> , at 1 atm (MD: Molecular dynamics, C-E: Chapman-Enskog equation). .....	.62
<b>Figure 2.26</b> Collision diameters ( $\sigma_{C-E}$ ) of linear alkanes obtained from the C-E results and relations with average radius of gyrations (R <sub>g</sub> ). .....	65
<b>Figure 2.27</b> New collision diameters ( $\sigma_{MD}$ ) of linear alkanes obtained from MD results and relations with average radius of gyrations (R <sub>g</sub> ). .....	67
<b>Figure 2.28</b> Comparison of collision diameters of linear alkanes obtained from MD and C-E results. Solid and dashed lines represent second-order fitting of $\sigma_{MD}$ and $\sigma_{C-E}$ respectively.....	67
<b>Figure 2.29</b> Comparison of collision diameters of cycloalkanes obtained from MD and C-E results. Solid and dashed lines represent second-order fitting of $\sigma_{MD}$ and $\sigma_{C-E}$ respectively.....	69

<b>Figure 2.30</b> Comparison of collision diameters of linearly configured aromatic molecules obtained from MD and C-E results. Solid and dashed lines represent second-order fitting of $\sigma_{MD}$ and $\sigma_{C-E}$ respectively.....	70
<b>Figure 2.31</b> Comparison of collision diameters of four ring aromatic molecules obtained from MD results. Solid represent second-order fitting of $\sigma_{MD}$ . .....	72
<b>Figure 3.1</b> The change of potential energy of $n\text{-C}_8\text{H}_{18}$ as a function of coupling parameters at 540K and 42.7 kg/m <sup>3</sup> density.....	81
<b>Figure 3.2</b> Estimated error by using block averaging analysis for $\lambda=0.5$ of Figure 3.1. ....	82
<b>Figure 3.3</b> Chemical potential and pressure of octane ( $n\text{-C}_8\text{H}_{18}$ ) computed from MD simulations at 540K.....	83
<b>Figure 3.4</b> Comparison of mutual diffusion coefficients of (a) $\text{C}_2\text{H}_6/\text{N}_2$ , (b) $\text{C}_6\text{H}_{14}/\text{N}_2$ , (c) $\text{C}_{12}\text{H}_{26}/\text{N}_2$ , and (d) $\text{C}_{16}\text{H}_{34}/\text{N}_2$ , at 1 atm (MD: Molecular dynamics, C- $E_{EXP}$ : C-E equation with experiment data, and C- $E_{Equiv}$ : C-E equation with equivalent single body potentials).....	89
<b>Figure 3.5</b> Comparison of collision diameters of linear alkanes obtained from MD, C- $E_{EXP}$ , and C- $E_{Equiv}$ results. Curves represent second-order fitting of $\sigma_{MD}$ , $\sigma_{C-E}$ , and $\sigma_{Equiv}$ respectively. ....	90

<b>Figure 3.6</b> Comparison of mutual diffusion coefficients of (a) $C_7H_{14}/N_2$ and (b) $C_{14}H_{28}/N_2$ , at 1atm (MD: Molecular dynamics, C-E <sub>EXP</sub> : C-E equation with experiment data, and C-E <sub>Equiv</sub> : C-E equation with equivalent single body potentials).....	91
<b>Figure 3.7</b> Comparison of collision diameters of cycloalkanes obtained from MD, C-E <sub>EXP</sub> , and C-E <sub>Equiv</sub> results. Curves represent second-order fitting of $\sigma_{MD}$ , $\sigma_{C-E}$ , and $\sigma_{Equiv}$ respectively. ....	92
<b>Figure 3.8</b> Comparison of mutual diffusion coefficients of (a) $C_6H_6/N_2$ and (b) $C_{18}H_{12-a}/N_2$ , at 1atm (MD: Molecular dynamics, C-E <sub>EXP</sub> : C-E equation with experiment data, and C-E <sub>Equiv</sub> : C-E equation with equivalent single body potentials). .....	93
<b>Figure 3.9</b> Comparison of collision diameters of aromatic molecules obtained from MD, C-E <sub>EXP</sub> , and C-E <sub>Equiv</sub> results. Curves represent second-order fitting of $\sigma_{MD}$ , $\sigma_{C-E}$ , and $\sigma_{Equiv}$ respectively.....	94
<b>Figure 4.1</b> Trans-Decalin.....	96
<b>Figure 4.2</b> Initiation reactions of decalin breakdown mechanisms: (a) carbon - carbon bond cleavage, and (b) hydrogen abstractions.....	101
<b>Figure 4.3</b> Potential energy diagram starting from $C_9 - C_{10}$ bond cleavage reaction. .....	102
<b>Figure 4.4</b> Energy barriers to produce 1-, 2-, and 9-decalyl radicals by hydrogen abstraction reaction.....	103

<b>Figure 4.5</b> Potential energy diagrams for pathways 1 and 2. ....	105
<b>Figure 4.6</b> Potential energy diagrams for pathway 3, 4, and 5. ....	106
<b>Figure 4.7</b> Potential energy diagram for pathway 6. ....	107
<b>Figure 4.8</b> Potential energy diagrams for pathways 7 and 8. ....	108
<b>Figure 4.9</b> Potential energy diagram for pathway 9. ....	109
<b>Figure 4.10</b> Potential energy diagram for pathway 10. ....	111
<b>Figure 4.11</b> Potential energy diagram for pathway 11. ....	112
<b>Figure 4.12</b> Potential energy diagram for pathway 12. ....	113
<b>Figure 4.13</b> Potential energy diagram for pathways 13 and 14. ....	114

## List of Tables

<b>Table 2.1</b> Mutual diffusion coefficients of $n\text{-C}_7\text{H}_{16}/\text{N}_2$ mixture at 1 atm with NVE and NVT ensembles with 1.0 ps coupling parameter.....	24
<b>Table 2.2</b> Mutual diffusion coefficients of $n\text{-C}_7\text{H}_{16}/\text{N}_2$ for different concentrations of $n\text{-C}_7\text{H}_{16}$ (1%, 5%, and 10%) with MD simulations at 1atm.....	29
<b>Table 2.3</b> Thermodynamic factors of six heptane isomers/ $\text{N}_2$ mixtures.....	33
<b>Table 2.4</b> Molecular configurations of studied cycloalkanes. ....	44
<b>Table 2.5</b> Molecular configurations of studied PAHs. ....	49
<b>Table 2.6</b> The contributions of collision diameter and energy well depth to diffusion coefficients of $n\text{-C}_7\text{H}_{16}/\text{N}_2$ mixture when 10% perturbation of $\sigma$ and $\varepsilon$ are exerted .....	64
<b>Table 3.1</b> Comparison of equilibrium vapor pressures ( $P_{sat}$ ), liquid densities ( $\rho_{liq}$ ) and vapor densities ( $\rho_{vap}$ ) of linear alkanes at $P_{sat}$ and different temperatures. $D_v$ denotes the average percentile deviations from experimental values.....	84



## **List of Appendices**

<b>Appendix A. Supplementary tables of chapter 2.....</b>	<b>122</b>
<b>Appendix B. Supplementary tables of chapter 3.....</b>	<b>131</b>
<b>Appendix C. Supplementary tables of chapter 4.....</b>	<b>141</b>

## Abstract

The predictive capability of combustion modeling is directly related to the accuracy of the models and data used for molecular transport and chemical kinetics. In this work, we report on improvements in both categories.

The gas kinetic theory (GKT) has been widely used to determine the transport properties of gas-phase molecules because of its simplicity and the lack of experimental data, especially at high temperatures.

The major focus of this thesis is to determine the transport properties of complex molecules and suggest an alternative way to overcome the limitations of GKT, especially for large polyatomic molecules. We also recommend a correction term to the expression of the diffusion coefficients that allows the expansion of the validity of the GKT to include molecules with complex geometries and systems at high temperatures. We compute the diffusion coefficients for three classes of hydrocarbons (linear alkanes, cycloalkanes and aromatic molecules) using Molecular Dynamics (MD) simulations with all-atom potentials to incorporate the effects of molecular configurations. The results are compared with the values obtained using GKT, showing that the latter theory overestimates the diffusion of large polyatomic molecules and the error increases for molecules of significantly non-spherical shape. A detailed analysis of the relative importance of the potentials

used for MD simulations and the structures of the molecules highlights the importance of the molecular shape in evaluating accurate diffusion coefficients. We also proposed a correction term for the collision diameter used in GKT, based on the radii of gyration of molecules.

In the field of chemical kinetics, we report on the reaction mechanisms for the decomposition of decalin, one of the main components of jet fuel surrogates. We identify fifteen reaction pathways and determine the reaction rates using *ab-initio* techniques and transition state theory. The new kinetic mechanism of decalin is used to study the combustion of decalin showing the importance of the new reactions in predicting combustion products.

# Chapter 1

## Introduction

### 1.1 Fuel surrogates

Computational combustion modeling is an essential tool not only for the prediction of flame characteristics but also for the optimal design of combustors. In the use of combustion modeling, conservation equations of fluid dynamics require mass diffusion coefficients and chemical kinetic mechanisms as an essential input data to investigate complex flame behaviors such as, flame speed, ignition characteristics etc. Therefore, the predictive capability of computational modeling is directly related to the accuracy of diffusion coefficients and kinetic mechanisms not only of fuel components but also of other chemical species produced during combustion.

Jet fuels are chemically complex mixtures that consist of a large variety of molecules with different number of carbons and more than thousands of species.<sup>[1]</sup> In recent years, reaction chemistry models have become more realistic and accurate

to provide insight about complex interactions of reacting flow systems under various temperature conditions. However, as the size of a molecule increases, the number of chemical reactions and species grows rapidly. The size of detailed reaction mechanisms for real fuel components is incredibly large and this complexity requires huge computational resources to solve kinetic problems. Therefore, it is not feasible to consider the reaction mechanisms of each single component of complex fuels. Moreover, the kinetic mechanisms of all fuel components are not well determined and the possible chemical kinetic interactions among them are not clearly understood.

As a result, surrogate fuels composed of well known hydrocarbons, which possess properties similar to those of target fuels, become attractive alternatives for combustion applications.<sup>[2]</sup> Surrogate blends are comprised of a relatively small number (less than ten species) of high purity hydrocarbons. Therefore, using surrogate blends has the advantage of allowing fuel composition to be accurately controlled.<sup>[3, 4]</sup>

The major categories of constituents of jet fuel are alkanes, cycloalkanes (naphthenes), aromatics, and alkenes.<sup>[5]</sup> Alkanes (such as dodecane, tetradecane, and isooctane) are the most abundant components and account for 50 – 60% by volume. Cycloalkanes (such as methylcyclohexane, tetralin, and decalin) and aromatics (such as toluene, xylene, and naphthalene) represent 20 – 30% by volume, and alkenes account for less than 5%.

Simple fuel properties, such as hydrogen/carbon (H/C) ratio, can be readily matched with a single-component surrogate.<sup>[6]</sup> However, other fuel properties, such

as chemical composition, ignition delay, soot formation, and molecular transport properties, usually require more components to be accurately reproduced.<sup>[6]</sup>

Although chemical kinetic mechanisms of hydrocarbons that comprise fuel surrogates have been widely studied,<sup>[7-9]</sup> molecular transport data of those species, especially for hydrocarbons that have large number of atoms, have not yet experienced similar focus. Analytical equations derived from gas kinetic theory are still widely used to compute mass diffusion coefficients for low density gas combustion systems irrespective of the configurations of molecules. Consequently, important questions about mass transport are being raised: How can diffusion coefficients be determined, especially for polyatomic molecules with long chains such as, dodecane ( $C_{12}H_{26}$ )? What is the effect of molecular shapes on diffusion coefficients under high temperature reacting flow conditions? Can gas kinetic theory be used for polyatomic molecules?

Recent advances in computational approaches, especially Molecular Dynamics (MD) simulations, can overcome the problems of analytical approaches in determining transport properties. In MD simulations, the configurations of molecules can be considered by describing bonding and angle interactions of all atoms that comprise polyatomic molecules. Molecular modeling techniques can reveal discrepancy with the gas kinetic theory and provide an explicit way to compute improved diffusion coefficients of polyatomic molecules.

The highlight of this study is twofold: first, we identified correlations between molecular configurations and diffusion coefficients by using MD simulations. Second, we suggested correction factors to gas kinetic theory for

hydrocarbon classes. These corrections will provide a straightforward approach to compute improved diffusion coefficients of large hydrocarbon molecules, as well as new fuel components when both experimental measurement and theoretical analysis are not feasible.

MD simulations will also provide new Lennard-Jones 12-6 potential parameters,  $\sigma$  and  $\epsilon$ , for each molecule, which can be directly applied to gas kinetic theory for diffusion calculations. These parameters will be an improvement upon existing data or will be completely novel for molecules in situations where this information is unavailable.

## **1.2 Mass diffusion**

Transport of macroscopic properties arises as a result of microscopic molecular motions.<sup>[10]</sup> Transport processes occur when non-uniform spatial distribution of macroscopic quantities such as, composition, temperature, and flow velocity perturbs equilibrium states. The results of these molecular transport processes appear as non equilibrium phenomena of mass diffusion, heat conduction, and viscosity at macroscopic level.

For low density gas systems, free molecular motion, where the mean free path of a molecule is much larger than the radius of the molecule, is dominant in flow regions. As a result, molecules move freely and molecular collisions are described by only binary interactions.<sup>[11]</sup> Gas kinetic theory is well established under this condition, for molecules that have spherical structure such as, methane (CH<sub>4</sub>).

Among transport properties, mass diffusion coefficients exert the biggest influence on deciding the characteristics of low density gas combustion systems. Mass diffusion results from the relaxation process of a state perturbed by a concentration gradient, to an equilibrium state. It represents the mobility of each species in fluid flow.<sup>[11]</sup> Diffusion coefficients are expressed by Fick's law of diffusion as:

$$J = D\nabla C \quad (1.1)$$

where  $D$ , the constant of proportionality, is the diffusion coefficient,  $J$  is the mass flux, and  $\nabla C$  is the concentration gradient of a species in a fluid. The diffusion coefficient is a property that related microscopic fluctuations to macroscopic flux and it is generally a function of temperature and density of a fluid.

Diffusion coefficients are essential data to solve the species conservation equation in flame modeling. In general, for a multicomponent combustion system, we can assume that thermal or pressure induced diffusion are negligible.<sup>[12, 13]</sup> Therefore, mass diffusion has a dominant effect on determining the balance among the species in a reacting flow. Specifically, mutual mass diffusion coefficients between nitrogen and fuel components critically influence flame characteristics.

### **1.2.1 The effect of mass diffusion on flame modeling**

Flame modeling requires accurate mass diffusion coefficients over a wide range of temperature and pressure conditions. Although several experiments and



theoretical studies have been reported, most of the measurements were conducted at relatively low temperatures (less than 500K).<sup>[14-20]</sup> Moreover, data on mass diffusion still include considerable uncertainties. Therefore, the range of applicability for combustion modeling is limited.<sup>[21]</sup>

In recent years, numerous theoretical and modeling studies have reported the importance of mass diffusion coefficients in flame modeling.<sup>[22-26]</sup> H<sub>2</sub>/air flame simulations, employing different transport formulations, produced between 15 – 30% difference in predicted extinction strain rates.<sup>[25]</sup> Non-premixed flame modeling of hydrocarbon surrogate fuels reported that the measured extinction strain rates are related to the size and mobility of molecules. As the size of molecules decreases, resistance to extinction strain rate increases.<sup>[1]</sup> Sensitivity analysis of ignition, laminar flame speed and extinction strain rates to diffusion coefficients showed that the sensitivity of diffusion is of the same order or larger than the ones of main chemical reactions such as,  $H+O_2 \rightarrow O+OH$ .<sup>[25, 26]</sup>

Modeling of dodecane (*n*-C<sub>12</sub>H<sub>26</sub>) non-premixed flames showed that the computed extinction strain rates were notably sensitive to the mutual diffusion coefficients of normal dodecane and nitrogen in addition to those of oxygen and nitrogen.<sup>[27]</sup> This result clearly implies that diffusion coefficients of fuel species are critical in deciding extinction characteristics of non-premixed flames.

McEnally et al. studied co-flow laminar non-premixed flames and reported the consumption rate of normal heptanes was slower than that of 2,2,3-trimethylbutane in experiments.<sup>[28]</sup> This result is inconsistent with the main consumption routes for heptanes. Hydrogen abstractions and carbon bond fission

processes should consume 2,2,3-trimethylbutane less rapidly than normal heptanes.<sup>[29]</sup> This inconsistency between the experimental evidence and kinetics was caused by transport properties of the two isomers.

All the above studies show the importance of diffusion coefficients in combustion modeling. However, the results only measured the effect of mass diffusion in a qualitative manner. Those studies employed monatomic sphere model to compute diffusion coefficients of polyatomic molecules in the frame of gas kinetic theory. Moreover, none of these studies reported any method to improve the accuracy of diffusion coefficient for combustion modeling. Therefore, alternative approaches that can overcome the limitations in gas kinetic theory should be proposed to improve predictive capability of combustion modeling and quantify the effect on flame characteristics.

### **1.2.2 Approach for diffusion of polyatomic molecules**

Gas kinetic theory utilizes a critical assumption that all molecules have spherical structures to analyze the dynamics of molecular collisions. This approach is reasonable and produces reliable diffusion coefficients for small molecules such as, methane and nitrogen. However for large polyatomic molecules such as, dodecane and hexadecane, the validity of the assumption is not obvious and needs to be verified. Therefore, the first step to understand the limitations of gas kinetic theory should be the incorporation of the effect of molecular configurations into diffusion calculations by evaluating all interactions among atoms that comprise molecules. Since constituents of hydrocarbon fuels typically have structures which

deviate significantly from sphere, quantification of this effect on diffusion is needed to improve the accuracy of diffusion coefficients.

For this purpose, we computed diffusion coefficients, taking into account detailed molecular configurations, and proposed modifications to the gas kinetic theory, which can be used for low density gas systems. To consider the detailed morphology of molecules, we employed Molecular Dynamics (MD) simulations with all-atom potentials. Atomistic level potentials can explicitly treat all bonding and angle interactions within a molecule, as well as non-bonded interactions between different molecules. As a result, our approaches can overcome the limitations of gas kinetic theory and will provide an explicit way to compute diffusion coefficients of polyatomic molecules.

MD simulations have been widely used to obtain diffusion coefficients of both liquid and gas systems. However, results concerning the applications of MD to high temperature systems have not yet been reported. Hence in this study we computed diffusion coefficients of relatively high temperature gas systems by using MD simulations. This work will produce molecular transport data applicable to combustion modeling.

### **1.3 Kinetic mechanisms**

Chemical kinetic mechanisms have been an essential part of combustion modeling, ranging from simple flame burners to automotive engines and gas turbines for aviation fuel combustion.<sup>[30-33]</sup> Typically, detailed kinetic mechanisms, which consist of thousands of reactions, are too large to be solved in Computational

Fluid Dynamics (CFD) models of real scale reacting flows. Therefore, reduced chemical kinetic mechanisms, such as skeletal mechanisms<sup>[34, 35]</sup>, are still commonly used for all practical combustion modeling. Reduced kinetic models can be obtained from validated detailed kinetic mechanisms to predict a range of experimental data. In other words, reduced models should be optimized based on accurate chemical reaction energies and reaction rates obtained from quantum chemistry technique or experimental approaches. All possible reaction pathways of chemical species should be identified before the reduced kinetic mechanisms are constructed. In recognition of this need, detailed chemical kinetic mechanisms have been developed and evaluated for various hydrocarbon fuel components by using *ab-initio* methods or experimental measurements. Previous research has reported detailed reaction mechanisms of normal alkane groups including *n*-heptane (*n*-C<sub>7</sub>H<sub>16</sub>) and its isomers<sup>[36-38]</sup>; *n*-alkanes from *n*-octane (*n*-C<sub>8</sub>H<sub>18</sub>) to *n*-hexadecane (*n*-C<sub>16</sub>H<sub>34</sub>)<sup>[39]</sup>; aromatics including toluene (C<sub>7</sub>H<sub>8</sub>)<sup>[40]</sup>; and cycloalkanes including cyclohexane (C<sub>6</sub>H<sub>12</sub>)<sup>[33]</sup> and methylcyclohexane (C<sub>7</sub>H<sub>14</sub>)<sup>[41]</sup>. These studies can provide extensive information to build reduced kinetic mechanisms. However, detailed reaction mechanisms of various aromatic molecules and especially cycloalkanes are still less defined and are confined to small molecules because of their complex reaction mechanisms and large number of possible reactions. Therefore, reaction pathways of cycloalkanes should be constructed to improve the capability of predicting combustion chemistry of fuel surrogates.

In recognition of this need, in this study, we will perform the analysis of breakdown mechanisms of decalin (Decahydronaphthalene- C<sub>10</sub>H<sub>18</sub>), a reference

component of multi-ring naphthene classes for jet fuel surrogate, by using Density Functional Theory (DFT) method.

## 1.4 Outline

The objective of this thesis work is to develop a predictive model for the combustion of jet fuels surrogate components. The major body of this study focuses on determining the diffusion properties of complex hydrocarbons over a wide range of temperatures using Molecular Dynamics simulations. Specifically, we will address the effect of molecular structures on diffusion coefficients, and propose implementations to the current models to take into account the geometry of molecules.

In order to implement the kinetics of jet fuel surrogate, we use *ab-initio* methods to determine reaction pathways of cycloalkanes, an important class of compounds in jet fuel surrogates. The reaction model is then compared with experimental data to assess the strength of the model in predicting important combustion properties.

Brief descriptions of each chapter are presented below.

In chapter 2, basic theory of mass diffusion in low density gas conditions is reviewed. A set of mathematical expressions are derived for mutual mass diffusion coefficients in the frame of gas kinetic theory and statistical mechanics. After these short review sections, mutual diffusion coefficients of hydrocarbon molecules in

nitrogen are computed and the effect of molecular configurations is analyzed in the following order.

- First, comparison between MD simulations and available experimental data is conducted to confirm the validity of MD simulations.
- Second, heptane isomers are selected to test the capability of all-atom potentials to capture the effect of molecular structures on diffusion coefficients.
- Third, mutual diffusion coefficients of normal alkanes, aromatic molecules, and cycloalkanes in nitrogen carrier gas are computed with both MD simulations and gas kinetic theory over the temperature range of 500 ~ 1000K and at 1 atm pressure. The results are compared to show deviations caused by using monatomic potentials or all-atom potentials for the same molecules.
- Finally, radius of gyration for target molecules is computed and compared to collision diameters.

Chapter 3 reports on potential approaches that can eliminate the effect that arises from using different potentials. Gas kinetic theory and MD simulations should use potentials that have the same functional form to isolate the effect of molecular configurations on mass diffusion coefficients. For this purpose, new molecular potential parameters for gas kinetic theory were obtained by using atomistic MD simulations.

- First, free energy calculations are conducted to compute chemical potential of liquid and vapor states.
- Second, based on chemical potential and pressure data, thermodynamic properties, such as critical properties and boiling temperatures are estimated.
- Third, the correlation of corresponding state is applied to define new molecular potential parameters from the thermodynamic properties. The comparison is carried out between MD simulations and gas kinetic theory with the molecular potential parameters.
- Finally, we tested the relative contribution of molecular configurations and force field to diffusion coefficients.

Chapter 4 describes the kinetic studies carried out for the cycloalkane class of compounds in jet fuel surrogate. The potential energy surface is explored to investigate the breakdown mechanism of Decalin (Decahydronaphthalene,  $C_{10}H_{18}$ ), a potential candidate of cycloalkane class for jet fuel surrogates. The Density Functional Theory (DFT) method (B3LYP) is used to identify possible reaction pathways. Rice-Ramsperger-Kassel-Marcus (RRKM) and Transition State Theory (TST) are employed to compute high pressure limit reaction rate constants for the identified reaction pathways. A kinetic analysis is also performed for pyrolysis conditions to evaluate the importance of each reaction pathway.

In chapter 5, the highlights of the work are summarized.

## **Chapter 2**

### **Mutual diffusion coefficients of hydrocarbons in nitrogen**

#### **2.1 Investigation of mass diffusion**

The most common approach to investigate the molecular transport of low density gas systems is to use the Boltzmann transport equation of gas kinetic theory. The solution of this transport equation, combined with Lennard-Jones potential parameters, suggests a simple analytical expression for self and mutual diffusion coefficients. This approach has been applied over wide range of flame modeling due to the ease of use even though the theory was developed for only monatomic molecules.<sup>[42]</sup>

##### **2.1.1 Gas kinetic theory**

Polyatomic molecules interact through the potentials between atomic interacting sites located in each molecule. The major difficulties in the analysis of binary collision between these molecules are the existence of inelastic collisions and



the very complicated trajectories associated with angle dependent potentials.<sup>[11]</sup> Kinetic theories for polyatomic gases were derived in three different ways. Taxman suggested the classical kinetic theory.<sup>[42]</sup> Wang Chang and Uhlenbeck developed the semi-classical theory which describes internal quantum states of a molecule as separate chemical species so that the translational motion can be treated classically.<sup>[43]</sup> Waldmann,<sup>[44]</sup> and Snider formulated fully quantum mechanical kinetic theory.<sup>[45]</sup> However, direct application of these theories to compute diffusion coefficients of polyatomic molecules is still too complex because of the difficulties in assessing the dynamics of molecular collisions. Therefore, the analysis of collision dynamics of polyatomic molecules should rely on the approximate method of evaluating collision integrals that contain all of the information about interaction energy related to intermolecular pair potentials and scattering mechanism of molecular collisions.<sup>[11]</sup> The most widely used approximation scheme for evaluating angular dependent interaction for transport properties has been proposed by Mason and Monchick and Mason.<sup>[46]</sup> The authors computed collision integrals with following assumptions:

- 1) Inelastic collisions have little effect on trajectories.

Most inelastic collisions involve the transfer of only one quantum rotational energy and this amount of energy is much less than  $k_B T$ . However the translational kinetic energy is of the order of  $k_B T$ .

- 2) In a given collision only one relative orientation is effective.

Although the potential acts along the whole trajectory, the deflection angle is determined by the interaction in the closest distance of the

colliding molecules. The relative orientation of two colliding molecules does not change substantially.

- 3) Every possible orientation has equal weight
- 4) Quantum effects are neglected

These assumptions make the dynamics of a collision a mathematically manageable problem. The collision integrals for a given pair of molecules are tabulated as a function of the reduced temperature,  $T^*$ . Based on these integrals, the Chapman-Enskog solution to Boltzmann transport equation can give a simple mathematical expression for mutual diffusion coefficients. Hirschfelder et. al. followed the Chapman-Enskog approach, combined with the Lennard-Jones (L-J) 6 - 12 intermolecular potential function, and suggested the Hirschfelder-Bird-Spotz (HBS) equation for mutual mass diffusion coefficients.<sup>[21]</sup>

$$D_{12} = \frac{3}{8} \frac{\sqrt{(k_B T)^3 / (2\pi m_{12})}}{n \sigma_{12}^2 \langle \Omega^{(1,1)*} \rangle} \quad (2.1)$$

where  $k_B$  is the Boltzmann constant;  $T$  is the temperature of a system;  $m_{12}$  is the reduced mass of the pair components;  $n$  is the average number density;  $\sigma_{12}$  is the collision diameter of two species and  $\Omega^{(1,1)*}$  is the collision integral. The collision integral depends on the reduced temperature,  $T^* = k_B T / \varepsilon_{12}$ , where  $\varepsilon_{12}$  is the energy well depth of the intermolecular potentials. The main disadvantage of this equation is the difficulty encountered in evaluating the collision diameter,  $\sigma_{12}$ , and

potential energy well depth,  $\varepsilon_{12}$ . These two parameters are usually obtained from viscosity measurements.<sup>[47]</sup> However, only limited amounts of measurement data are available for polyatomic molecules. Therefore, the correlations of corresponding states of Tee et al. are frequently employed to estimate the parameters for fluids.<sup>[48]</sup>

According to this theory, the volumetric behavior and the intermolecular forces in a fluid can be characterized by critical pressure,  $P_c$ , critical temperature,  $T_c$ , and acentric factor,  $\omega$ , of the fluid. Therefore, the two potential parameters ( $\sigma$  and  $\varepsilon$ ) can be predicted from the three quantities.

$$\sigma \left( \frac{P_c}{T_c} \right)^{1/3} = a_1 + b_1 \omega \quad (2.2)$$

$$\frac{\varepsilon}{k_B T_c} = a_2 + b_2 \omega \quad (2.3)$$

where 'a' and 'b' are empirically derived coefficients and  $\omega$  is an acentric factor that measures non-sphericity of a molecule. The empirical coefficients are derived from the viscosity and second virial coefficient data of 14 substances ranging from inert gases to benzene and normal heptane.

$$a_1 = 2.3551, b_1 = -0.3955, a_2 = 0.8063, b_2 = 0.6802$$

Lee and Kesler developed an analytical correlation, based on the 3-parameter corresponding states principle for the acentric factor,  $\omega$ .<sup>[49]</sup>

$$\omega = \frac{-\ln(P_c) - 5.927 + 6.096/T_{br} + 1.288\ln(T_{br}) - 0.169T_{br}^6}{15.252 - 15.687/T_{br} - 13.472\ln(T_{br}) + 0.436T_{br}^6} \quad (2.4)$$

where  $T_{br} = T_b/T_c$ ,  $T_b$  and  $T_c$  denote boiling and critical temperature respectively. Typically, experimentally measured thermodynamic properties ( $P_c$ ,  $T_c$ , and  $T_b$ ) are used for the above equations. However, the lack of these measurement data makes it possible to apply the Chapman-Enskog (C-E) equation for only limited number of molecules.

Another approach for molecular transport is to use atomistic modeling techniques, such as Molecular Dynamics (MD) simulations. The main advantage of this strategy over gas kinetic theory is that complete atomistic representation of a molecule can be achieved by using molecular configuration data and all-atom potentials. Therefore, MD simulations are especially useful for polyatomic molecules that comprise fuel surrogate blends.

### 2.1.2 Green-Kubo formula and MD simulations

The fluctuation dissipation theorem, which is the basis of linear response theory, suggests an advanced way to express the mass diffusion coefficient.<sup>[50-52]</sup> The mathematical formulation of the theorem is expressed as the Green-Kubo (G-K) relations.<sup>[50]</sup> This formula can determine diffusion coefficients from microscopic fluctuations in systems at the equilibrium state instead of considering non-

equilibrium systems.<sup>[53]</sup> As a result, this approach establishes a theoretical basis for computing mass diffusion coefficients from equilibrium MD simulations.

The G-K formula expresses the self diffusion coefficient as the ensemble average of the velocity auto correlation functions of time. The mutual mass diffusion coefficient is defined as the combination of the ensemble average of velocity auto- and cross-correlation functions of time. The cross correlation terms describe the momentum transfer of a particle through its neighbors.<sup>[54]</sup> The mutual diffusion coefficient is expressed as<sup>[55]</sup>

$$D_{12} = Q \left[ x_2 D_1 + x_1 D_2 + x_1 x_2 \left( \frac{f_{11}}{x_1^2} + \frac{f_{22}}{x_2^2} - 2 \frac{f_{12}}{x_1 x_2} \right) \right] \quad (2.5)$$

$$D_\alpha = \frac{1}{3} \int_0^\infty \langle \vec{u}_i^\alpha(t) \cdot \vec{u}_i^\alpha(0) \rangle dt \quad (2.6)$$

$$f_{\alpha\alpha} = \frac{1}{3} \int_0^\infty \langle \vec{u}_i^\alpha(t) \cdot \vec{u}_j^\alpha(0) \rangle dt \quad (2.7)$$

$$f_{\alpha\beta} = \frac{1}{3} \int_0^\infty \langle \vec{u}_i^\alpha(t) \cdot \vec{u}_j^\beta(0) \rangle dt \quad (2.8)$$

where  $D_\alpha$  is the time integral of velocity auto-correlation functions of species  $\alpha$ ,  $\vec{u}^\alpha$  and  $\vec{u}^\beta$  are the velocity vectors of species  $\alpha$  and  $\beta$ ,  $f_{\alpha\alpha}$  and  $f_{\alpha\beta}$  are the time integrals of velocity cross-correlation function between the same species and between species  $\alpha$  and  $\beta$  respectively.  $x_\alpha$  is the mole fraction of each species, while the angular brackets denote the ensemble average.  $Q$  is a thermodynamic factor related to the compositional derivative of chemical potential and corrects compositional

dependence in diffusion flux.<sup>[56]</sup> The  $Q$  factor can be determined from the integral of the radial distribution functions. For a binary mixture system, the parameter is defined as<sup>[55]</sup>

$$Q = \frac{1}{1 + x_1 x_2 \rho (\Gamma_{11} + \Gamma_{22} - 2\Gamma_{12})} \quad (2.9)$$

$$\Gamma_{\alpha\alpha} = 4\pi \int_0^{\infty} r^2 [g_{\alpha\alpha}(r) - 1] dr \quad (2.10)$$

$$\Gamma_{\alpha\beta} = 4\pi \int_0^{\infty} r^2 [g_{\alpha\beta}(r) - 1] dr \quad (2.11)$$

where  $g_{\alpha\alpha}(r)$  and  $g_{\alpha\beta}(r)$  are the radial distribution functions between same species and between species  $\alpha$  and  $\beta$  respectively.  $\Gamma_{\alpha\alpha}$  and  $\Gamma_{\alpha\beta}$  represent the spatial integrals of the radial distribution functions. For a thermodynamically ideal mixture, defined as the perfectly mixed state of a mixture, the integrals of the radial distribution functions of each species are identical, and  $Q$  can be approximated as unity.<sup>[57]</sup>

## 2.2 Computational method: Molecular Dynamics simulations

### 2.2.1 All-atom Force field

When using Molecular Dynamics (MD) simulations, potential parameters used to describe intermolecular interactions between molecules are critical for

predicting physical and chemical properties. Quantum mechanical approaches can predict intermolecular potentials with accuracy but high computational cost limits their applications to small systems. Therefore, molecular modeling approaches typically employ empirical force fields.

The united atom (UA) model, in which a group of atoms are represented by a single pseudo-atom, is computationally appealing and has been widely used in predicting fluid properties.<sup>[58-60]</sup> However, reported results showed the inadequacy of UA model.<sup>[61, 62]</sup> In those studies, self diffusion coefficients obtained by using the UA model are too large due to the absence of hydrogen bonding and the smoother potential energy surface that results from neglecting hydrogen atoms. The all-atom model can resolve these issues by considering hydrogen atoms of hydrocarbons explicitly and can provide an accurate description of the shape of molecules.

The OPLS AA force field, used in this study, is an empirical all atom force field and can be applied for a wide range of hydrocarbon molecules.<sup>[63]</sup> This force field has been widely used to obtain thermodynamic and transport properties of liquid systems that consist of polyatomic molecules and the results of these studies showed a good agreement with available experimental data.<sup>[64-68]</sup> However, the validity of these potentials for low density gas systems should be addressed. The parameters of OPLS AA potentials were optimized by matching liquid densities and vaporization enthalpies of various hydrocarbon molecules near normal boiling temperatures.<sup>[63]</sup> The accuracy of these parameters for high temperature low density gas systems is still unknown. Therefore, we should test the capability of

OPLS AA parameters, at least for high temperature gas diffusion calculations, by comparison with available experimental data.

### 2.2.2 Potential model

The OPLS AA force field utilizes the Lennard-Jones (L-J) 12-6 potential model for determining interatomic interactions between two atoms.

$$u_{ij}(r) = 4\varepsilon_{ij} \left[ \left( \frac{\sigma_{ij}}{r} \right)^{12} - \left( \frac{\sigma_{ij}}{r} \right)^6 \right] \quad (2.11)$$

where  $r$  is the distance between two atoms;  $\sigma_{ij}$  represents a separation distance at which potential energy becomes zero;  $\varepsilon_{ij}$  is the energy well depth of L-J potentials. The interactions for unlike molecules are computed by using Lorentz-Berthelot combining rules.<sup>[69, 70]</sup>

$$\sigma_{ij} = \frac{1}{2}(\sigma_i + \sigma_j) \quad \varepsilon_{ij} = \sqrt{\varepsilon_i \varepsilon_j} \quad (2.12)$$

All molecules were treated as fully flexible by allowing bond stretching and angle vibration, as well as the change of torsion angle. Bond stretching and angle vibration were represented by harmonic potentials



$$V_{bond} = \frac{1}{2}k_b (r - r_0)^2 \quad (2.13)$$

$$V_{angle} = \frac{1}{2}k_\theta (\theta - \theta_0)^2 \quad (2.14)$$

where  $V_{bond}$  and  $V_{angle}$  denote bond and angle potentials respectively;  $k_b$  and  $k_\theta$  represent force constants for bending and angle interactions;  $r_0$  and  $\theta_0$  are equilibrium distance and angle. Ryckaert-Bellemans function was used for the description of torsional energy.

$$V_{torsion} = \sum_{n=0}^5 C_n (\cos \varphi)^n \quad (2.15)$$

where  $C_n$  are coefficients and  $\varphi$  is dihedral angle. Torsional potential is coupled with 1 – 4 nonbonded interactions and will change conformational energy profiles. Therefore, a scaling factor of 0.5 was used for 1 – 4 nonbonded interactions to prevent a change of energy profile.

Interatomic interactions were truncated with the cut off distance of 18Å and long-range corrections for energy and pressure were considered during the simulations. Electrostatic interactions were computed with the same cutoff distance of 18 Å based on the distance between two charge groups.

$$V_{elec} = \frac{q_i q_j}{4\pi\epsilon_0 r} \quad (2.16)$$

where  $q$  is partial charge of an atom and  $\epsilon_0$  is the permittivity of vacuum.

### **2.2.3 Simulation method**

Simulations were conducted in the temperature range of 500 ~ 1000K and 1 atm pressure. The initial position of each atom is achieved by placing them arbitrary position in a simulation box and the initial velocity of each atom was generated with a Maxwellian distribution at a give temperature. Total simulation time was 14ns and velocity components of each atom were recorded every 50 time steps. The force acting on each atom was calculated with Newton's equation of motion and given force field. To integrate the equation of motion, the verlet leapfrog numerical algorithm was used with a time step of 1.0 fs. All MD simulations were carried out with the GROMACS software packages.<sup>[71]</sup>

In defining system sizes, we used experimentally measured densities at each temperature and utilized periodic boundary conditions of cubic box. The canonical ensemble (NVT) was obtained by employing a global Nose-Hoover global thermostat.<sup>[72, 73]</sup>

### **2.2.4 The effect of the thermostat**

Nose-Hoover thermostat controls temperature by expanding phase space with scaled momentum.<sup>[74]</sup> The velocity components of particles can be perturbed by this scaling method. Therefore, computing transport properties requires a very weak perturbation so that the thermostat exerts negligible influence on the final

results. Studies of self and binary diffusion coefficients of pure liquids such as  $N_2$ ,  $CO_2$ ,  $C_2H_6$ , and  $C_2H_4$  showed that the Nose-Hoover global thermostat did not influence significantly the values of diffusion coefficients.<sup>[75]</sup> However, the effect of thermostat on transport properties in high temperature gas systems has not been addressed. Therefore, we compared the results of NVE ensemble with those of NVT ensemble to identify the effect of the thermostat on diffusion coefficients. Normal heptane and nitrogen ( $n-C_7H_{16}/N_2$ ) mixtures were used and simulations were performed at two different temperature conditions (500K and 1000K) as the strength of the temperature coupling varies. The coupling strength of the Nose-Hoover global thermostat is expressed with the period of the oscillations of kinetic energy between the systems and the reservoir. Short oscillation times produce strong coupling and vice versa.

Table 2.1 Mutual diffusion coefficients of  $n-C_7H_{16}/N_2$  mixture at 1 atm with NVE and NVT ensembles with 1.0 ps coupling parameter.

Temp.	$D_{12}$ [ $cm^2/s$ ]	
	NVT	NVE
500K	$0.172 \pm 0.005$	$0.173 \pm 0.007$
1000K	$0.557 \pm 0.013$	$0.558 \pm 0.016$

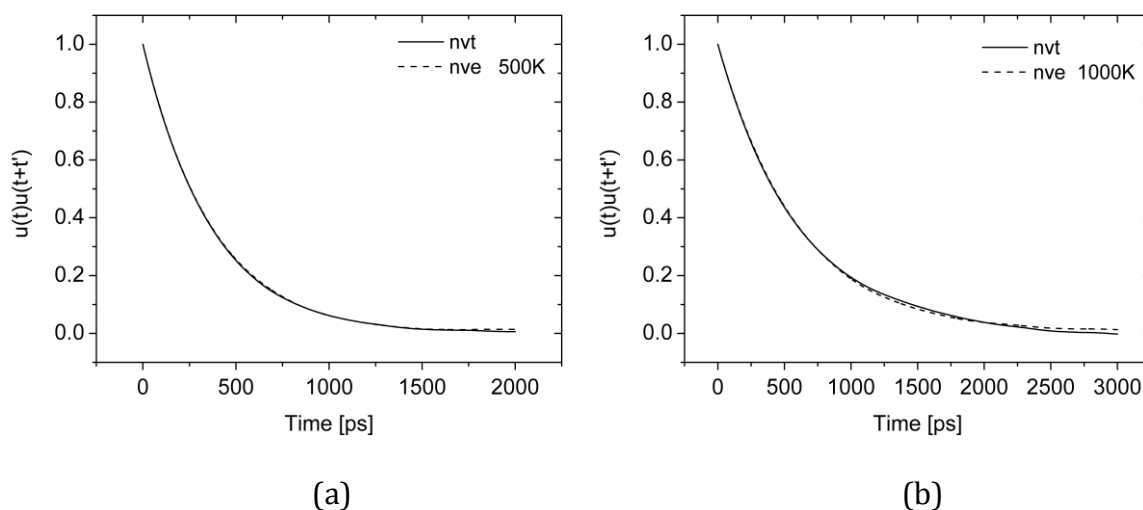


Figure 2.1 Comparison of velocity auto-correlation functions of  $n\text{-C}_7\text{H}_{16}$  with NVE and NVT ensembles with 1.0 ps coupling parameter at 1 atm and (a) 500K, (b) 1000K.

As shown in Table 2.1, the deviations between the two ensembles are less than 1% of the computed diffusion coefficients. Figure 2.1 also demonstrates that velocity correlation functions are well matched with each other. In Table 2.1 and Figure 2.1, we reported results obtained by using 1.0 ps coupling parameter but we tested different coupling values in the range of 1.0 – 100.0 ps. These calculations showed that the deviations were less than 1% irrespective of the applied coupling parameters. Based on these results, we concluded that the Nose-Hoover global thermostat has negligible effect on diffusion coefficients of the high temperature gas systems considered in this study and subsequently we justified the use of the NVT ensemble to obtain target temperatures in all simulations.

### 2.2.5 Velocity correlation

Figure 2.2 illustrates that the velocity was sufficiently decorrelated within 3 ns in the temperature range considered. However we used longer relaxation time (7 ns) for our calculations to improve the statistical accuracy in the tail region. Typically longer relaxation time is required for polyatomic molecules than monatomic molecules because the translational and vibrational motions have different relaxation time. Our simulation results showed that 7 ns relaxation time was adequate for the complete decay of the correlation functions.

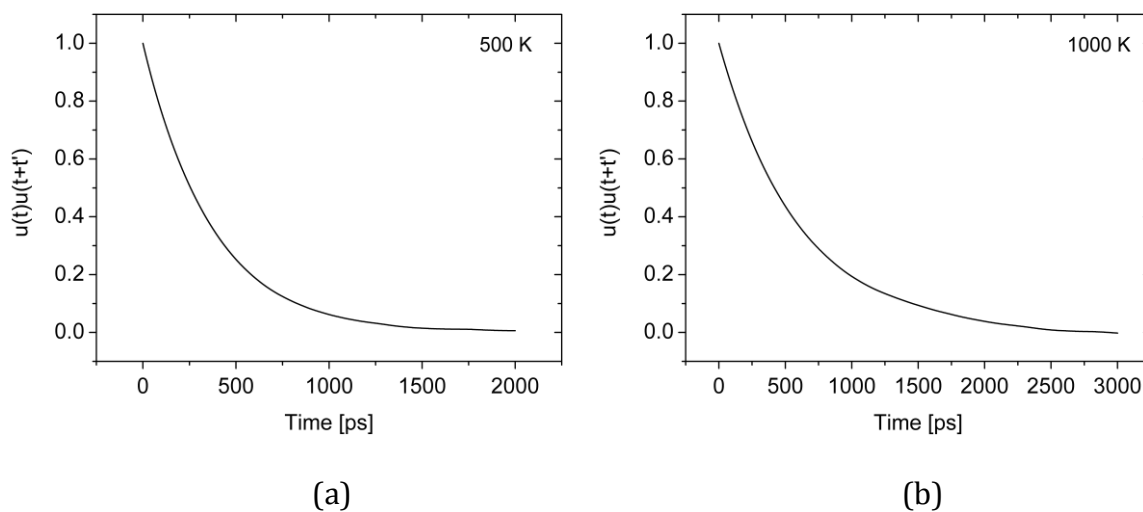


Figure 2.2 Normalized velocity correlation functions of  $n\text{-C}_7\text{H}_{16}$  in the mixture at 1 atm and (a) 500K, (b) 1000K.

## 2.3 Benchmark of computational approaches

### 2.3.1 The effect of system size

Four systems that have different numbers of molecules were simulated to test the effect of system size on diffusion coefficients. Figure 2.3 and Table A.1 in the Appendix A show computed mutual diffusion coefficients of normal heptane and nitrogen ( $n\text{-C}_7\text{H}_{16}/\text{N}_2$ ) mixtures at 500 and 1000K. The error bars in Figure 2.3 represent standard deviations.

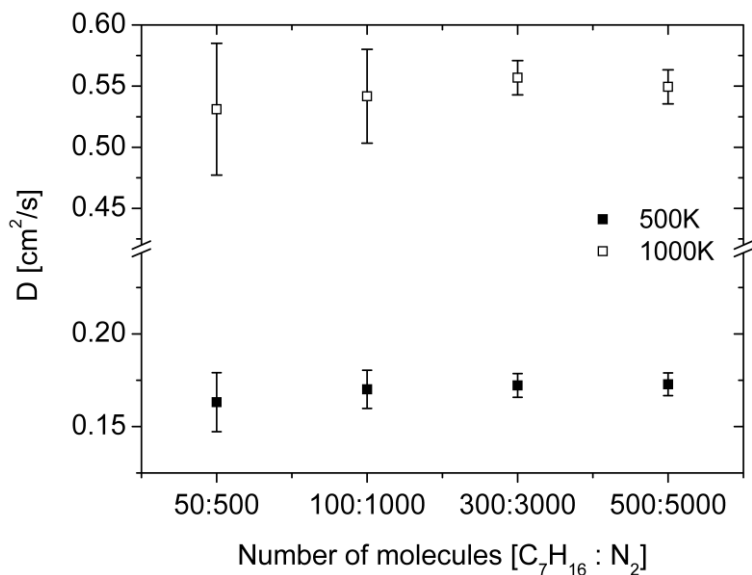


Figure 2.3 Mutual diffusion coefficients of  $n\text{-C}_7\text{H}_{16}/\text{N}_2$  mixtures at 1 atm for different system sizes with error bars obtained from MD simulations.

The maximum differences among the four mixtures are around 5% at the both temperatures. When considering the error ranges, we can conclude that all of the testing systems produced very similar diffusion coefficients. However, Figure 2.3 illustrates that system B (1100 molecules) has much larger statistical error compared with that of system C (3300 molecules) or D (5500 molecules), especially at high temperature (1000K). Although, system D showed slightly better results than system C, we decided system C as the basis size for all our simulations due to the compromise between the accuracy and computational cost.

### 2.3.2 The effect of concentration

In principle, mutual diffusion coefficients of ideal gas systems are independent of relative concentration of each species. Therefore, the Chapman-Enskog (C-E) equation (equation 2.1), derived from gas kinetic theory, does not include any concentration dependent variables.

To evaluate the effect of concentration on diffusion, we analyzed 1%, 5%, and 10% mole fractions of  $n\text{-C}_7\text{H}_{16}$  in the mixtures. We limited the mole fraction of hydrocarbons at 10% because one of the main goals of this study is to compute mutual diffusion coefficients for systems relevant to combustion applications. In general combustion conditions, fuel concentrations for stoichiometric condition are very low compared to those of nitrogen.

Table 2.2 shows mutual diffusion coefficients of  $n\text{-C}_7\text{H}_{16}/\text{N}_2$  mixture at different concentration ratios. This result confirms that MD simulations also

produce diffusion coefficients that are independent of the mole fractions of each species in a low density gas, consistent with standard gas kinetic theory.

Table 2.2 Mutual diffusion coefficients of  $n\text{-C}_7\text{H}_{16}/\text{N}_2$  for different concentrations of  $n\text{-C}_7\text{H}_{16}$  (1%, 5%, and 10%) with MD simulations at 1atm.

Temp.	$D_{12}$ [ $\text{cm}^2/\text{s}$ ]		
	1%	5%	10%
500K	$0.172 \pm 0.006$	$0.173 \pm 0.007$	$0.172 \pm 0.005$
1000K	$0.564 \pm 0.017$	$0.558 \pm 0.013$	$0.557 \pm 0.012$

### 2.3.3 Validity of atomistic force field for high temperature gas mixture

Since the OPLS AA potential parameters were optimized at normal boiling temperature, direct application of this force field to different temperature conditions cannot guarantee the accuracy of computed diffusion coefficients. Therefore, comparison with available experimental data is needed to identify the validity of the potentials under such conditions. However, only small amount of experimental data are available for mutual diffusion coefficients of high temperature gas systems especially for hydrocarbon/ $\text{N}_2$  mixtures. Consequently, we chose  $n\text{-C}_3\text{H}_8/\text{N}_2$  and  $n\text{-C}_4\text{H}_{10}/\text{N}_2$  systems for our test simulations.



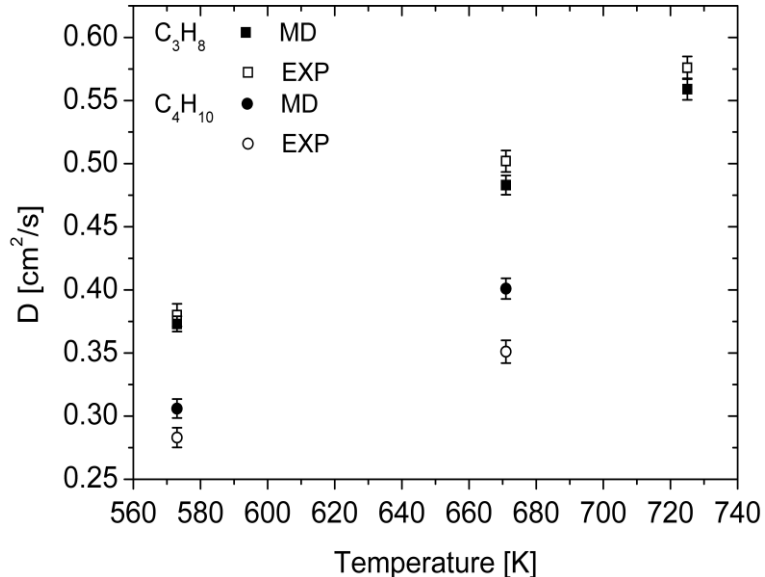


Figure 2.4 Mutual diffusion coefficients of  $n\text{-C}_3\text{H}_8/\text{N}_2$  and  $n\text{-C}_4\text{H}_{10}/\text{N}_2$  mixture at 1 atm (MD: Molecular Dynamics simulations, EXP: experiment).

For  $n\text{-C}_3\text{H}_8/\text{N}_2$  mixture, simulation results show better agreement with experimental results (around 3% deviations) than  $n\text{-C}_4\text{H}_{10}/\text{N}_2$  mixture (around 10% deviations). Since  $n\text{-C}_3\text{H}_8/\text{N}_2$  results were recently measured data that utilized the reverse-flow gas chromatographic technique,<sup>[76]</sup> we surmise that they are more accurate than experimental results of  $n\text{-C}_4\text{H}_{10}/\text{N}_2$  mixture reported around 30 years ago.<sup>[16]</sup> However, when considering the reported uncertainty of the experimental measurements (around 3%),<sup>[76]</sup> we concluded that MD results were in a reasonable agreement with experimental data. Consequently, we believe that the OPLS AA force field can produce reliable diffusion coefficients for the high temperature (500K ~ 1000K) gas systems considered in this study, at 1 atm pressure. Moreover, the goal

of this study is to identify the effect of molecular shapes on mass diffusion coefficients and assess the validity of gas kinetic theory for polyatomic molecules rather than compute exact diffusion values. Therefore, we concluded that the above comparison demonstrated the validity of the use of the OPLS AA potentials for the goal of this study. Further results of calculations are listed in Table A.2 in the Appendix A.

## **2.4 Diffusion coefficients of heptane isomers**

### **2.4.1 Configurations of heptane isomers**

Although all-atom force field can describe molecular structures, we need to clarify the effectiveness of these potentials in capturing the difference in the configurations of molecules. For this purpose, we computed diffusion coefficients for the mixtures of nitrogen and six heptane isomers. Since all isomers have the same mass, deviations in computed diffusion coefficients among isomers originate entirely from their structural differences. Moreover, the structural differences are quite subtle so we expect that only a small amount of variance will manifest in final diffusion values. Capturing these small discrepancies will verify the validity of our approach to address the effect of molecular structures on mass diffusion coefficients.

Molecular configurations of the 6 heptane isomers are listed in Figure 2.5: normal heptane ( $n\text{-C}_7\text{H}_{16}$ ) a linear chain molecule, 2-methylhexane ( $2\text{-C}_7\text{H}_{16}$ ), 2,2-dimethylpentane ( $2,2\text{-C}_7\text{H}_{16}$ ), 2,3-dimethylpentane ( $2,3\text{-C}_7\text{H}_{16}$ ), 3,3-dimethylpentane

(3,3-C<sub>7</sub>H<sub>16</sub>), and 2,2,3-trimethylbutane (2,2,3-C<sub>7</sub>H<sub>16</sub>) which has an approximately spherical shape due to its high branching.

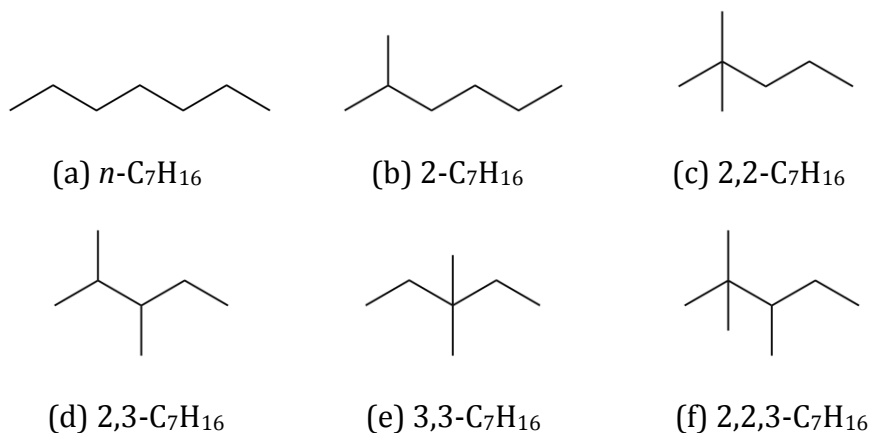


Figure 2.5 Molecular configurations of the six heptane isomers.

#### 2.4.2 Simulation results

In using the Green-Kubo formula (equation 2.5), we assumed the thermodynamic factor,  $Q$ , is unity. In order to validate this assumption, we computed the radial distribution functions (RDF) for the six heptane isomer systems and obtained thermodynamic factors. Figure 2.6 plots the computed RDFs of *n*-C<sub>7</sub>H<sub>16</sub>/N<sub>2</sub> mixture at 500K and 1atm. The shapes of RDFs of the six isomers match almost exactly. Consequently, the values of the thermodynamic factors are in the range of 0.9990 – 0.9993 for the temperature range considered (see Table 2.3).

This result reveals conventional characteristics of high temperature low density gas mixtures. A system in a low density has very large mean free path between particles so that the distributions of molecules are very similar irrespective

of molecular structures and sizes. Under this condition, a binary system typically makes a homogeneous mixture. As a result, the spatial integrals of the three RDFs in equation 2.9 generate very similar values each other and the Q factor becomes unity.

Table 2.3 Thermodynamic factors of six heptane isomers/ $N_2$  mixtures.

Mixture	Q
$n\text{-C}_7\text{H}_{16}/N_2$	0.9990
$2\text{-C}_7\text{H}_{16}/N_2$	0.9991
$2,3\text{-C}_7\text{H}_{16}/N_2$	0.9993
$2,3\text{-C}_7\text{H}_{16}/N_2$	0.9991
$3,3\text{-C}_7\text{H}_{16}/N_2$	0.9990
$2,2,3\text{-C}_7\text{H}_{16}/N_2$	0.9990

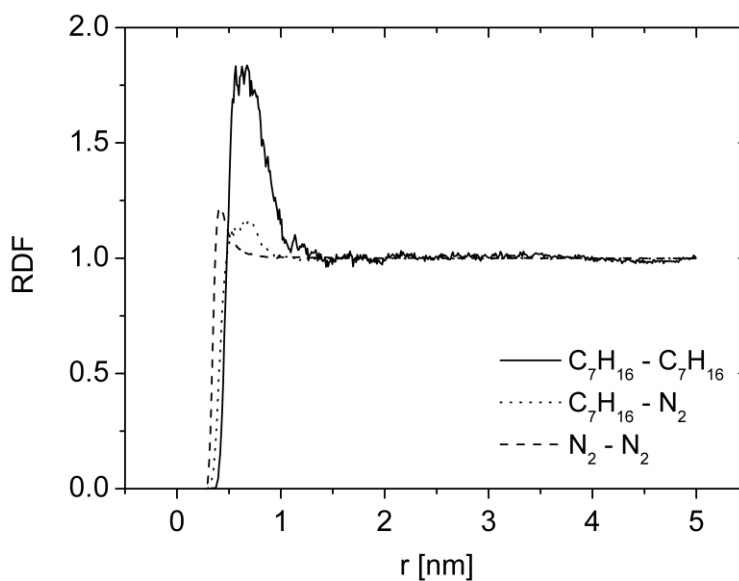
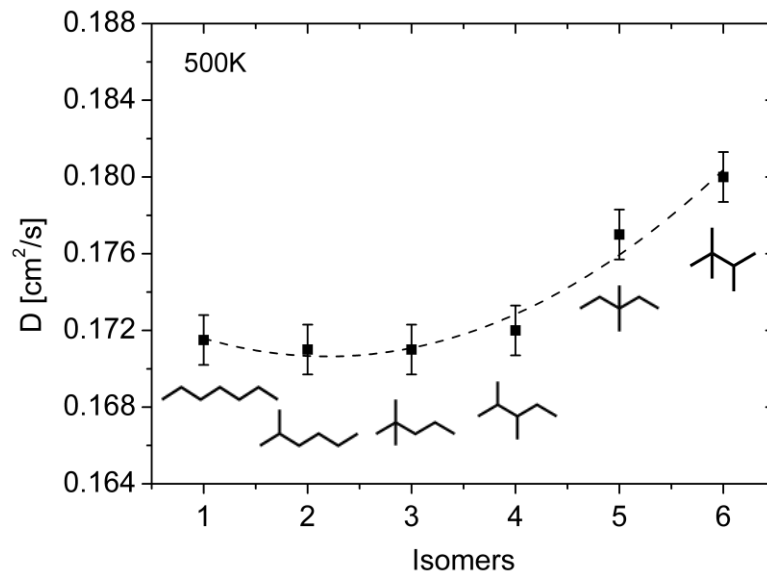
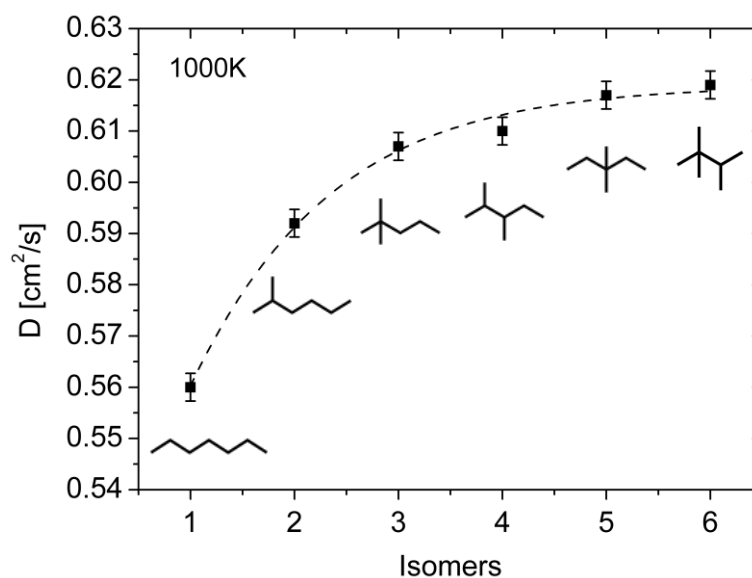


Figure 2.6 Radial distribution functions of  $n\text{-C}_7\text{H}_{16}/N_2$  mixture at 500K, 1 atm.

Figure 2.7 shows the distribution of diffusion coefficients of the isomers at 500K and 1000K. The differences in diffusion coefficients are small at low temperature and increase with temperature. The results illustrate that as the number of alkyl branches increases, the corresponding diffusion coefficients increase. Experimental work on heptane isomers/helium mixtures also reported the same trends of isomer diffusions. Eli Grushka et al.<sup>[77, 78]</sup> showed that heptane isomers that have larger number of alkyl branches produced higher diffusion coefficients. The consistency of these results justifies that our approach is able to reproduce the experimental measurement correctly.



(a)



(b)

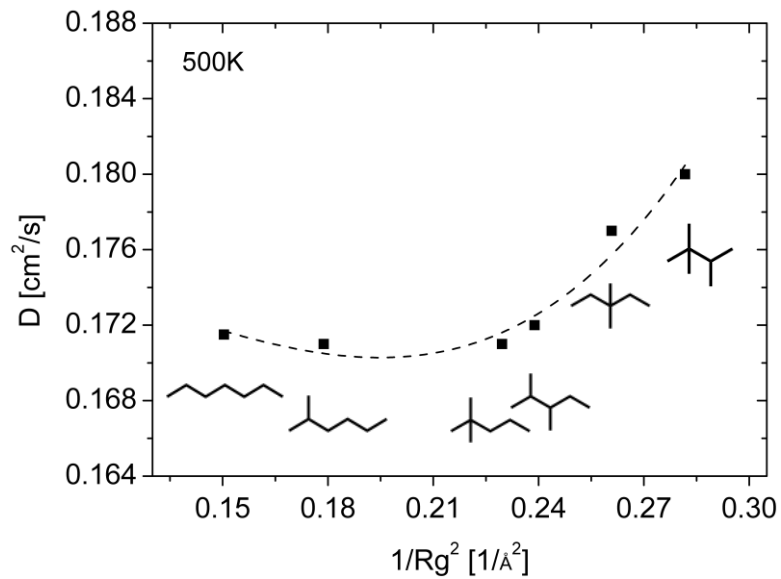
Figure 2.7 Mutual diffusion coefficients of heptane isomers in nitrogen with error bars at two different temperatures and 1 atm: Isomers - (1: *n*-C<sub>7</sub>H<sub>16</sub>, 2: 2-C<sub>7</sub>H<sub>16</sub>, 3: 2,2-C<sub>7</sub>H<sub>16</sub>, 4: 2,3-C<sub>7</sub>H<sub>16</sub>, 5: 3,3-C<sub>7</sub>H<sub>16</sub>, 6: 2,2,3-C<sub>7</sub>H<sub>16</sub>)

The above results illustrate that the number of methyl branches and their relative locations in a molecule changes the overall molecular configurations and these structural variations affect diffusion values. To identify these effects, we computed radius of gyrations (Rg) of heptane isomers and investigated the relation between diffusion coefficients and molecular configurations. The radius of gyration of a molecule describes the overall spread of atoms and represents their equilibrium conformations. Therefore, it has been used as geometric factors for various polyatomic molecules.<sup>[79-81]</sup> In this study, we computed the radius of gyrations from the following relation:

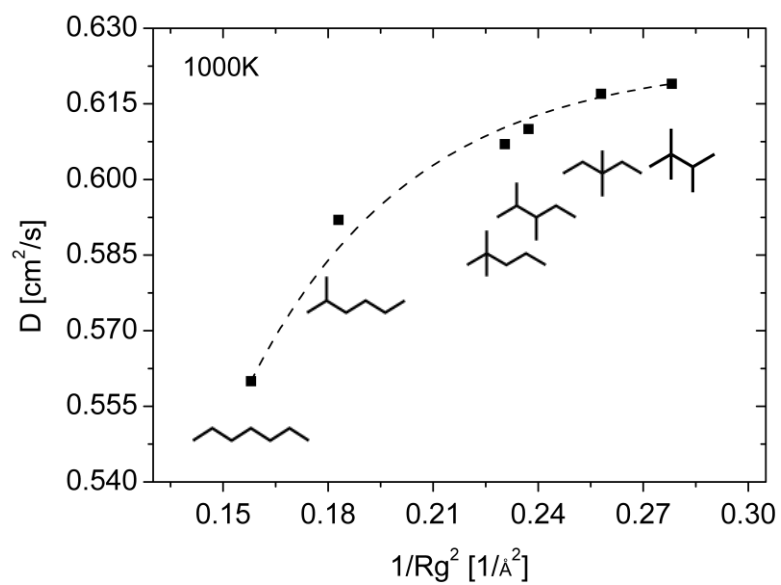
$$Rg = \sum_{\alpha=1}^3 I_{\alpha\alpha} \quad (2.17)$$

where  $I_{\alpha\alpha}$  denotes the moment of inertia of principal axes.

Since, in gas kinetic theory, a diffusion coefficient is proportional to the square inverse of a collision diameter ( $\sigma$ ), a geometric factor of a molecule, we used the square inverse of radius of gyrations (Rg) for comparison. Figure 2.8 shows that Rg explains the trends of diffusion coefficients of heptane isomers (Figure 2.7). As Rg decreases, diffusion coefficients increase and a collision diameter has the same effect on diffusion coefficients in gas kinetic theory.



(a)



(b)

Figure 2.8 Mutual diffusion coefficients of heptane isomers in nitrogen versus the square inverse of radius of gyrations ( $Rg$ ) of the isomers at 1 atm and (a) 500K and (b) 1000K.



The above result implies that  $R_g$  can be related to a collision diameter and can be used as a geometric factor that explains the trends of diffusion values. Figure 2.8 also reveals that as the number of methyl branches increases, the collision diameter (or  $R_g$ ) decreases and, consequently, a diffusion coefficient increases.

To address the temperature dependence of diffusion coefficients, we plotted the results in the temperature range considered (See Figure 2.9). In Figure 2.9, only three isomers are presented for clarity of the plot. Experimental measurement of mutual diffusion coefficients for gas mixtures at 1 atm showed that measured values had the following form<sup>[76, 82]</sup>

$$D_{12} = AT^n \quad (2.18)$$

where  $A$  and  $n$  are fitting constant and  $T$  is the temperature of the system. Therefore, we will express diffusion coefficients in the same way by fitting our results with equation 2.18 through least mean square fitting procedure.

The mixture of 2,2,3- $C_7H_{16}/N_2$  has the highest mass diffusivities among isomers in all temperature due to the smallest collision diameter (or  $R_g$ ) and  $n$ - $C_7H_{16}/N_2$  has the lowest diffusion coefficients. More results about all other isomers are listed in Table A.3 in the Appendix A.

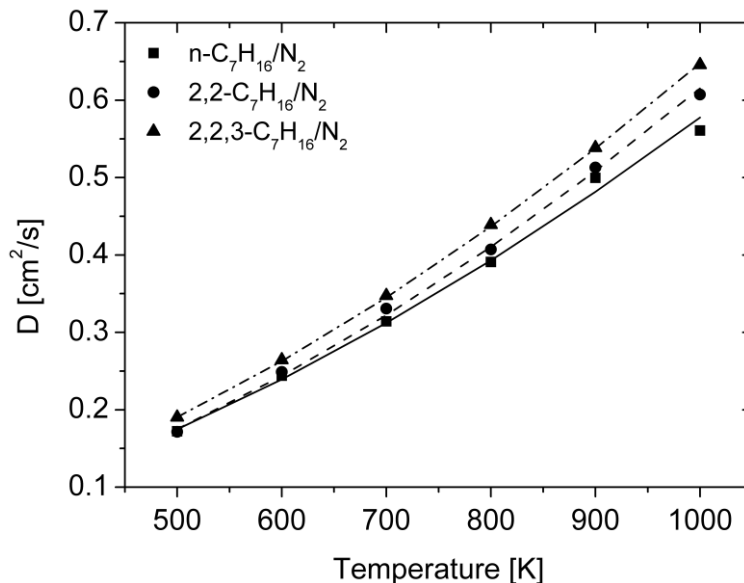


Figure 2.9 Mutual diffusion coefficients of three heptane isomers in nitrogen as a function of temperature at 1 atm. Symbols: MD results; Curves: least mean square curve fittings of MD results.

## 2.5 Diffusion coefficients of hydrocarbon molecules

In the previous section we verified our approaches to identify the effect of molecular configurations on diffusion coefficients with heptane isomers. In this section, we computed mutual diffusion coefficients of hydrocarbons in nitrogen mixtures. Hydrocarbon classes considered in this study are linear alkanes, cycloalkanes, and aromatic molecules, which typically constitute conventional transportation fuels or fuel surrogates. For each mixture, the results of five simulations were averaged in order to increase statistical accuracy of velocity correlations.

### 2.5.1 Linear alkanes

Linear alkanes are the most abundant constituents in conventional hydrocarbon fuels and are typically employed as representative fuel components for conventional combustion modeling. In this study, we selected sixteen linear alkanes (from methane,  $\text{CH}_4$  to hexadecane,  $\text{C}_{16}\text{H}_{34}$ ) to identify the effect of the length of linear molecules on diffusion coefficients.

MD results are presented in Figure 2.10. As the number of methyl groups increases, the diffusion coefficients decrease and the equation 2.18 successfully describes the temperature dependency of diffusion coefficients. Detailed results of all linear alkanes are listed in Table A.4 in the Appendix A.

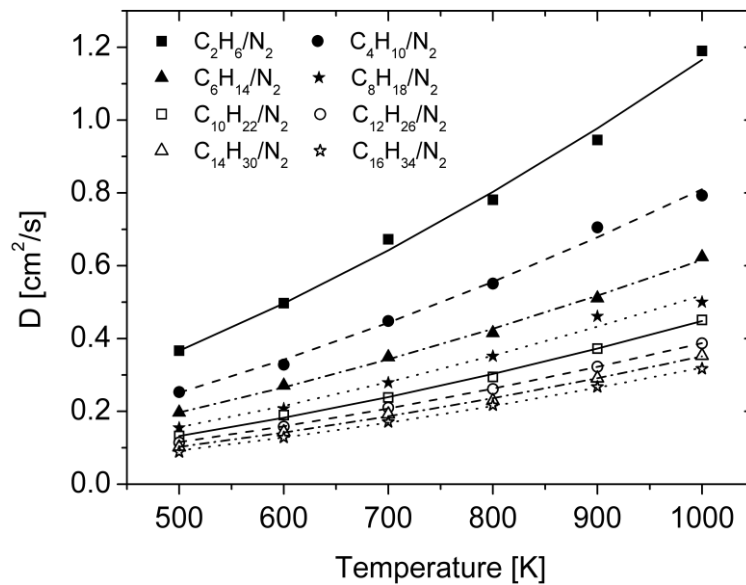


Figure 2.10 Mutual diffusion coefficients of linear alkanes in nitrogen at 1 atm as a function of temperature. The curves correspond to the least mean square curve fittings of MD results.

Figure 2.10 reveals that the difference in diffusion coefficients among mixtures becomes larger as temperature increases. This trend implies that the difference in diffusion coefficients of Figure 2.10 results from the coupling effect of mass, molecular configuration, and temperature (T). Therefore, we removed the temperature effect by dividing the computed diffusion coefficients by the factor of  $T^{1.5}$  because diffusion coefficients are proportional to  $T^{1.5}$  in an ideal gas. This result was plotted in Figure 2.11 and the curves show that the difference in diffusion values are very similar irrespective of temperature. Since the mass of a molecule is independent of temperature, we conclude that the effect of molecular configurations on diffusion coefficients is almost independent of temperature for target systems.

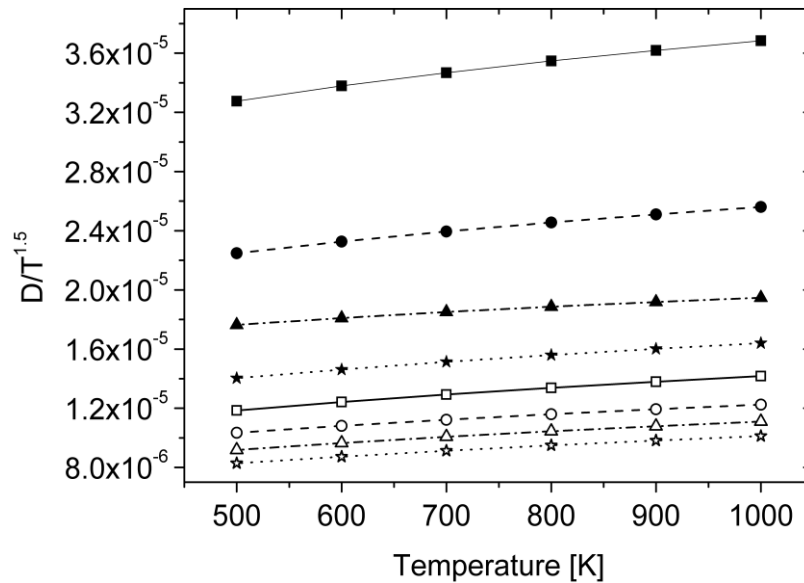
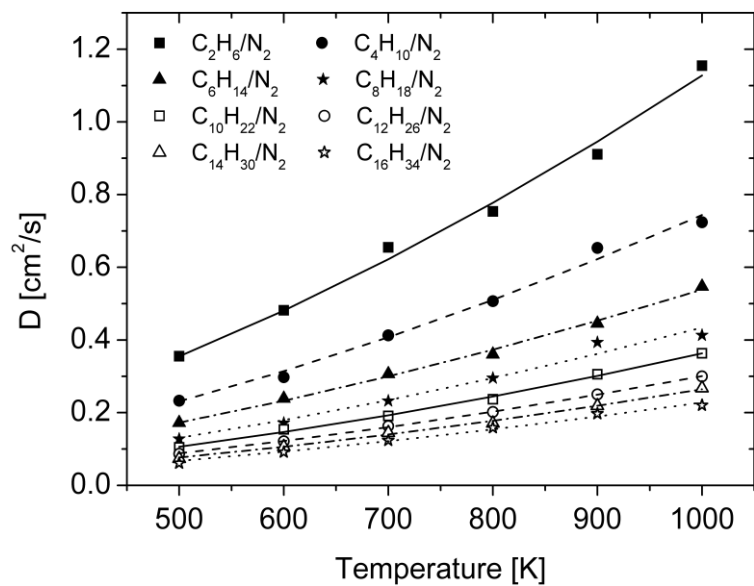


Figure 2.11 Mutual diffusion coefficients of linear alkanes in nitrogen at 1 atm, scaled with  $1/T^{1.5}$  to remove the temperature effect.

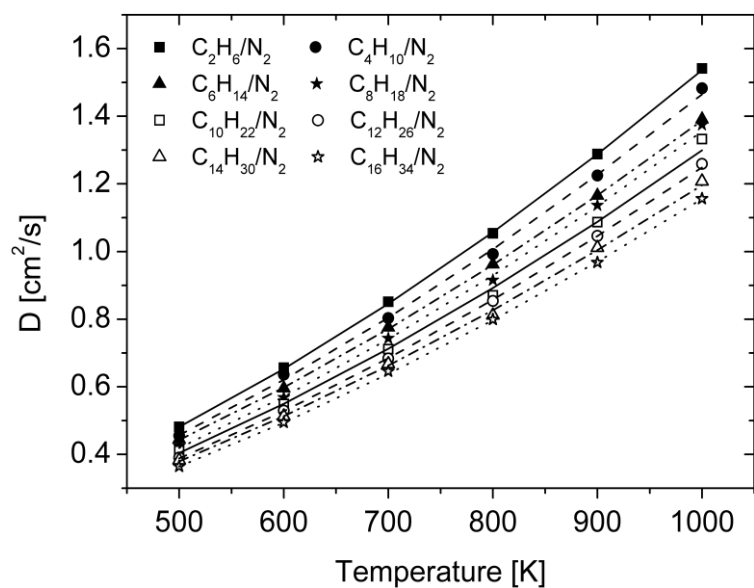
Another advantage of using MD simulations over gas kinetic theory to study mass diffusion is the ability to determine the self diffusion coefficient of each component in mixtures. Figure 2.12 reports the self-diffusion coefficients of normal alkanes and nitrogens in each system. The results reveal that unlike nitrogen (Figure 2.12 (b)), the diffusion coefficients of linear alkanes (Figure 2.12 (a)) show significant variations among the studied systems.

Mutual diffusion coefficients are computed from the summation of two velocity auto-correlation terms of each species and three velocity cross-correlation terms (equation 2.5). Our results showed that the cross-correlation terms accounted for negligible portions (less than 1%) of the diffusion values. Therefore, the mutual diffusion coefficients depend on only self diffusion coefficients of two species and their mole fractions (equation 2.19). Equation 2.19 also confirms that a species of smaller mole fraction has a dominant effect on deciding diffusion coefficients. As a result, the trends in self diffusion coefficients of linear alkanes (Figure 2.12 (a)) are very similar to those of mutual diffusion coefficients (Figure 2.10).

$$D_{12} = x_{nitrogen} D_{alkanes} + x_{alkanes} D_{nitrogen} \quad (2.19)$$



(a)



(b)

Figure 2.12 Self diffusion coefficients of (a) linear alkanes and (b) nitrogen in the mixtures, at 1atm. The curves correspond to the least mean square curve fittings of MD results.

## 2.5.2 Cycloalkanes

Cyclohexanes with methyl branches have recently been employed as important constituents of jet fuel surrogates.<sup>[83]</sup> In this study, we computed diffusion coefficients for this cycloalkane group to address the effect of the length of methyl branches on diffusion values. Table 2.4 lists the configurations of the cycloalkanes considered in this study.

Table 2.4 Molecular configurations of studied cycloalkanes.

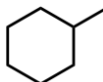
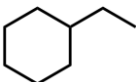
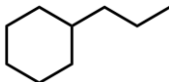
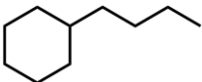
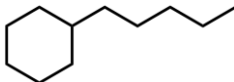
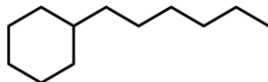
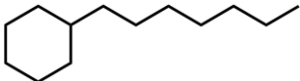
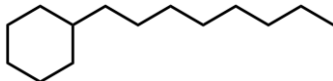
Molecules	
 Methylcyclohexane(C <sub>7</sub> H <sub>14</sub> )	 Ethylcyclohexane(C <sub>8</sub> H <sub>16</sub> )
 Propylcyclohexane(C <sub>9</sub> H <sub>18</sub> )	 Butylcyclohexane(C <sub>10</sub> H <sub>20</sub> )
 Pentylcyclohexane(C <sub>11</sub> H <sub>22</sub> )	 Hexylcyclohexane(C <sub>12</sub> H <sub>24</sub> )
 Heptylcyclohexane(C <sub>13</sub> H <sub>26</sub> )	 Octylcyclohexane(C <sub>14</sub> H <sub>28</sub> )

Figure 2.13 reports mutual diffusion coefficients computed from MD simulations and Figure 2.14 (a) shows the self diffusion coefficients of cycloalkanes, which is dominant to those of nitrogen (Figure 2.14 (b)) in determining the values of mutual diffusion coefficients. All the results of cycloalkanes are listed in Table A.5 in the Appendix A.

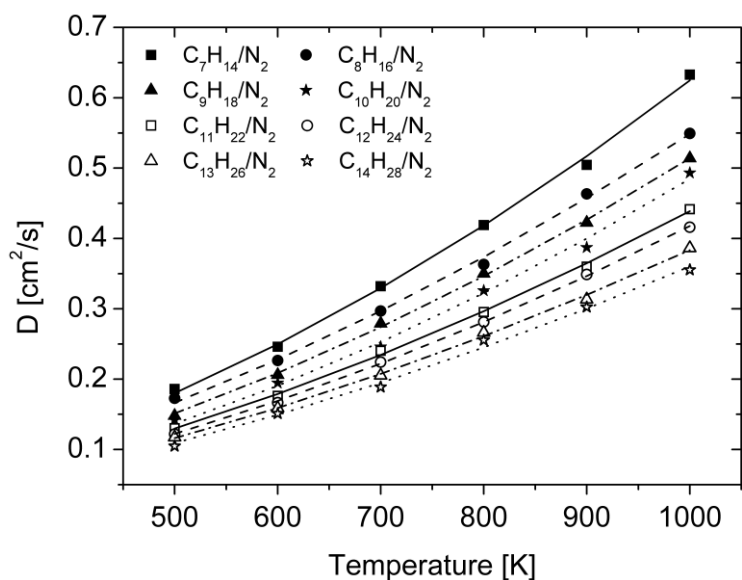
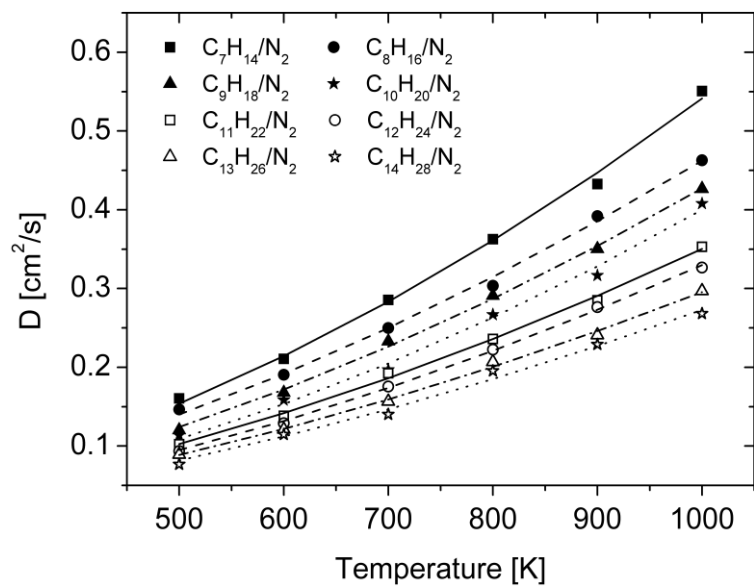
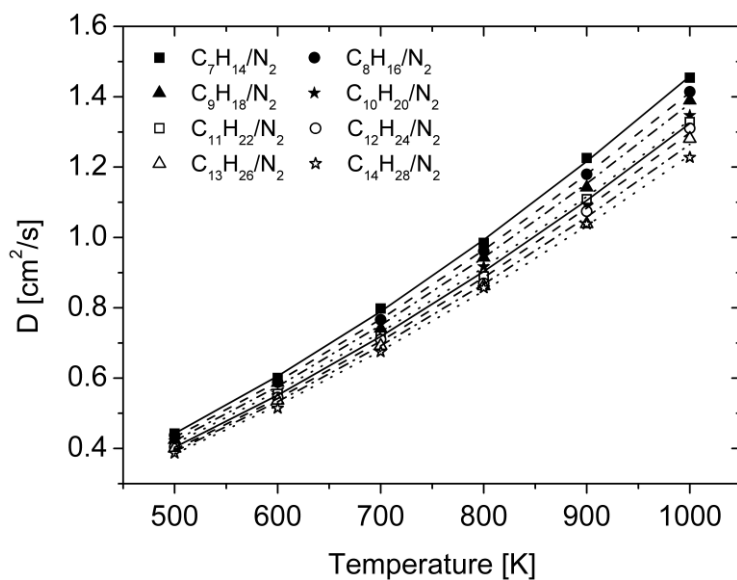


Figure 2.13 Mutual diffusion coefficients of cycloalkanes in nitrogen as a function of temperature, at 1 atm.





(a)



(b)

Figure 2.14 Self diffusion coefficients of (a) cycloalkanes and (b) nitrogen in the mixtures, at 1 atm. The curves correspond to the least square curve fittings of MD results.

The above cycloalkane series has similarity in variation of their configurations to those of linear alkanes. To show this trend, we compared the change of diffusion coefficients as additional methyl groups are added sequentially both to linear alkanes and to cyclohexanes (Figure 2.15). This result shows that the contributions of an additional methyl group to diffusion coefficients for both groups are very similar. The shift in the two curves is related to the presence of the six-member aliphatic ring in cycloalkanes. The constrained arrangement of the aliphatic ring has much smaller deformation than linear alkanes. As a result, cycloalkanes have smaller effective area and consequently, produce higher diffusion coefficients.

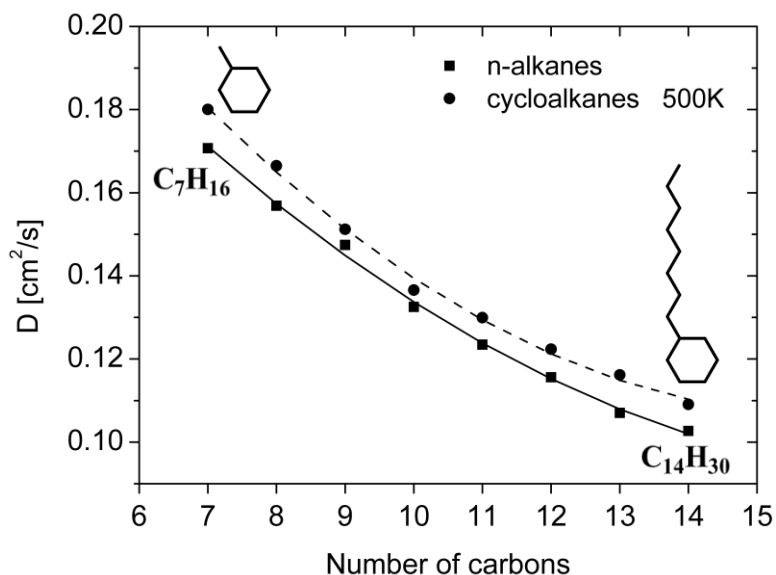

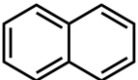
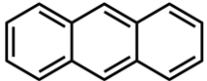
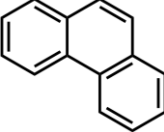
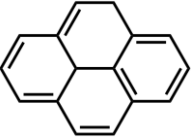
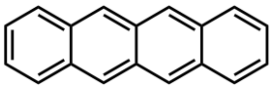
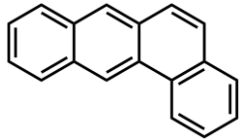
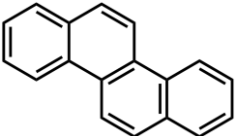
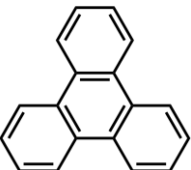


Figure 2.15 Mutual diffusion coefficients of normal alkanes ( $C_7H_{16} \sim C_{14}H_{30}$ ) and cycloalkanes ( $C_7H_{14} \sim C_{14}H_{28}$ ) in nitrogen, 1 atm. The curves correspond to the least square curve fittings of MD results.

### 2.5.3 Aromatic molecules

Aromatic hydrocarbons are usually regarded as important precursors for soot formation.<sup>[84, 85]</sup> Moreover, benzene and naphthalene are frequently employed as representative aromatic compounds in jet fuel surrogate blends.<sup>[5]</sup> In this study, we computed mutual diffusion coefficients for polycyclic aromatic hydrocarbons (PAH) in nitrogen, from one-ring to four-ring aromatic molecules (Table 2.5).

Table 2.5 Molecular configurations of studied PAHs.

structure	Molecules
One-ring	 Benzene (C <sub>6</sub> H <sub>6</sub> )
Two-ring	 Naphthalene (C <sub>10</sub> H <sub>8</sub> )
Three-ring	<div style="display: flex; justify-content: space-around; align-items: center;"> <div style="text-align: center;">             Anthracene (C<sub>14</sub>H<sub>10</sub>-a)         </div> <div style="text-align: center;">             Phenanthrene (C<sub>14</sub>H<sub>10</sub>-b)         </div> </div>
Four-ring	<div style="text-align: center;">             Pyrene (C<sub>16</sub>H<sub>10</sub>)         </div>
	<div style="display: flex; justify-content: space-around; align-items: center;"> <div style="text-align: center;">             Naphthacene (C<sub>18</sub>H<sub>12</sub>-a)         </div> <div style="text-align: center;">             Benz[a]Anthracene (C<sub>18</sub>H<sub>12</sub>-b)         </div> </div>
	<div style="display: flex; justify-content: space-around; align-items: center;"> <div style="text-align: center;">             Chrysene (C<sub>18</sub>H<sub>12</sub>-c)         </div> <div style="text-align: center;">             Triphenylene (C<sub>18</sub>H<sub>12</sub>-d)         </div> </div>

The results show very similar trends to those of the other two hydrocarbon groups reported in the previous sections. Aromatic molecules are the main cause of the variations in the mutual diffusion coefficients. As the number of aromatic rings increases, diffusion coefficients decrease. Figure 2.16 and 2.17 show mutual and self diffusion coefficients of each species respectively. Results of all aromatic mixtures are listed in Table A.6 in the Appendix A.

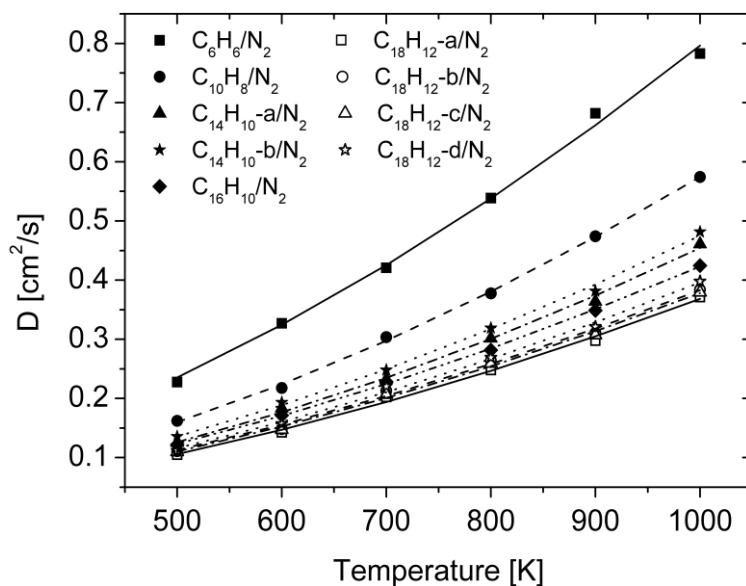
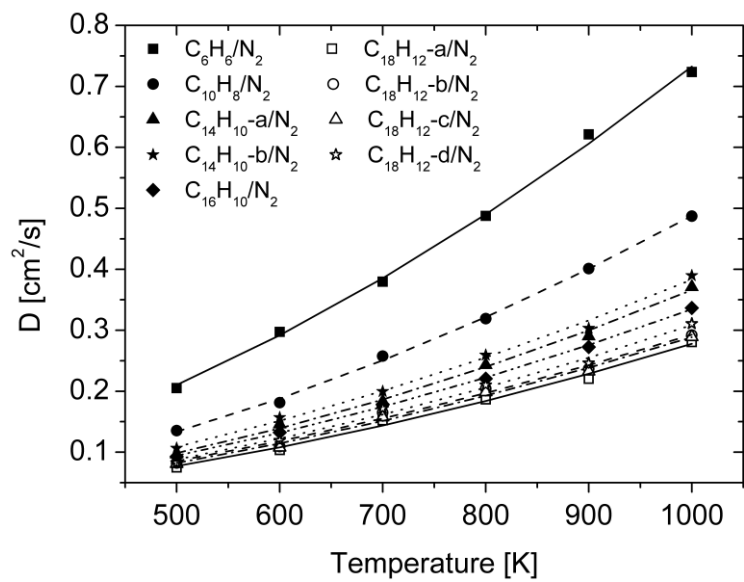
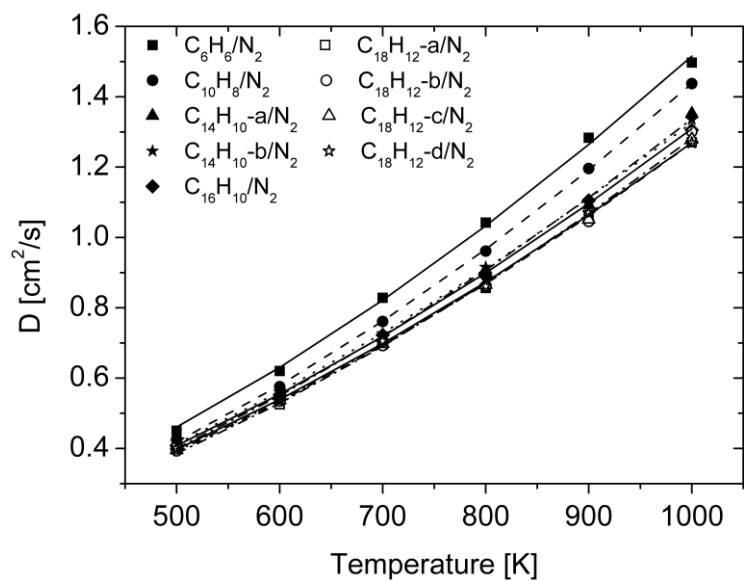


Figure 2.16 Mutual diffusion coefficients of aromatic molecules in nitrogen as a function of temperature, at 1 atm. The curves correspond to the least mean square curve fittings of MD results.



(a)

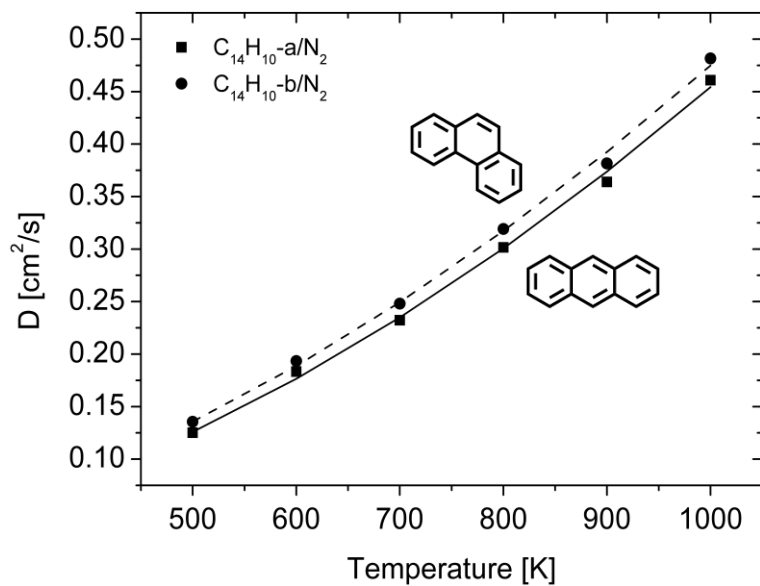


(b)

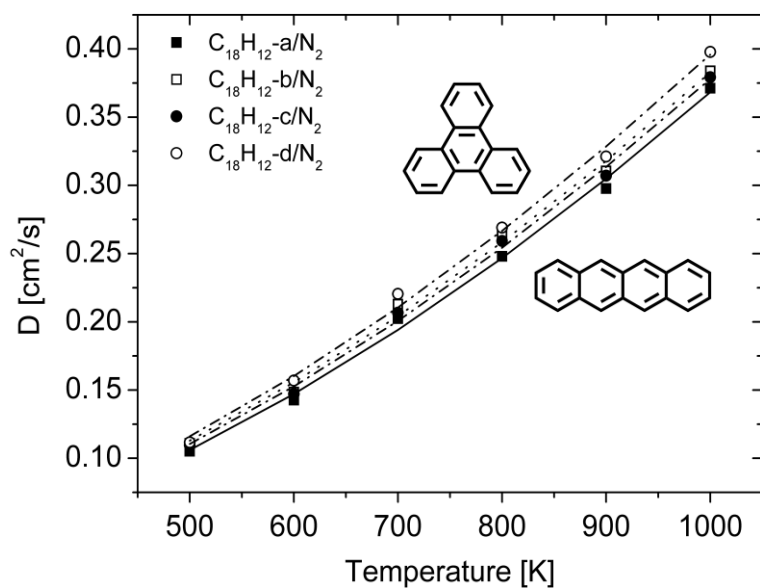
Figure 2.17 Self diffusion coefficients of (a) aromatic molecules and (b) nitrogen in the mixtures, at 1 atm. The curves correspond to the least mean square curve fittings of MD results.

In order to differentiate between the effect of molecular configurations and mass, we analyzed the mutual diffusion coefficients of two groups of isomers (see Figure 2.18). Between three ring species,  $C_{14}H_{10}$ -a mixture has lower diffusion coefficients than  $C_{14}H_{10}$ -b mixture over the entire temperature range considered with a difference around 5%.

Four ring aromatic molecules also show a very similar trend. Diffusion coefficients decrease as aromatic rings are configured linearly.  $C_{18}H_{12}$ -a mixture has the smallest diffusion coefficients due to this configuration. Around 8% difference in diffusion values was observed between  $C_{18}H_{12}$ -a/ $N_2$  and  $C_{18}H_{12}$ -d/ $N_2$ . Although  $C_{18}H_{12}$ -b and  $C_{18}H_{12}$ -c mixtures show around 1% difference in their diffusion values, this deviation is too small to confirm the effect of molecular configuration when we consider the error range of our calculations. However, these two molecules produced larger diffusion coefficients than that of  $C_{18}H_{12}$ -a and smaller values than that of  $C_{18}H_{12}$ -d.



(a)



(b)

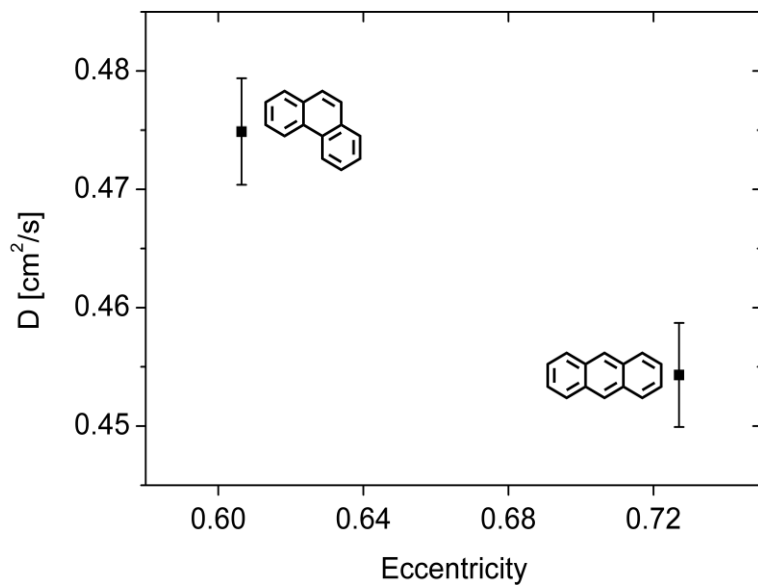
Figure 2.18 Mutual diffusion coefficients of isomers of aromatic hydrocarbons in nitrogen, at 1 atm (a) two ring aromatic molecules (b) four ring aromatic molecules.



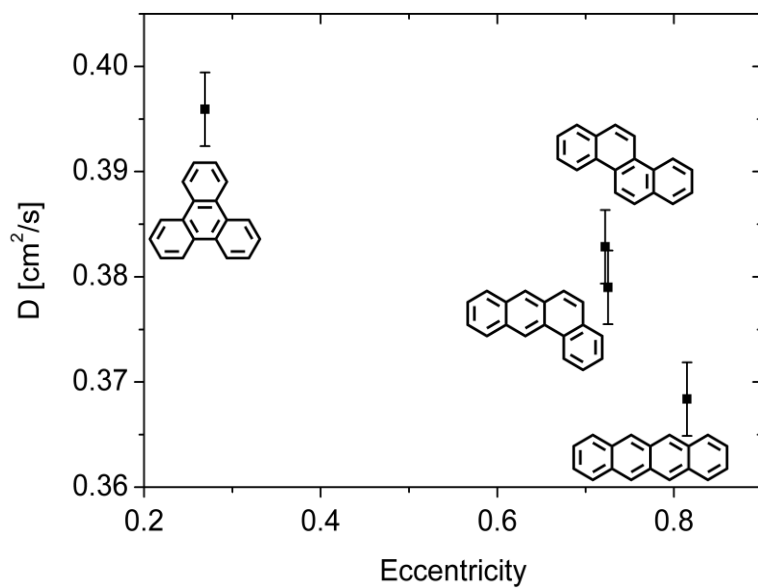
The diffusion coefficients of the above aromatic isomers can be characterized by employing eccentricity ( $e$ ) of molecules.<sup>[86]</sup> Eccentricity measures non-sphericity of a molecule and zero value represents a perfect sphere. The values increase as non-sphericity of molecules increase. In this study, we computed the eccentricity of molecules from the moment of inertia tensor:

$$e = 1 - \frac{I_{\min}}{I_{\text{avg}}} = 1 - \frac{I_{\min}}{(I_{xx} + I_{yy} + I_{zz})/3} \quad (2.20)$$

where  $I_{xx}$ ,  $I_{yy}$ , and  $I_{zz}$  denote the moment of inertia of principal axes and  $I_{\min}$  represents the minimum moment of inertia among the three main axes. Since aromatic molecules have planar structures, eccentricity can express their molecular configurations more effectively than radius of gyration used for heptane isomers.



(a)



(b)

Figure 2.19 Mutual diffusion coefficients of aromatic isomers in nitrogen at 1000K, 1 atm versus their eccentricity of (a) two ring aromatics and (b) four ring aromatics.

Figure 2.19 illustrates that the eccentricity of molecules can explain the trends of diffusion coefficients of aromatic isomers. As the eccentricity increases, the diffusion coefficients decrease. Moreover, from Figure 2.19 (b) we can confirm why  $C_{18}H_{12}$ -b and  $C_{18}H_{12}$ -c have very similar diffusion coefficients. This result shows that the assumption of spherical structures of gas kinetic theory is not appropriate especially for molecules that have planar structures. Aromatic rings have the almost same surface area irrespective of their arrangement and the deformations of their configurations during the interactions with other species are very small when compared with linear alkane molecules. Therefore, the isomers have very similar collision diameters and consequently, employing spherical representation for these molecules cannot express these structural characteristics effectively. Our results show that molecules that have configurations closer to spheres produce higher diffusion coefficients even though the collision diameters are very similar each other.

## 2.6 Comparison with gas kinetic theory

The Chapman-Enskog equation (equation 2.1) is advantageous in computing mutual diffusion coefficients due to its simplicity. However, the lack of potential parameters (collision diameter,  $\sigma$ , and energy well depth,  $\epsilon$ ) for molecules significantly limits its application. These potential parameters, especially for polyatomic molecules, are rarely available. Therefore, in this study, we employed correlations of corresponding state theory to obtain potential parameters, which were introduced in previous sections. Equations 2.2 through 2.4 were used for these calculations, with thermodynamic parameters obtained from the NIST chemistry

web data base. We compared results from MD simulations with those from C-E equation to show the effect of molecular configurations on diffusion coefficients. This comparison will show the deviation in diffusion values originated from the utilization of monatomic spherical potentials.

### **2.6.1 Thermodynamic properties and potential parameters**

Unfortunately, not all thermodynamic data are available for the hydrocarbons, considered in this study. Therefore we only listed the available thermodynamic data and the computed potential parameters in Table A.7 through A.9 in the Appendix A.

### **2.6.2 Linear alkanes**

Based on the potential parameters in Tables A.7 to A.9, diffusion coefficients were computed with the C-E equation. Figure 2.20 and Table A.10 in the Appendix A report mutual diffusion coefficients of linear alkanes as a function of temperature.

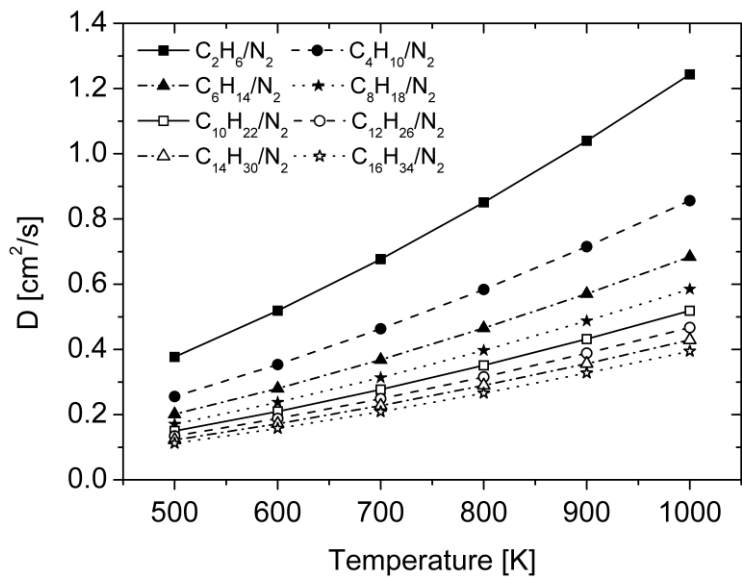


Figure 2.20 Mutual diffusion coefficients of linear alkanes in nitrogen as a function of temperature, at 1 atm obtained from the C-E equation.

As shown in Figure 2.20, the C-E equation produced very similar trends of diffusion coefficients compared with MD simulations (see Figure 2.10). For a more distinctive comparison, diffusion coefficients of four mixtures were plotted in Figure 2.21.

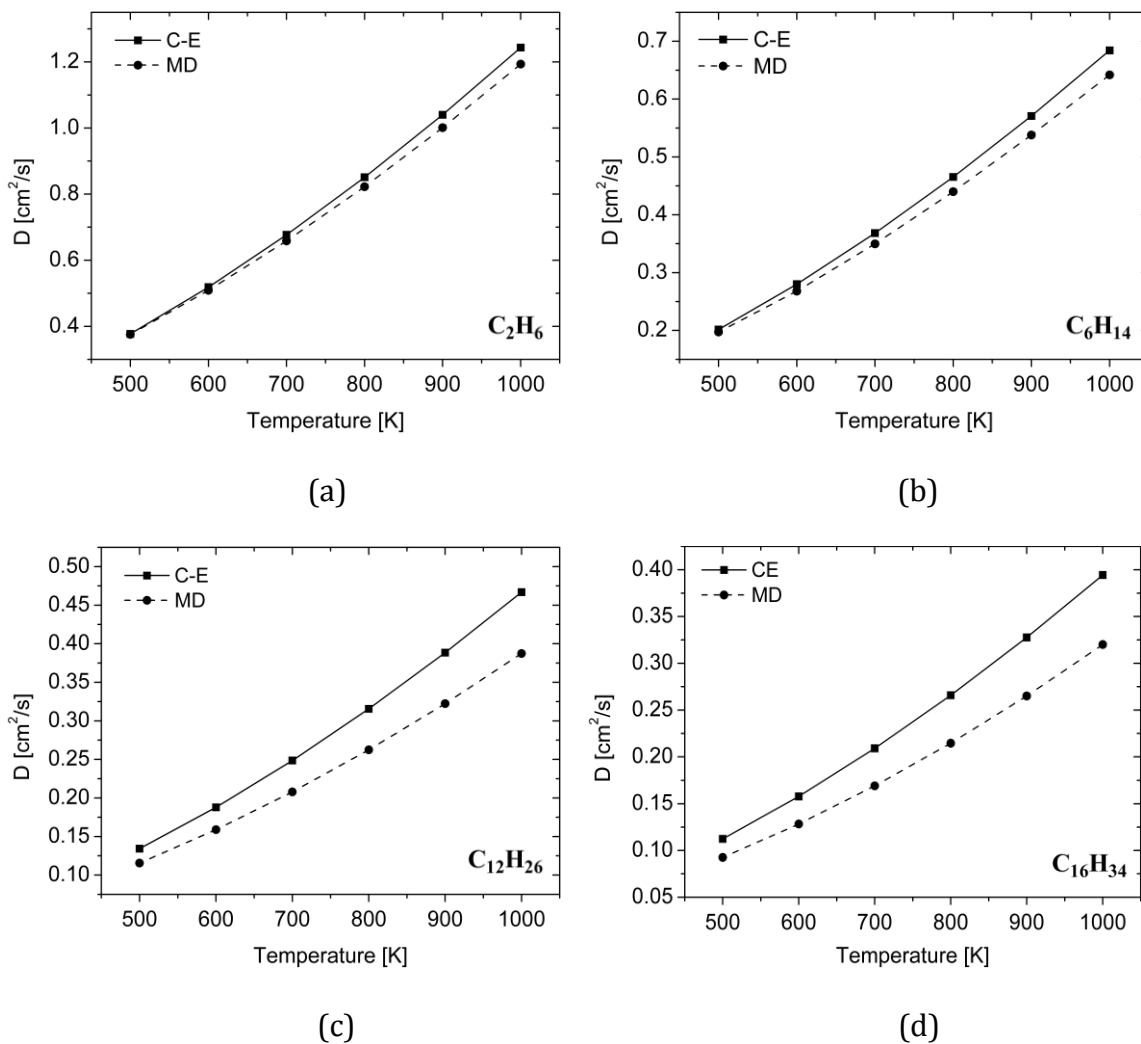


Figure 2.21 Comparison of mutual diffusion coefficients of (a)  $\text{C}_2\text{H}_6/\text{N}_2$ , (b)  $\text{C}_6\text{H}_{14}/\text{N}_2$ , (c)  $\text{C}_{12}\text{H}_{26}/\text{N}_2$ , and (d)  $\text{C}_{16}\text{H}_{34}/\text{N}_2$ , at 1 atm (MD: Molecular dynamics simulations, C-E: the Chapman-Enskog equation).

For the  $\text{C}_2\text{H}_6/\text{N}_2$  mixture, the results from MD simulations and those from C-E equation match well. Slight deviations can be found in high temperature region, but the overall values show a good agreement. However, the results of the  $\text{C}_{16}\text{H}_{34}/\text{N}_2$  mixture show totally different trends and exhibit large differences in diffusion values over the entire temperature region. The average deviation between the two

approaches is around 17% of diffusion values and MD simulations produced smaller diffusion coefficients than C-E equation. This result implies that the C-E equation can produce similar diffusion coefficients to those of MD simulations, when target molecules can be regarded as a sphere such as, CH<sub>4</sub> and C<sub>2</sub>H<sub>6</sub>. In other words, using single body interaction potentials is not appropriate for molecules that have non-spherical structures.

### 2.6.3 Cycloalkanes

The cycloalkane group considered in this study also shows similar trends of diffusion coefficients to those of alkane group. As the number of methyl groups increases, the diffusion coefficients decrease. Figure 2.22 and Table A.11 in the Appendix A show this trend clearly.

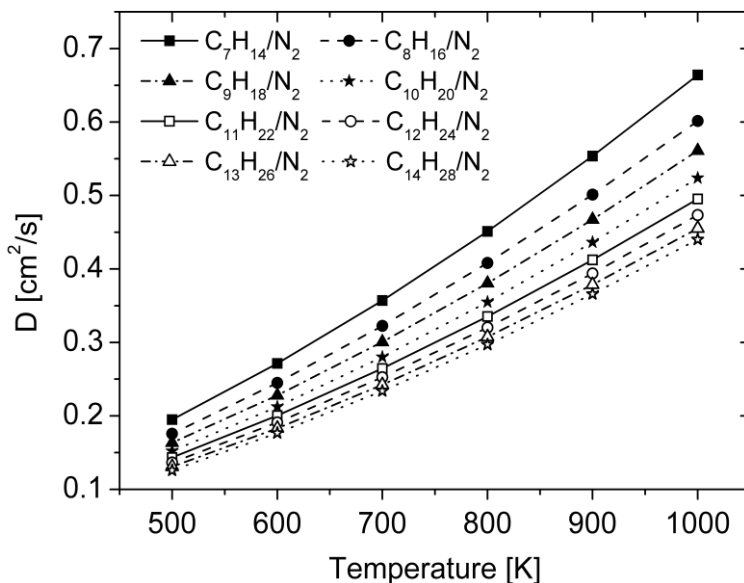


Figure 2.22 Mutual diffusion coefficients of cycloalkanes in nitrogen as a function of temperature, at 1 atm obtained from the C-E equation.

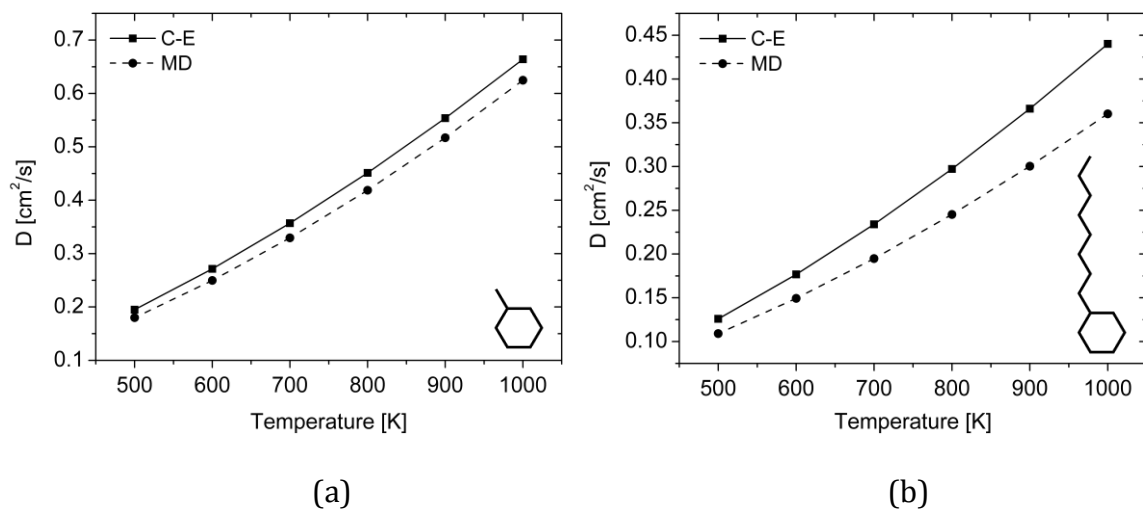


Figure 2.23 Comparison of mutual diffusion coefficients of (a)  $\text{C}_7\text{H}_{14}/\text{N}_2$  and (b)  $\text{C}_{14}\text{H}_{28}/\text{N}_2$ , at 1 atm (MD: Molecular dynamics simulations, C-E: Chapman-Enskog equation).

The  $\text{C}_7\text{H}_{14}/\text{N}_2$  mixture shows a 4% deviation between the two approaches and the  $\text{C}_{14}\text{H}_{28}/\text{N}_2$  mixture reveals a much larger deviation, around 16% (see Figure 2.23). As in linear alkanes, the C-E equation presented larger diffusion coefficients than MD simulations, likely due to the use of monatomic spherical potentials for cycloalkanes.

#### 2.6.4 Aromatic molecules

Figure 2.24 and Table A.12 in the Appendix A show mutual diffusion coefficients of aromatic molecules in nitrogen computed from C-E equation. The trends of diffusion coefficients are very similar to those of MD simulations.



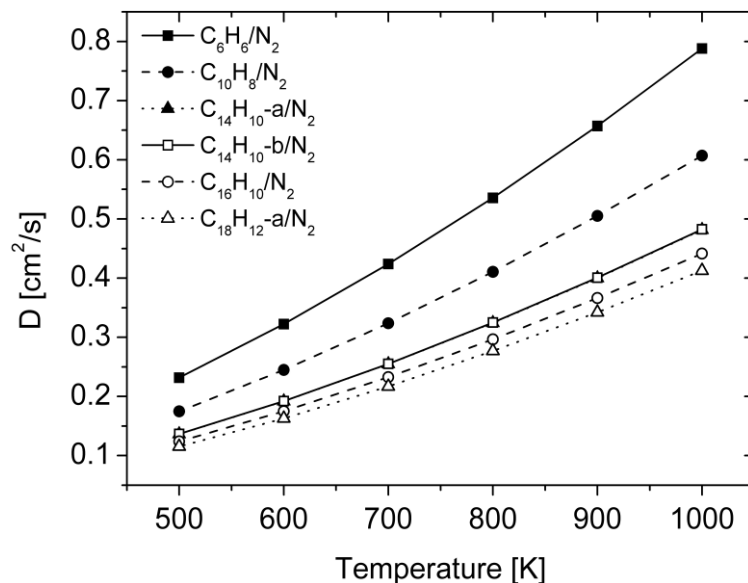


Figure 2.24 Mutual diffusion coefficients of aromatic molecules in nitrogen as a function of temperature at 1 atm obtained from the C-E equation.

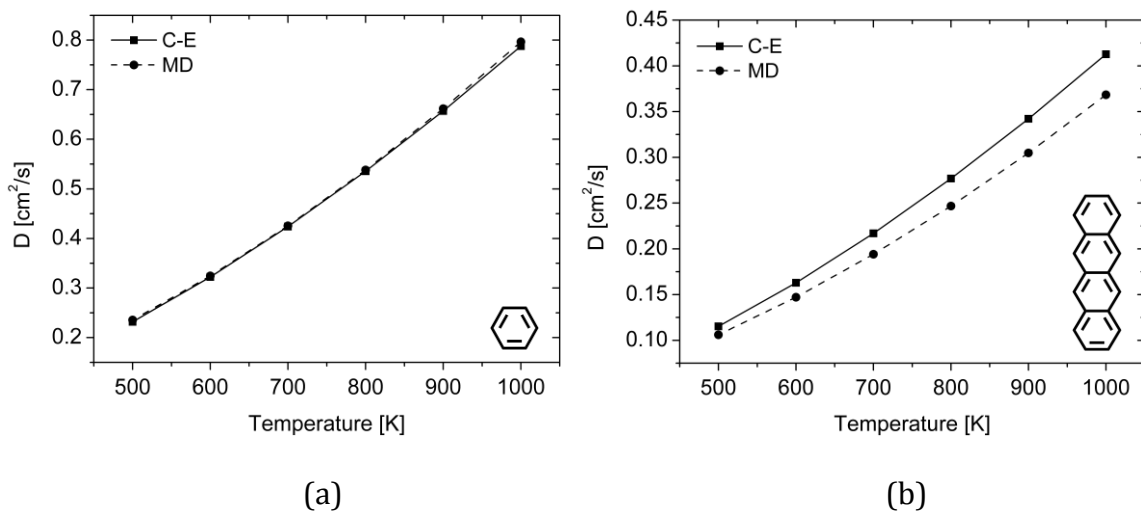


Figure 2.25 Comparison of mutual diffusion coefficients of (a) C<sub>6</sub>H<sub>6</sub>/N<sub>2</sub> and (b) C<sub>18</sub>H<sub>12</sub>-a/N<sub>2</sub> at 1 atm (MD: Molecular dynamics, C-E: Chapman-Enskog equation).

The comparison with MD simulations (Figure 2.25) shows that, in the  $C_6H_6/N_2$  mixture, MD and C-E results are perfectly matched. However, the  $C_{18}H_{12}a/N_2$  mixture exhibits approximately a 10% difference in diffusion coefficients. Even in this case, the C-E equation also produced higher diffusion coefficients than MD simulations over entire temperature ranges.

## 2.7 The effect of molecular configurations

The comparison between MD simulations and the C-E equation showed that single-body spherical potentials produced higher diffusion coefficients than all-atom potentials. Although, this analysis revealed the difference in diffusion values, the effect of molecular configuration on diffusion coefficients cannot be determined from those simple comparisons. We need to employ a geometric factor that can represent molecular structures at equilibrium state of MD simulations. Moreover, this factor has to be comparable to a collision diameter because the latter also is related to the molecular structure in gas kinetic theory. For this purpose, we computed radius of gyration (Rg) of each molecule with MD simulations. Since the computed Rg expresses equilibrium configurations obtained by averaging all possible conformations, it can represent the structural characteristics of all-atom description of MD simulations. The Rg can represent molecular configurations effectively because it reproduces the moment of inertia of the all atom molecules. As we confirmed in the result of heptane isomers (see Figure 2.8), Rg can be related to a collision diameter and be used as a geometric factor that explains the trends of diffusion values.

Before the use of  $R_g$  for the analysis, the temperature dependence of  $R_g$  should be noted. We computed  $R_g$  of the studied molecules in the temperature range of 500 – 1000K but the values did not vary significantly. Therefore, in the following, we are going to use the average value in the above temperature range, hence neglect the small temperature effect.

In gas kinetic theory, the changes of collision diameters ( $\sigma$ ) and energy well depths ( $\epsilon$ ) cause the variations in diffusion coefficients at fixed temperature and pressure condition. However, since the square inverse of  $\sigma$  is proportional to diffusion coefficients,  $\sigma$  has a dominant effect on determining diffusion values over energy well depths. As shown in Table 2.6, 10% perturbation of  $\sigma$  causes around 11.3% deviation from the original diffusion values. On the other hand, the same amount of perturbation of  $\epsilon$  produces only 1.5% deviation. As a result, in order to simplify the comparison we assumed that the contribution of energy well depths ( $\epsilon$ ) to diffusion values is negligible, and  $\sigma$  causes all the variations in diffusion values.

Table 2.6 The contributions of collision diameter and energy well depth to diffusion coefficients of  $n\text{-C}_7\text{H}_{16}/\text{N}_2$  mixture when 10% perturbation of  $\sigma$  and  $\epsilon$  are exerted.

Temperature [K]	$D_{12}$ [cm <sup>2</sup> /s]		
	No perturbation	perturbed $\sigma$	Perturbed $\epsilon$
500	0.185	0.164	0.182
1000	0.630	0.559	0.623
Deviation [%]	0	11.3	1.5

### 2.7.1 Linear alkanes

As shown in Figure 2.26, collision diameters of linear alkanes (Table A.7 in the Appendix A) used for the C-E equation were plotted with respect to their average radius of gyrations (Table A.13 in the Appendix A). If the collision diameters ( $\sigma_{C-E}$ ) are linearly related to the radius of gyrations (Rg), the assumption of spherical molecules in gas kinetic theory can represent polyatomic molecules successfully. However, Figure 2.26 illustrates that the second order fitting shows better matching with Rg. This second order fitting represents the deviation from sphericity of a molecule.

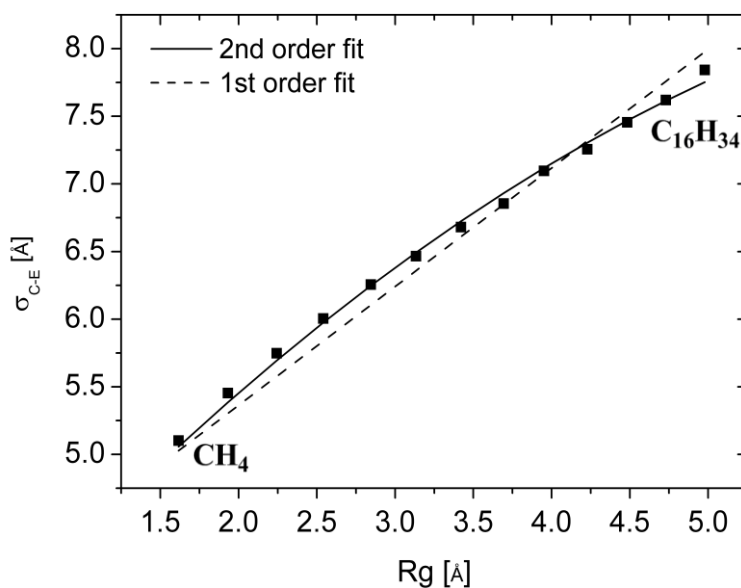


Figure 2.26 Collision diameters ( $\sigma_{C-E}$ ) of linear alkanes obtained from the C-E results and relations with average radius of gyrations (Rg).

To compare with the MD results, we obtained new collision diameters ( $\sigma_{\text{MD}}$ ) from the diffusion coefficients of MD simulations. Based on the discussion in the previous section, we obtained  $\sigma_{\text{MD}}$  by inserting the  $\varepsilon$  values of Table A.7 in the Appendix A into the C-E equation. These  $\sigma_{\text{MD}}$  represent new collision diameters that should be used to reproduce the diffusion coefficients of all-atom MD simulations with the same energy well depths employed for the C-E equation. In this way, we can address the effect of molecular configurations on diffusion coefficients by using single geometric parameters. The  $\sigma_{\text{MD}}$  of linear alkanes are listed in the Table A.14 in the Appendix A and Figure 2.27 represents the first and second order fitting results of  $\sigma_{\text{MD}}$  versus  $R_g$ . Although, we can still observe a little difference between the first and second order fitting, the deviation is much smaller when compared with the C-E results in Figure 2.26. This small discrepancy results from the temperature dependence of the radius of gyration and the effect of energy well depths that we neglected in our analysis. The smaller deviations in Figure 2.27 reveal that MD simulations can take into account molecular structures more effectively in diffusion calculations.

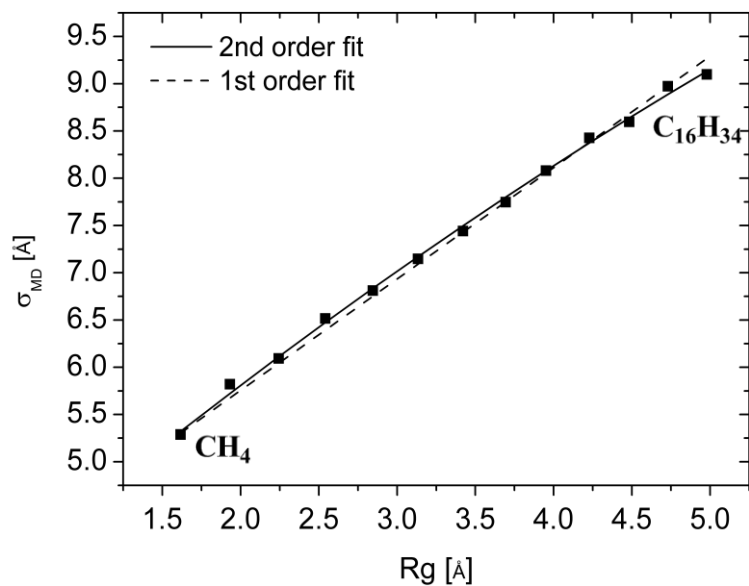


Figure 2.27 New collision diameters ( $\sigma_{MD}$ ) of linear alkanes obtained from MD results and relations with average radius of gyrations (Rg).

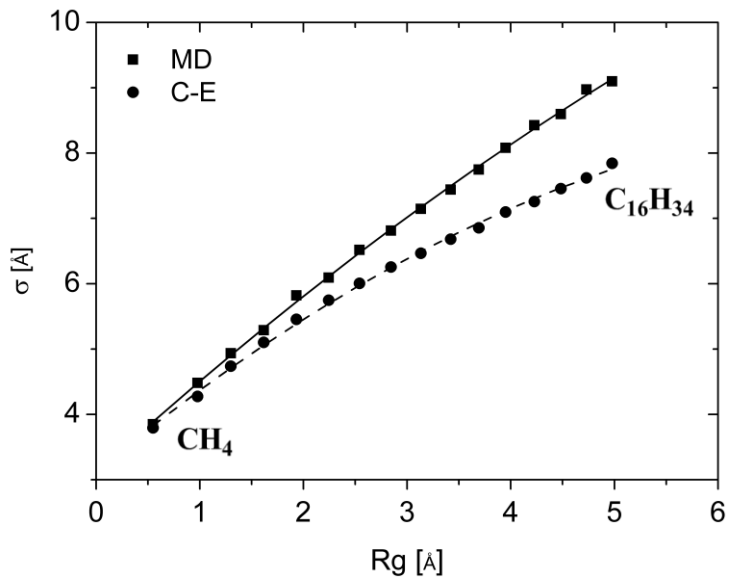


Figure 2.28 Comparison of collision diameters of linear alkanes obtained from MD and C-E results. Solid and dashed lines represent second-order fitting of  $\sigma_{MD}$  and  $\sigma_{C-E}$  respectively.

Figure 2.28 shows comparison between  $\sigma_{MD}$  and  $\sigma_{C-E}$ . The plot clearly demonstrates that the C-E equation presents larger deviation as the number of methyl groups increases. This trend implies that the C-E equation cannot produce reliable diffusion coefficients for polyatomic molecules.

The relation between  $\sigma_{MD}$  and  $\sigma_{C-E}$  of linear alkanes can be obtained by combining the two second order fitting expressions. In equation 2.21, the two collision diameters are related with only  $Rg$ . This relation suggests a simple way that can implement the effect of molecular configurations into the gas kinetic theory.

$$\sigma_{MD} = \frac{3.1115 + 1.4412Rg - 0.0465Rg^2}{3.1271 + 1.3203Rg - 0.0786Rg^2} \sigma_{C-E} \quad (2.21)$$

### 2.7.2 Cycloalkanes

The same comparison was conducted for cycloalkane group and the results were plotted in Figure 2.29. The  $\sigma_{MD}$  of cycloalkanes are listed in Table A.15 in the Appendix A. As in the results of linear alkanes, the C-E equation shows larger deviation as the number of methyl groups increases. The fitting results show that MD simulations can take into account the effect of molecular configurations successfully when compared with the C-E equation.

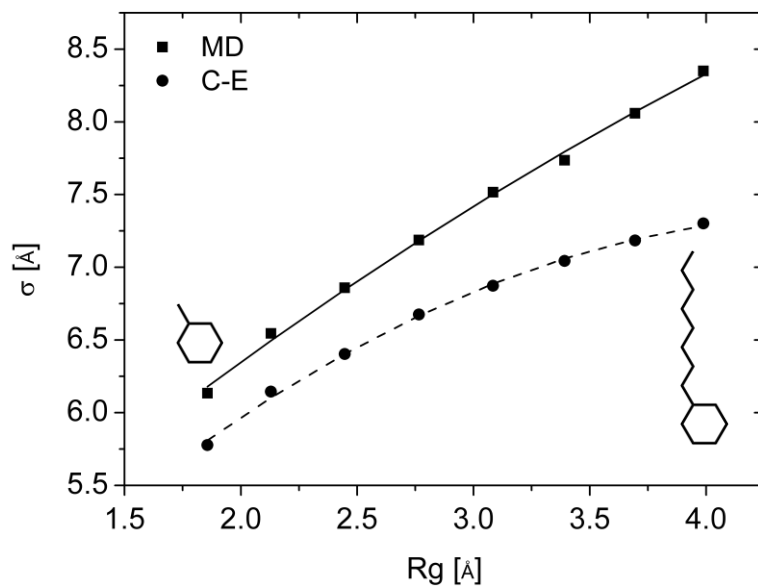


Figure 2.29 Comparison of collision diameters of cycloalkanes obtained from MD and C-E results. Solid and dashed lines represent second-order fitting of  $\sigma_{MD}$  and  $\sigma_{C-E}$  respectively.

The relation between  $\sigma_{MD}$  and  $\sigma_{C-E}$  of cycloalkanes is suggested in equation 2.22 and the  $Rg$  values are also listed in the Appendix A (Table A.16). New collision diameters that include the effect of molecular structures can be obtained the following relation.

$$\sigma_{MD} = \frac{3.7153 + 1.4779Rg - 0.0811Rg^2}{3.0126 + 1.8859Rg - 0.2042Rg^2} \sigma_{C-E} \quad (2.22)$$



### 2.7.3 Aromatic molecules

We compared four mixtures ( $C_6H_6/N_2$ ,  $C_{10}H_8/N_2$ ,  $C_{14}H_{10-a}/N_2$ , and  $C_{18}H_{12-a}$ ) to identify the effect of the number of rings in linearly configured aromatic molecules. Figure 2.30 shows that the deviations between the two approaches increase as the number of ring increases.

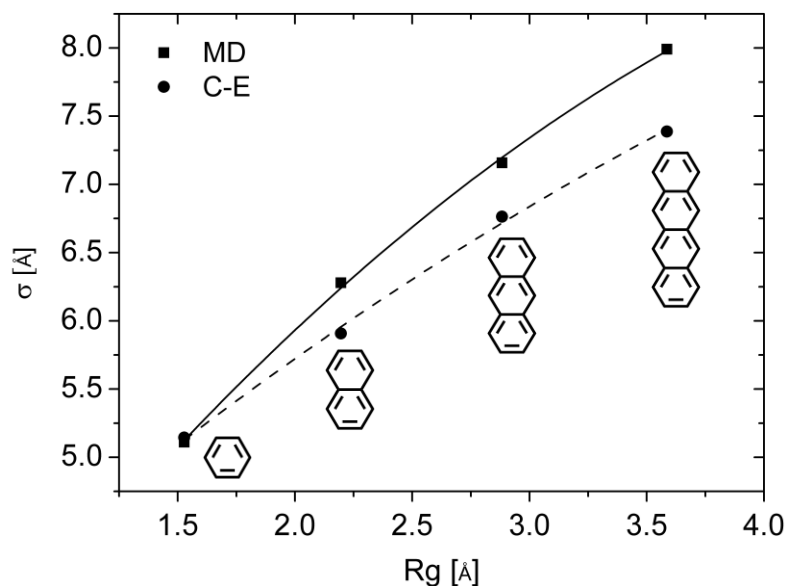


Figure 2.30 Comparison of collision diameters of linearly configured aromatic molecules obtained from MD and C-E results. Solid and dashed lines represent second-order fitting of  $\sigma_{MD}$  and  $\sigma_{C-E}$  respectively.

The relation between  $\sigma_{MD}$  and  $\sigma_{C-E}$  of linearly configured aromatic molecules is presented in equation 2.23. As in the other hydrocarbon groups, Rg expresses the

trends of collision diameters successfully. The  $\sigma_{MD}$  and Rg values of all aromatic molecules considered studied are listed in the Appendix A (Table A.17 and A.18).

$$\sigma_{MD} = \frac{1.8895 + 2.4283Rg - 0.2037Rg^2}{2.9125 + 1.5972Rg - 0.0963Rg^2} \sigma_{C-E} \quad (2.23)$$

Figure 2.31 illustrates the results of four ring aromatic isomers. In this group, we only plotted the  $\sigma_{MD}$  versus Rg. The results of the C-E equation are only available for C<sub>18</sub>H<sub>12</sub>-a due to the lack of experimental thermodynamic properties for other isomers.

As we mentioned in section 2.5, eccentricity (e) can explain the trends of diffusions among isomers more effectively than radius of gyrations (Rg) due to their planar structures. However, we used Rg for these isomers to assign a single geometric factor for all hydrocarbon groups considered in this study. Moreover, even though, C<sub>18</sub>H<sub>12</sub>-b and C<sub>18</sub>H<sub>12</sub>-c deviate from the fitting result, the difference in diffusion coefficients between the two species is very small (see Figure 2.19). Therefore, we concluded that the deviations of those two molecules exert very small effect on providing reasonable relations between Rg and  $\sigma_{MD}$ .

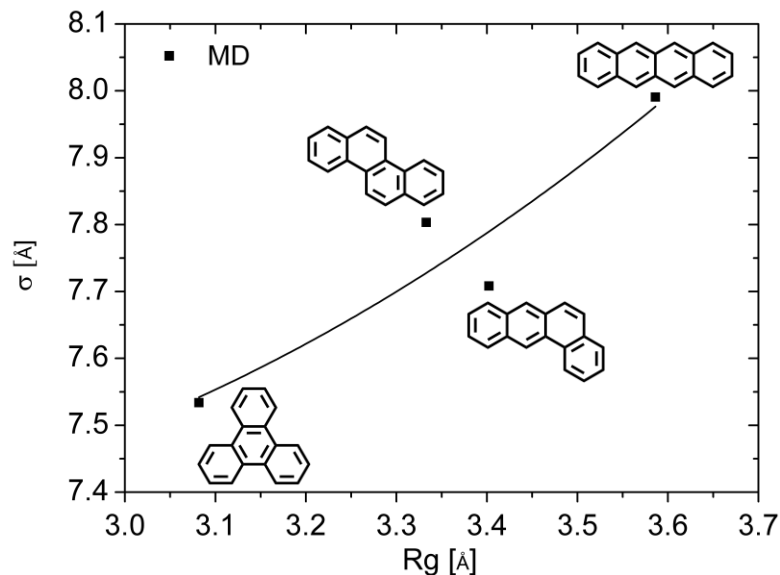


Figure 2.31 Comparison of collision diameters of four ring aromatic molecules obtained from MD results. Solid represent second-order fitting of  $\sigma_{MD}$ .

The relation between  $\sigma_{MD}$  and  $\sigma_{C-E}$  of four ring aromatic isomers is presented in equation 2.24. For this expression, we employed the value of  $C_{18}H_{12-a}$  as  $\sigma_{C-E}$  because it is the only available data for the C-E equation.

$$\sigma_{MD} = \frac{10.2023 - 2.3456Rg + 0.4810Rg^2}{7.3871} \sigma_{C-E} \quad (2.24)$$

## 2.8 Conclusions

In this chapter, we computed mutual diffusion coefficients of three hydrocarbon groups in nitrogen carrier gas by using both the Chapman-Enskog (C-E) equation and Molecular Dynamics (MD) simulations. After qualitative comparison

between the two approaches, we identified the effect of molecular configurations on diffusion coefficients by employing radius of gyration ( $R_g$ ). Our results showed that  $R_g$  could reproduce the trends of diffusion coefficients successfully and also could be used as a geometric factor that expresses molecular configurations effectively. We related  $R_g$  to the collision diameters obtained both from MD simulations ( $\sigma_{MD}$ ) and from the C-E equation ( $\sigma_{C-E}$ ). In this process, we observed that  $\sigma_{MD}$  produced much smaller deviations from the first order fitting with  $R_g$ . As a result, we concluded that MD simulations could take into account molecular configurations more effectively in diffusion calculations. The relations between  $\sigma_{MD}$  and  $\sigma_{C-E}$  are also presented for each hydrocarbon groups to implement the effect of molecular configuration into the C-E equation.

## Chapter 3

### The equivalent single body potentials of polyatomic molecules

#### 3.1 The effect of potentials on diffusion

In the previous chapter, we observed that molecular configurations exerted influence on the diffusion coefficients and all-atom MD simulations are more effective than gas kinetic theory in incorporating the effect of molecular structures into diffusion calculations. These results also showed that all-atom potentials produced smaller diffusion coefficients for all hydrocarbon classes compared with monatomic spherical potentials. This discrepancy between the two approaches was more distinctive for molecules that have higher mass and larger number of atoms. However these differences are the consequences of a more detailed description of molecular configurations and the employment of different potentials. In order to evaluate the relative importance of these two contributions, we removed the effect of the structures by reducing the all-atom multi body molecular potentials to equivalent single body potentials. For this purpose in this chapter, we computed

new Lennard-Jones (L-J) 12-6 potential parameters for the three hydrocarbon groups that we studied in chapter 2 by using MD simulations and OPLS AA force field. The new single body potential parameters were compared with the single body potential parameters (Tables A.7 to A.9 in the Appendix A) used for the C-E equation in the previous chapter.

### 3.2 Thermodynamic properties from MD simulations

Besides experimental measurements, the correlation of corresponding state is the most widely used to estimate L-J potential parameters ( $\sigma$  and  $\epsilon$ ) for gas kinetic theory.<sup>[48]</sup> Since this approach requires only critical temperature ( $T_c$ ) and pressure ( $P_c$ ), and normal boiling temperature ( $T_b$ ) of each species, the first step to obtain new potential parameters by using MD simulations should be the computation of the above thermodynamic properties.

To obtain the  $T_c$ ,  $P_c$ , and  $T_b$  from MD simulations, we computed the chemical potential at a given temperature and for different densities. This allowed us to compute liquid – vapor coexistence curves, the saturated pressures and liquid and vapor densities. From these liquid and vapor density values, we estimated the three thermodynamic properties ( $T_c$ ,  $P_c$ , and  $T_b$ ).<sup>[87, 88]</sup>

Several approaches have been developed for the calculations of coexistence curves such as the Gibbs Ensemble Monte Carlo (GEMC) technique<sup>[89]</sup>, NPT test particle method<sup>[90]</sup>, and NVT test particle method.<sup>[91]</sup> The GEMC technique has been widely used because the approach does not require many simulations for different system sizes nor free energy calculations.<sup>[92-94]</sup> However, volume fluctuations limit

stable simulations at high temperature region and the NPT test particle method also has the same problem.<sup>[95]</sup> On the other hand, volumes are fixed during simulations in the NVT test particle method so that this approach can perform stable simulations in the temperature region close to the critical point. Therefore, we used this method in this study.

In brief, we determined the coexistence curves and equilibrium vapor pressure by computing chemical potentials for liquid and vapor states separately at a constant temperature and volume condition. The pressure at the intersection of liquid and vapor curves in the pressure versus chemical potential plane is the equilibrium liquid – vapor pressure at a given temperature.<sup>[91]</sup> Pressures however, can be determined in a straightforward way from MD simulations. On the other hand, computing the chemical potentials requires a more complex approach.

### 3.2.1 Chemical potentials

The difficulty in computing chemical potential lies in measuring free energy. Chemical potential of a constant volume (V) and constant temperature (T) system is defined as:

$$\mu_i = \left. \frac{\partial A}{\partial N_i} \right|_{N,V,T} \quad (3.1)$$

where  $A$  denotes the Helmholtz free energy of the system and  $N$  is the number of molecules. Since the free energy is related to the canonical partition function itself

rather than being an ensemble average of the partition function,<sup>[74]</sup> different approaches are developed to circumvent this issue. A class of methods is based on the coupling parameter approach.<sup>[96]</sup> In these techniques, the coupling parameters are variables implemented into potentials to describe the continuous change of a system from the initial state to the final state.<sup>[96]</sup> In other words, the Hamiltonian of this transition can be written as:

$$H(\lambda) = \lambda H_1 + (1 - \lambda) H_0 \quad 0 \leq \lambda \leq 1 \quad (3.2)$$

where  $\lambda$  is the coupling parameter and  $H_1$  and  $H_0$  denote Hamiltonians at state  $\lambda=1$  and  $\lambda=0$  respectively.

Even though partition functions cannot be directly evaluated in a simulation, their derivatives with respect to coupling parameters can be evaluated as an ensemble average<sup>[74]</sup>:

$$\frac{dA}{d\lambda}_{N,V,T} = \frac{\int \frac{\partial U(\lambda)}{\partial \lambda} \exp[-\beta U(\lambda)] d\mathbf{r}^N}{\int \exp[-\beta U(\lambda)] d\mathbf{r}^N} = \left\langle \frac{\partial U(\lambda)}{\partial \lambda} \right\rangle_{\lambda} \quad (3.3)$$

where  $U$  is the potential energy of the system, expressed as a function of the coupling parameter. The kinetic energy of the system does not need to be considered because the kinetic energy is a quadratic function of momentum and its contribution to microcanonical partition function is analytical.<sup>[97]</sup> Hence, we can simply integrate out this term from the total partition function.



The difference in free energy between two states and resulting chemical potential are obtained by evaluating the following integrations (equations 3.4 and 3.5) with the slow growth method.<sup>[98]</sup>

$$A(\lambda=1) - A(\lambda=0) = \int_{\lambda=0}^{\lambda=1} \left\langle \frac{\partial U(\lambda)}{\partial \lambda} \right\rangle_{\lambda} d\lambda \quad (3.4)$$

$$\mu_i = \frac{\partial A}{\partial N_i} = \frac{1}{N_i} \int_{\lambda=0}^{\lambda=1} \left\langle \frac{\partial U(\lambda)}{\partial \lambda} \right\rangle_{\lambda} d\lambda \quad (3.5)$$

These integrations are related to a nonphysical path and the coupling parameters connecting the fully coupled ( $\lambda=0$ ) and fully uncoupled ( $\lambda=1$ ) states. The system has to change very slowly from fully coupled state to fully uncoupled state so that the system remains equilibrated during the process. In order to obtain this gradual change, discrete coupling parameters between 0 and 1 are chosen. The integration over these parameters leads to the change of free energy.<sup>[99, 100]</sup> The number and distribution of coupling values between 0 and 1 are related to the overlap of the probability distributions of potential energy between the reference state and the target state. Therefore, several intermediate states should be constructed so that the overlap of the probability distributions of two consecutive states becomes sufficient for direct evaluations.<sup>[97]</sup>

### 3.2.2 Simulation method

The change of chemical potential was calculated from the potential energy changes,  $\frac{\partial U(\lambda)}{\partial \lambda}$ , of a system through removal of a molecule at a random position of the system. For thermodynamic integration, we employed total eleven discrete coupling parameters ( $\lambda = 0.0, 0.1, \dots, 0.9, 1.0$ ). At  $\lambda=0$ , a molecule fully interacts with surrounding molecules and the molecule is fully uncoupled with a system at  $\lambda=1$ .

The potential energy interaction at each coupling value was computed with linear interpolation between state 0 and 1. However, this approach causes singularity problem when a molecule disappears ( $\lambda \rightarrow 1$ ) and in order to circumvent this issue, soft core potential was used.<sup>[101]</sup>

$$U_{sc}(r) = (1 - \lambda)U^{\lambda=0}(r_0) + \lambda U^{\lambda=1}(r_1) \quad (3.6)$$

$$r_0 = \left( \alpha \sigma_{\lambda=0}^6 \lambda^p + r^6 \right)^{\frac{1}{6}} \quad (3.7)$$

$$r_1 = \left( \alpha \sigma_{\lambda=1}^6 (1 - \lambda)^p + r^6 \right)^{\frac{1}{6}} \quad (3.8)$$

where  $U^{\lambda=0}$  and  $U^{\lambda=1}$  denote normal potentials at state  $\lambda=0$  and  $\lambda=1$  respectively,  $\alpha$  is the parameter for soft core scaling and  $p$  is the soft core power,  $\sigma$  is the radius of interactions and  $r$  is the distance between atoms.

In general, the value of  $\frac{\partial U(\lambda)}{\partial \lambda}$  has a weak dependency on the choice of the soft core scaling factor for  $\lambda \rightarrow 1$ . However, the deviation at that point contributes

only small portion to final result when the derivatives of potential energies are integrated over all  $\lambda$  values. Therefore, we can neglect the effect of the parameters.

To test the convergence of simulations, we compared the results obtained with simulations of different length for a box containing 300 octanes ( $n\text{-C}_8\text{H}_{18}$ ). The differences in free energy for 2, 3, and 4 ns runs were less than 2%. Therefore, we chose 2ns simulation time for our calculations. Moreover, every system was pre-equilibrated for 2ns before the actual simulations. All other conditions for simulations are the same as those for diffusion calculations.

Figure 3.1 shows an example of free energy calculation of an octane system at 540K and 42.7 kg/m<sup>3</sup> density. The integration of these discrete potential energies yields 1.756 KJ/mol for the free energy difference between the initial and the final states. Subsequently, this value becomes the difference of chemical potential at a given temperature and density.

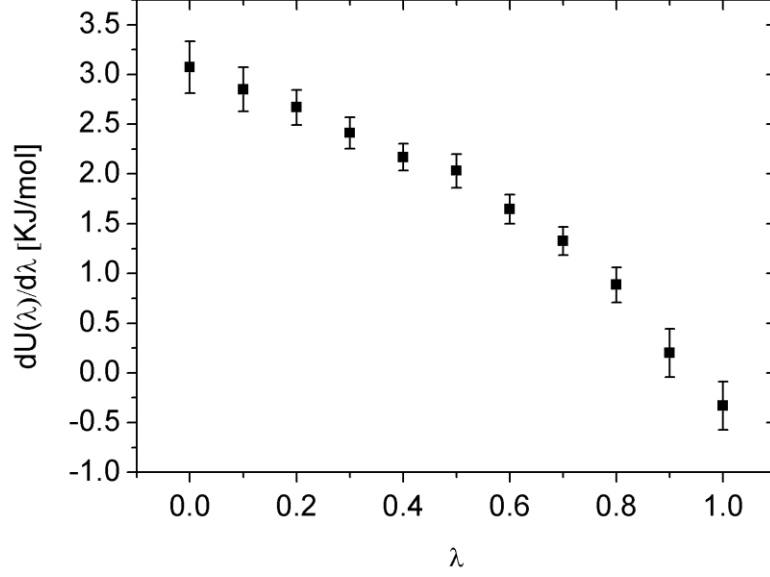


Figure 3.1 The change of potential energy of  $n\text{-C}_8\text{H}_{18}$  as a function of coupling parameters at 540K and 42.7 kg/m<sup>3</sup> density.

The errors on Figure 3.1 were estimated by using block averaging method<sup>[102]</sup> and an example of the error analysis for  $\lambda=0.5$  was plotted in Figure 3.2. The dashed line is the estimated error obtained by assuming all the blocks are independent. The solid line is the fitted results by using the following exponential function:<sup>[103]</sup>

$$\varepsilon^2(t) = \frac{2\sigma^2}{T} \left[ \alpha \tau_1 \left\{ 1 + \frac{\tau_1}{t} (e^{-t/\tau_1} - 1) \right\} + (1-\alpha) \tau_2 \left\{ 1 + \frac{\tau_2}{t} (e^{-t/\tau_2} - 1) \right\} \right] \quad (3.9)$$

where  $\sigma$ ,  $\alpha$ ,  $\tau_1$ , and  $\tau_2$  are fitting constants and T is total simulation time.

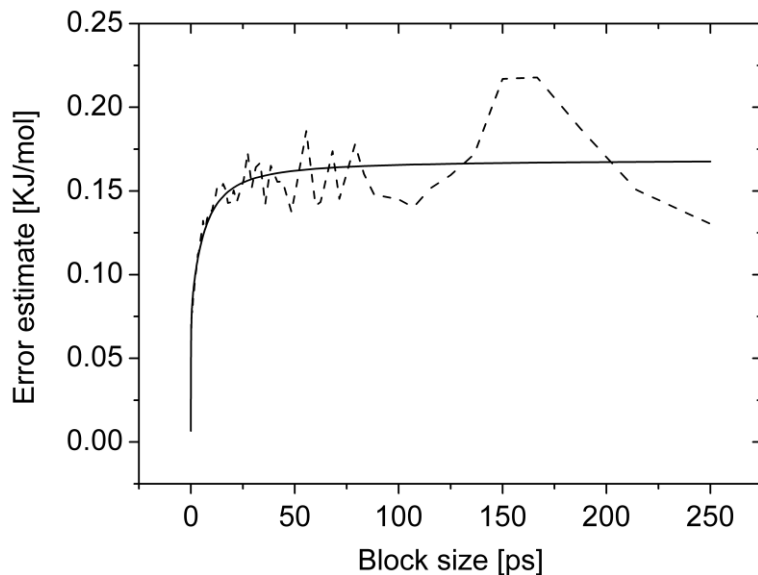


Figure 3.2 Estimated error by using block averaging analysis for  $\lambda=0.5$  of Figure 3.1.

The above graph demonstrates that the error value is well converged. The estimated errors for all  $\lambda$  values are listed in Table B.1 in the Appendix B.

### 3.2.3 Equilibrium vapor pressure and densities

Figure 3.3 illustrates the computed chemical potentials and pressures of liquid and vapor octane systems at 540K. Simulations were performed at several different volumes for both liquid and vapor branches to obtain relations between chemical potential and pressure at a fixed temperature. The solid squares denote liquid state and the hollowed circles represent vapor state. The intersection of the two lines provides equilibrium vapor pressure ( $P_{sat}$ ) at a given temperature. Once the  $P_{sat}$  is obtained, the liquid density ( $\rho_{liq}$ ) and vapor density ( $\rho_{vap}$ ) can be computed from liquid and vapor branches in Figure 3.3 respectively. However, the estimation

of critical properties and normal boiling temperature requires the  $\rho_{liq}$  and  $\rho_{vap}$  at  $P_{sat}$  obtained at two different temperatures. To reduce the statistical error, we repeated the same procedure for three different temperatures and we averaged the results obtained for all the pairwise combinations.

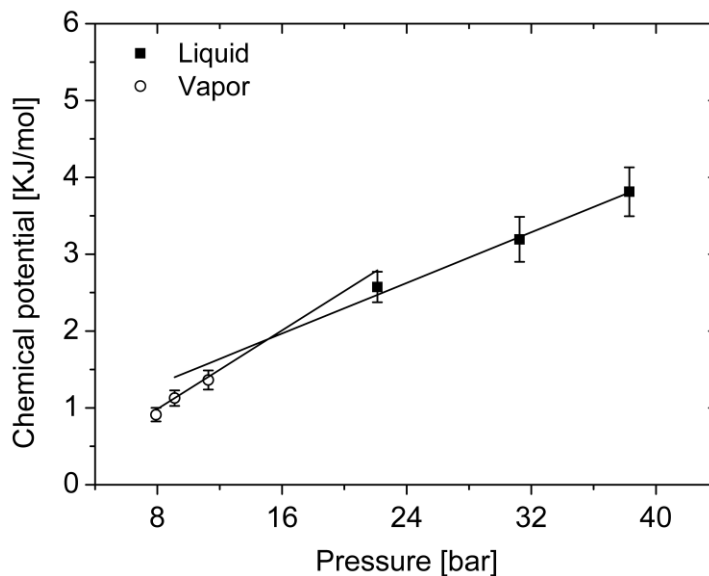


Figure 3.3 Chemical potential and pressure of octane ( $n\text{-C}_8\text{H}_{18}$ ) computed from MD simulations at 540K.

In Table 3.1, we list  $P_{sat}$ ,  $\rho_{liq}$ , and  $\rho_{vap}$  values both from MD simulations and from experimental measurement for comparison. Experimental data were obtained from NIST chemistry database.

Table 3.1 Comparison of equilibrium vapor pressures ( $P_{sat}$ ), liquid densities ( $\rho_{liq}$ ) and vapor densities ( $\rho_{vap}$ ) of linear alkanes at  $P_{sat}$  and different temperatures. Dv denotes the average percentile deviations from experimental values.

		MD			EXP		
	Temp [K]	$P_{sat}$ [bar]	$\rho_{liq}$ [kg/m <sup>3</sup> ]	$\rho_{vap}$ [kg/m <sup>3</sup> ]	$P_{sat}$ [bar]	$\rho_{liq}$ [kg/m <sup>3</sup> ]	$\rho_{vap}$ [kg/m <sup>3</sup> ]
C <sub>2</sub> H <sub>6</sub>	290	33.4	226.5	52.3	35.2	351.7	77.4
	280	27.1	237.2	42.2	28.1	383.2	56.6
	270	21.4	245.8	33.9	22.1	407.8	42.3
Dv [%]		<b>3.9</b>	<b>35.8</b>	<b>25.9</b>			
C <sub>4</sub> H <sub>10</sub>	400	22.4	263.1	45.9	24.9	408.5	73.1
	390	19.2	273.5	40.2	20.9	433.2	57.5
	380	15.9	281.5	34.1	17.4	454.2	45.8
Dv [%]		<b>8.9</b>	<b>36.8</b>	<b>30.9</b>			
C <sub>6</sub> H <sub>14</sub>	470	15.5	301.1	37.2	17.2	444.4	59.3
	460	13.1	311.6	32.4	14.6	463.8	48.2
	450	11.0	320.8	27.9	12.3	481.1	39.4
Dv [%]		<b>9.7</b>	<b>32.8</b>	<b>33.1</b>			
C <sub>8</sub> H <sub>18</sub>	550	17.6	286.8	55.6	19.1	389.7	92.2
	540	15.5	309.6	48.4	16.5	419.6	72.6
	530	13.0	327.5	42.1	14.3	443.2	58.7
Dv [%]		<b>8.5</b>	<b>26.4</b>	<b>32.8</b>			

The results show that OPLS AA parameters underestimate equilibrium pressures and densities. The average percentile deviation (Dv) of equilibrium

pressure from experimental results is 3.9% for ethane (C<sub>2</sub>H<sub>6</sub>) and around 9% for other normal alkanes, while MD simulations underestimate the densities around 30% of all species. These results demonstrate the characteristics of OPLS AA potentials at a temperature which differs substantially from the temperature used in the force field derivation. This force field was optimized at normal boiling temperature and liquid density was not tested at high temperature in their derivation process.<sup>[63]</sup> Based on the above results, we expect that all equilibrium pressures and densities obtained in this study are lower than measured values. We listed computed  $P_{sat}$ ,  $\rho_{liq}$ , and  $\rho_{vap}$  of all hydrocarbon groups considered in this study in the Appendix B (Tables B.2 to B.4)

### 3.2.4 Computed thermodynamic properties

With the computed  $\rho_{liq}$  and  $\rho_{vap}$  (Tables B.2 to B.4), critical temperature can be estimated by using the following scaling law:<sup>[104]</sup>

$$\frac{1}{2}(\rho_{liq} - \rho_{vap}) = A(T_c - T)^\beta \quad (3.10)$$

where  $\rho_{liq}$  and  $\rho_{vap}$  denote liquid and vapor densities at  $P_{sat}$  respectively,  $T$  is temperature where  $\rho_{liq}$  and  $\rho_{vap}$  are computed, and  $\beta$  is estimated as 0.325<sup>[105, 106]</sup>. Fitting parameter,  $A$ , and critical temperature,  $T_c$ , are obtained at the same time by inserting  $\rho_{liq}$  and  $\rho_{vap}$  of two different temperatures ( $T$ ) into equation 3.10.



Critical pressure,  $P_c$ , and normal boiling temperature,  $T_b$ , can be estimated by using the following Clausius-Clapeyron equation:

$$P = \exp\left(\frac{B}{T} + C\right) \quad (3.11)$$

where B and C are fitting parameters, which can be estimated by inserting the  $P_{sat}$  and its corresponding temperature ( $T$ ) into the equation 3.11. After these fitting parameters are determined, we can obtain the  $P_c$  by substituting  $T$  of the equation 3.11 with  $T_c$  and can also compute  $T_b$  by substituting  $P$  with 1 atm.

In Tables B.5 to B.7 in the Appendix B, we list both the computed critical properties and normal boiling temperatures and relevant experimental data for all the hydrocarbons. The comparison reveals that critical properties and boiling temperatures are in agreement with experimental data within a 7% deviation. These deviations are significantly small when compared with those of the densities. The reason for these results is that liquid-vapor coexistence curves are shifted toward lower density region without significant changes in shapes. As a result, critical properties and boiling temperatures have smaller deviation from experimental results even though the densities are less accurately reproduced.

### **3.3 Equivalent single body potentials of all atom potentials**

Once the thermodynamic properties ( $T_c$ ,  $P_c$ , and  $T_b$ ) were obtained, L-J 12-6 potential parameters can be computed by using the correlations of corresponding

state (equations 2.2 to 2.4). The computed parameters for all the hydrocarbons are listed in the Appendix B (Tables B.8 to Table 10).

### **3.4 Comparison with the C-E equation and MD simulations**

Based on the equivalent potentials obtained in the previous section, we computed diffusion coefficients of all the hydrocarbons by using the C-E equation. The computed diffusion values were compared with both those of MD simulations (Tables A.4 to A.6 in the Appendix A) and those of the C-E equation that used potential parameters obtained from experimental data (Tables A.10 to A.12 in the appendix) to show the difference in diffusion coefficients among those three approaches. As done in the previous chapter, we also related collision diameters ( $\sigma$ ) to radius of gyration ( $R_g$ ) and compared the results with those reported in the chapter 2. These comparisons will reveal the relative contributions of the molecular configuration and the employment of different potentials to diffusion coefficients.

#### **3.4.1 Linear alkanes**

Figure 3.4 illustrates the comparison of mutual diffusion coefficients of linear alkanes mixtures obtained with three different approaches: MD simulations (MD), the C-E equation with potential parameters obtained from experimental data (C-E<sub>EXP</sub>), and the C-E equation with equivalent single body potential parameters obtained from MD simulations in this chapter (C-E<sub>Equiv</sub>).

As shown in Figure 3.4, the  $C-E_{\text{Equiv}}$  produced very similar diffusion values to those of the  $C-E_{\text{EXP}}$  and has large deviation from MD results especially for long-chain linear alkanes. It follows that the single body equivalent potentials cannot take into account molecular configurations in diffusion calculations even though these potentials are derived by using an all-atom potential. Moreover, this similarity between  $C-E_{\text{EXP}}$  and  $C-E_{\text{Equiv}}$  proves that the deviations between MD simulations and the  $C-E_{\text{EXP}}$ , also analyzed in chapter 2, are caused by primarily the difference in molecular configurations rather than the employment of different potentials.

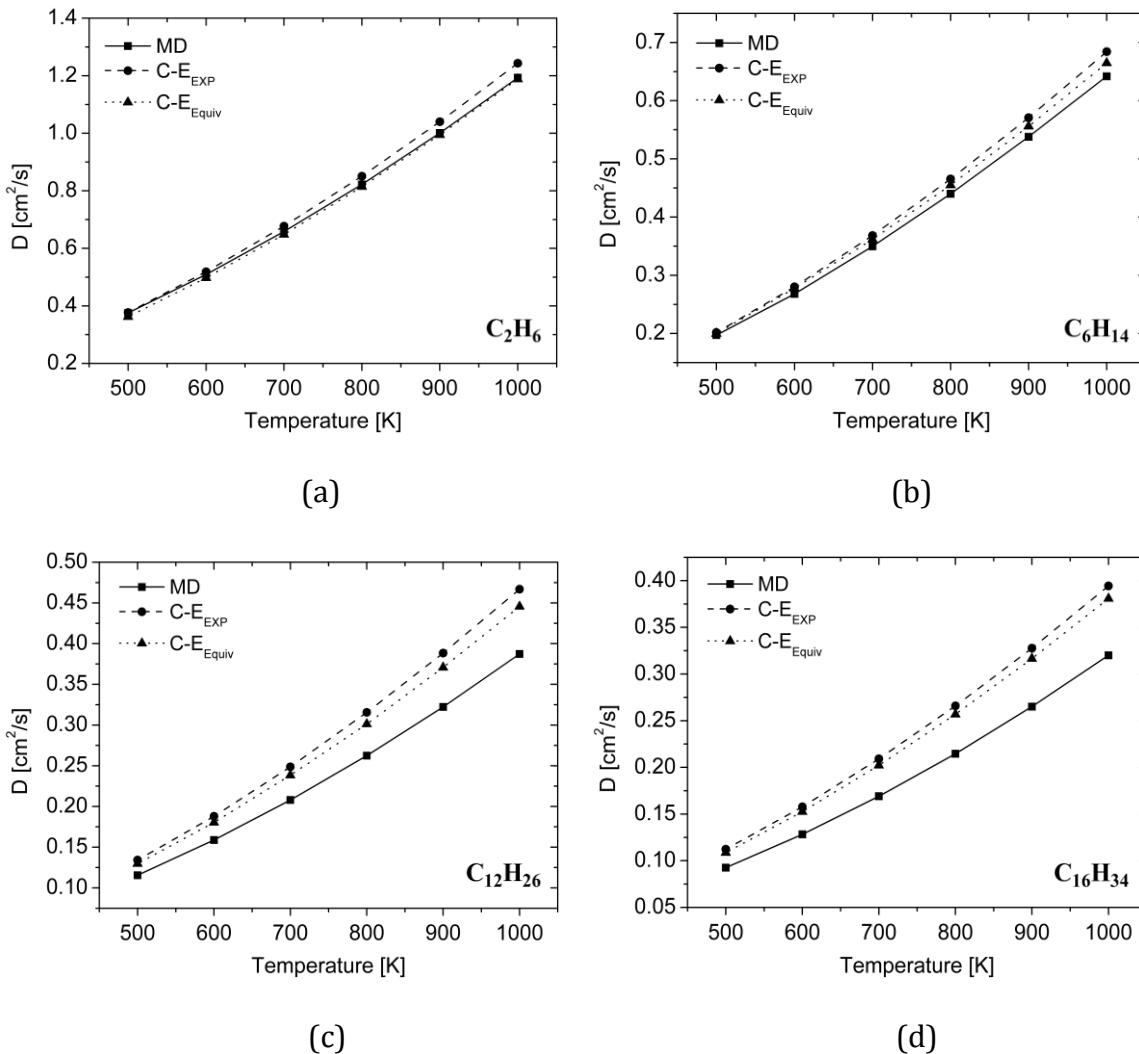


Figure 3.4 Comparison of mutual diffusion coefficients of (a) C<sub>2</sub>H<sub>6</sub>/N<sub>2</sub>, (b) C<sub>6</sub>H<sub>14</sub>/N<sub>2</sub>, (c) C<sub>12</sub>H<sub>26</sub>/N<sub>2</sub>, and (d) C<sub>16</sub>H<sub>34</sub>/N<sub>2</sub>, at 1 atm (MD: Molecular dynamics, C-E<sub>EXP</sub>: C-E equation with experiment data, and C-E<sub>Equiv</sub>: C-E equation with equivalent single body potentials).

To investigate how much information on molecular configurations was retained with this procedure, we computed collision diameters from the diffusion coefficients of C-E<sub>Equiv</sub> ( $\sigma_{\text{Equiv}}$ ) and compared with  $\sigma_{\text{C-E}}$  and  $\sigma_{\text{MD}}$ . As done in the

previous chapter,  $\sigma_{\text{Equiv}}$  were computed by inserting the energy well depths ( $\epsilon$ ) of Table A.7 in the Appendix A into the C-E equation (equation 2.1). Therefore,  $\sigma_{\text{Equiv}}$  represents collision diameters that should be used to reproduce the diffusion coefficients of the C-E<sub>Equiv</sub> with the same energy well depths employed for the C-E<sub>EXP</sub>.

Figure 3.5 illustrates that the  $\sigma_{\text{Equiv}}$  produces much larger deviation from the linear relation with  $R_g$  when compared with that of MD. Moreover, the trends of the  $\sigma_{\text{Equiv}}$  are very similar to those of  $\sigma_{\text{C-E}}$  and the deviations from  $\sigma_{\text{MD}}$  increase as the number of methyl groups increases. This result also confirms that the equivalent single body potentials and the correlations of corresponding state approaches cannot yield reliable diffusion coefficients for polyatomic molecules.

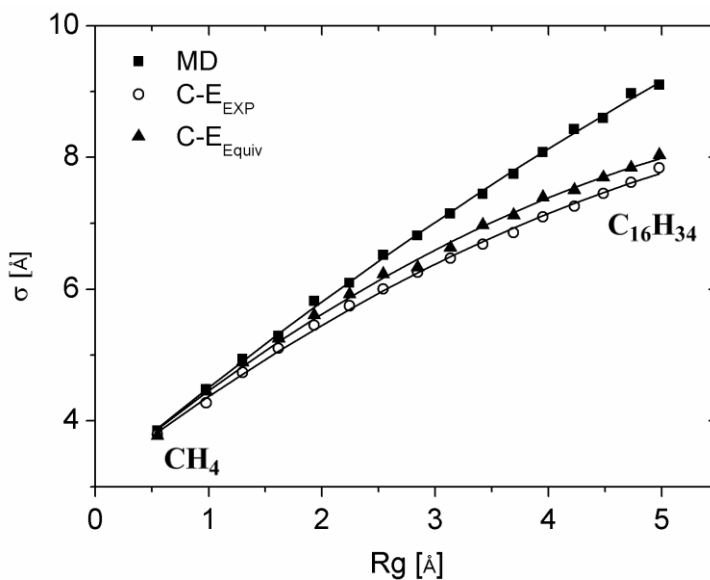


Figure 3.5 Comparison of collision diameters of linear alkanes obtained from MD, C-E<sub>EXP</sub>, and C-E<sub>Equiv</sub> results. Curves represent second-order fitting of  $\sigma_{\text{MD}}$ ,  $\sigma_{\text{C-E}}$ , and  $\sigma_{\text{Equiv}}$  respectively.

### 3.4.2 Cycloalkanes

As before, the trends of diffusion obtained from  $C-E_{\text{Equiv}}$  are very similar to those of the  $C-E_{\text{EXP}}$  and Figure 3.6 illustrates these results clearly. As the non-sphericity of molecules increases ( $C_{14}H_{28}$ ), the deviation between MD and  $C-E_{\text{Equiv}}$  increases. The similarity between  $C-E_{\text{EXP}}$  and  $C-E_{\text{Equiv}}$  is more evident as the shapes of molecules deviate from sphere structures. Again, these trends indicate the limitations of single body spherical potentials in computing diffusion coefficients of polyatomic molecules.

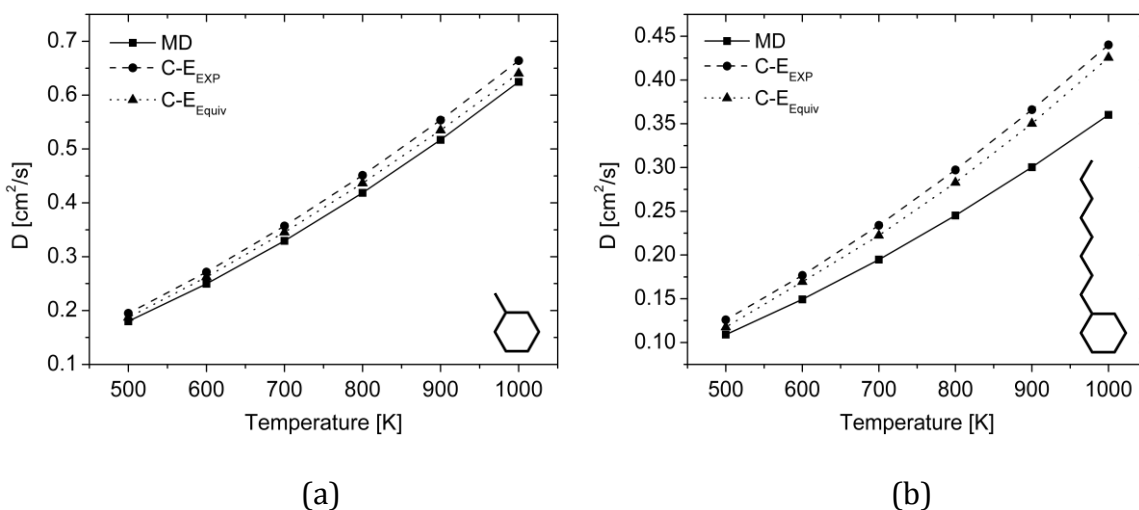


Figure 3.6 Comparison of mutual diffusion coefficients of (a)  $C_7H_{14}/N_2$  and (b)  $C_{14}H_{28}/N_2$ , at 1atm (MD: Molecular dynamics,  $C-E_{\text{EXP}}$ : C-E equation with experiment data, and  $C-E_{\text{Equiv}}$ : C-E equation with equivalent single body potentials).

As shown in Figure 3.7, the collision diameters of  $C-E_{\text{Equiv}}$  are also very similar to those of  $C-E_{\text{EXP}}$ . From the large deviation between MD and  $C-E_{\text{Equiv}}$ , we can

conclude that all-atom MD simulations are the most effective approach among those three methods to compute diffusion coefficients of polyatomic molecules.

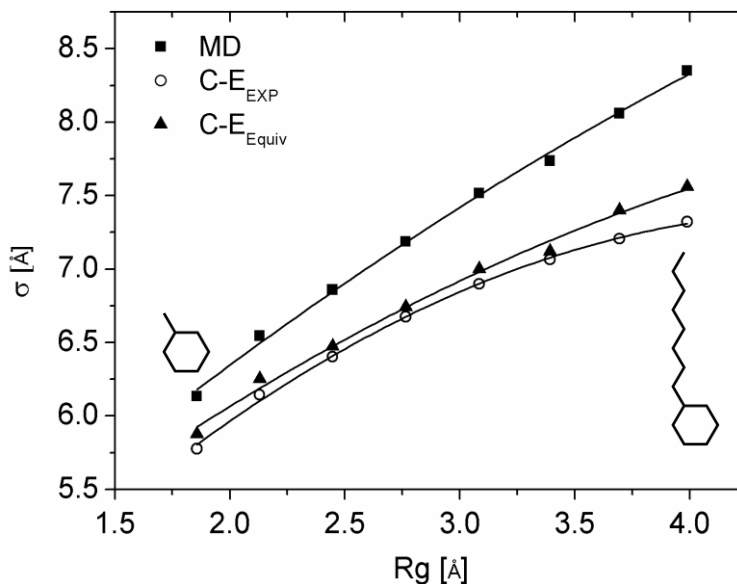


Figure 3.7 Comparison of collision diameters of cycloalkanes obtained from MD, C-E<sub>EXP</sub>, and C-E<sub>Equiv</sub> results. Curves represent second-order fitting of  $\sigma_{MD}$ ,  $\sigma_{C-E}$ , and  $\sigma_{Equiv}$  respectively.

### 3.4.3 Aromatic molecules

Aromatic molecules also show similar results to those of the other two hydrocarbon groups. Figure 3.8 illustrates mutual diffusion coefficients of four aromatic molecules that have linearly configured structures. For C<sub>6</sub>H<sub>6</sub>/N<sub>2</sub> mixture, all of the approaches produced very similar diffusion coefficients. However, for C<sub>18</sub>H<sub>12</sub>-a/N<sub>2</sub> mixture, C-E<sub>Equiv</sub> shows large deviation from MD. This result is evidence that single body spherical potentials are not appropriate in the diffusion calculations of linearly configured multi-ring aromatic molecules.

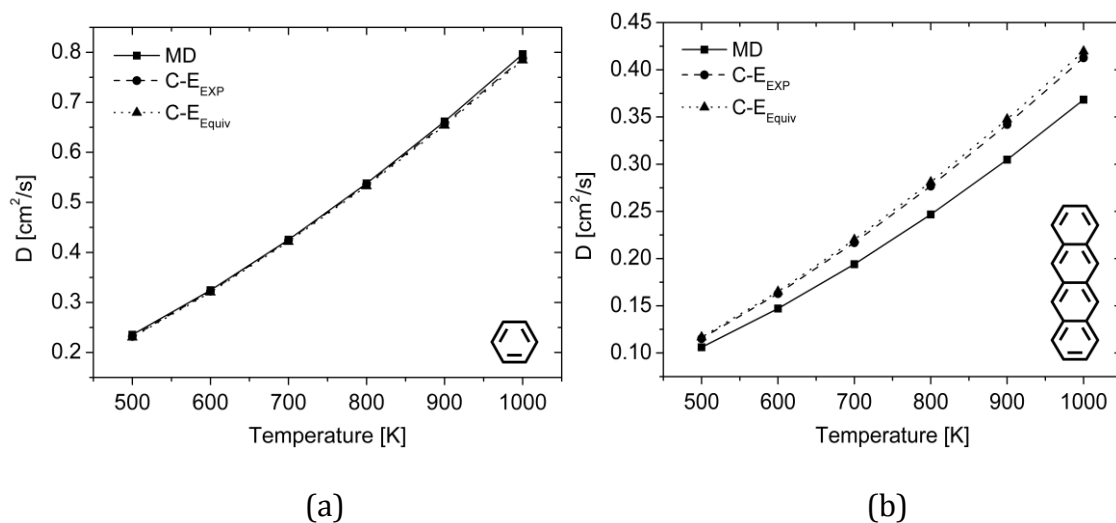


Figure 3.8 Comparison of mutual diffusion coefficients of (a)  $C_6H_6/N_2$  and (b)  $C_{18}H_{12-a}/N_2$ , at 1atm (MD: Molecular dynamics,  $C-E_{EXP}$ : C-E equation with experiment data, and  $C-E_{Equiv}$ : C-E equation with equivalent single body potentials).

We can observe the limitation of this approach more clearly from the relation between the radius of gyration and the collision diameters of  $C-E_{Equiv}$ . The deviations between MD and the both C-E results increase as the number of aromatic rings increase (Figure 3.9). This effect is likely the sum of both the single body approximation and the employment of the force field far from its intended temperature range.

For isomers, we did not find any noticeable difference in collision diameters because the thermodynamic properties are very similar. In our simulations, the simple change in the arrangement of aromatic rings does not affect the potentials obtained from the correlations of corresponding state, showing another important limitation of this approach.



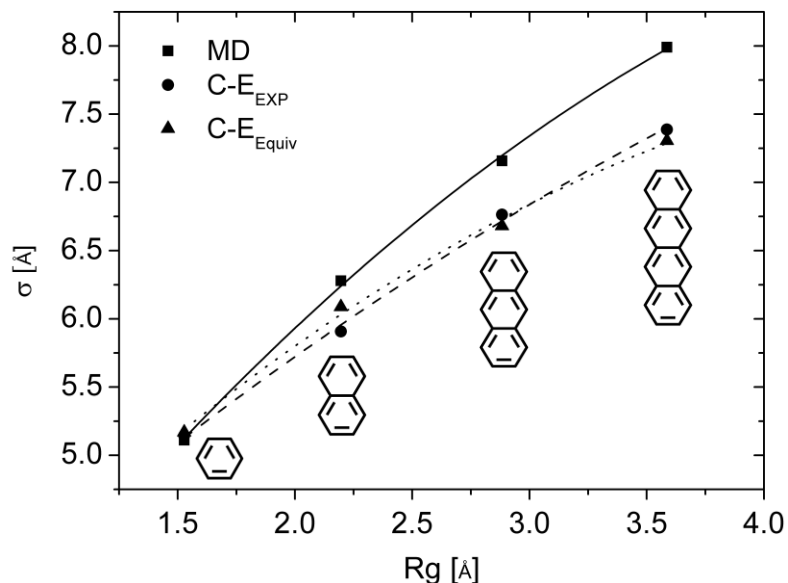


Figure 3.9 Comparison of collision diameters of aromatic molecules obtained from MD, C-E<sub>EXP</sub>, and C-E<sub>Equiv</sub> results. Curves represent second-order fitting of  $\sigma_{MD}$ ,  $\sigma_{C-E}$ , and  $\sigma_{Equiv}$  respectively.

### 3.5 Conclusions

In this chapter, we obtained equivalent single body potentials for all the studied hydrocarbons by reducing the multi body potentials. Free energy calculations were conducted to identify the coexistence curves and the correlations of corresponding state were used to obtain these equivalent L-J potential parameters.

Diffusion coefficients computed with these equivalent potentials were very similar to those from experimentally derived potentials and showed large deviations from MD results. Based on this result, we conclude that the molecular

configurations have a dominant effect on determining the deviations between MD simulations and the C-E equation. The comparison of collision diameters also revealed that single body spherical potentials cannot take into account molecular configurations in diffusion calculations and cannot distinguish between isomers.

Therefore, among the three approaches that we compared, molecular dynamics simulations with all-atom potentials provide the most effective way to compute diffusion of various hydrocarbons studied in this work and the correlations of corresponding state did not yield reliable diffusion coefficients for polyatomic molecules.

## Chapter 4

### Breakdown mechanisms of Decalin

#### 4.1 Decalin

Decahydronaphthalene, also known as decalin ( $C_{10}H_{18}$ ), is a bi-cyclic organic compound of the naphthalene class (Figure 4.1) and is the saturated analogue of naphthalene. Decalin can occur in *cis*- and *trans*- conformations and the latter is energetically more stable due to reduced steric interactions.<sup>[107, 108]</sup>

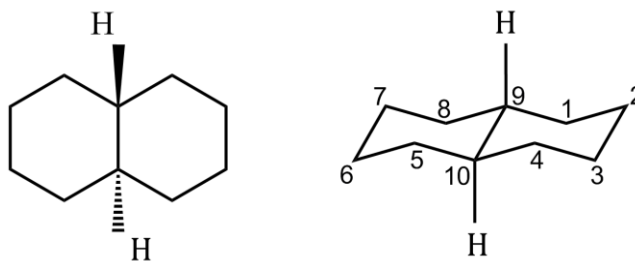


Figure 4.1 Trans-Decalin

Decalin has been shown to be one of the most thermally stable and endothermic fuel components of advanced jet fuels.<sup>[109, 110]</sup> In addition, it has shown favorable combustion characteristics in both gas turbines and diesel engines.<sup>[111, 112]</sup> Moreover, decalin can decompose without forming deposits so that it can be used at high temperatures.<sup>[113]</sup> This is one of the critical characteristics required for an advanced jet fuel.<sup>[114, 115]</sup> Decalin is also attractive as a potential hydrogen donor to suppress pyrolytic deposits.<sup>[116, 117]</sup> By donating hydrogen atoms to radicals, which are formed during the thermal decomposition process, decalin helps to prevent the formation of various thermal deposits.

For these reasons, decalin has been employed as a reference component of multi-ring naphthene classes for JP-8 surrogates.<sup>[5, 118, 119]</sup> Surrogates with 35 % by volume of decalin showed good agreement with experimental results on the sooting tendency of pool fire.<sup>[120]</sup> Agosta et. al. have included 6 % by volume of decalin in their surrogate to match the auto-ignition behavior of hydrocarbon fuels.<sup>[118]</sup>

Despite of the importance of decalin for combustion research, the fundamental reaction mechanisms of decalin have not been identified yet. Prompted by this need, the analysis of the breakdown mechanisms of decalin was performed by using Density Functional Theory (DFT) method. All transition states and intermediate states were identified, along with possible reaction pathways. Reaction rates were also computed for these reaction pathways. Finally, the identified pathways were implemented in a kinetic mechanism analysis code to simulate the pyrolysis environment.

## 4.2 Computational method

### 4.2.1 Electronic structure calculations

We explored potential energy surface of each reaction pathway by using a hybrid non local density functional theory (B3LYP), namely, Becke's three-parameter non local exchange<sup>[121, 122]</sup> with the non local correlation function of Lee, Yang and Parr.<sup>[123]</sup> This level of theory has been found to be sufficiently accurate for predicting the transition state properties for hydrogen abstraction reactions by radicals.<sup>[124, 125]</sup> Therefore, the theory has been widely used to study hydrogen abstraction reactions from hydrocarbons.<sup>[126-128]</sup> The geometry and frequency calculations for all of the species were carried out using the 6-31G(d,p) basis set. Transition States (TS) were identified by the existence of only a singular imaginary frequency. The frequency calculations also allowed the zero-point energy (ZPE) corrections to be obtained. Intrinsic Reaction Coordinate (IRC) calculations were carried out to verify that each transition state connected the corresponding reactants and products of a given reaction. All computations were carried out by using the GAUSSIAN 03 package.<sup>[129]</sup>

### 4.2.2 Reaction rates

The Rice-Ramsperger-Kassel-Marcus (RRKM) theory and the canonical Transition State Theory (TST) methods were used to derive high pressure limit rate constants for unimolecular and bimolecular reactions, respectively.<sup>[130-132]</sup> To

consider nonlinear Arrhenius effects, two parameter Arrhenius pre-exponential factors,  $A$  and  $n$ , were incorporated in the form of  $AT^n$ . Calculated rate constants for each reaction as a function of temperature were fitted into the modified Arrhenius form as:

$$k(T) = AT^n \exp(-E_a / RT) \quad (4.1)$$

Each rate constant was calculated by using the code TheRate (THEoretical RATES), from the web-based Computational Science and Engineering Online (CSE-Online) environment.<sup>[133]</sup> Transmission coefficients, which account for the quantum mechanical tunneling effect, were calculated by using the Eckart method.<sup>[134]</sup> The thermal rate coefficient is expressed as:

$$k(T) = \kappa(T) \sigma \frac{k_B T}{h} \frac{Q^\ddagger(T)}{\Phi^R(T)} e^{\frac{-\Delta V^\ddagger}{k_B T}} \quad (4.2)$$

where  $\kappa$  is the transmission coefficient,  $\sigma$  is the reaction symmetry number,  $Q^\ddagger(T)$  and  $\Phi^R(T)$  are the total partition functions per unit volume of the transition state and reactant, respectively,  $\Delta V^\ddagger$  is the classical barrier height,  $T$  is the temperature, and  $k_B$  and  $h$  are the Boltzmann and Planck constant, respectively.

### 4.3 Reaction pathways

Experimental results, previously reported for decalin pyrolysis at high temperatures, have shown that the most probable initiation reactions of thermal cracking are carbon-carbon (C<sub>9</sub> – C<sub>10</sub>) bond cleavage (Figure 4.2 (a)) reaction and hydrogen abstraction (from C<sub>1</sub>, C<sub>2</sub> and C<sub>9</sub>) reactions (Figure 4.2 (b)).<sup>[135-137]</sup> Billaud *et. al.* reported experimental results on the thermal cracking of decalin in a steam pyrolysis environment.<sup>[138]</sup> However, detailed reaction pathways and their reaction rate constants to build kinetic mechanisms are not yet available. Drawing on these experimental observations, in this study, a series of new breakdown reaction pathways of decalin were identified.

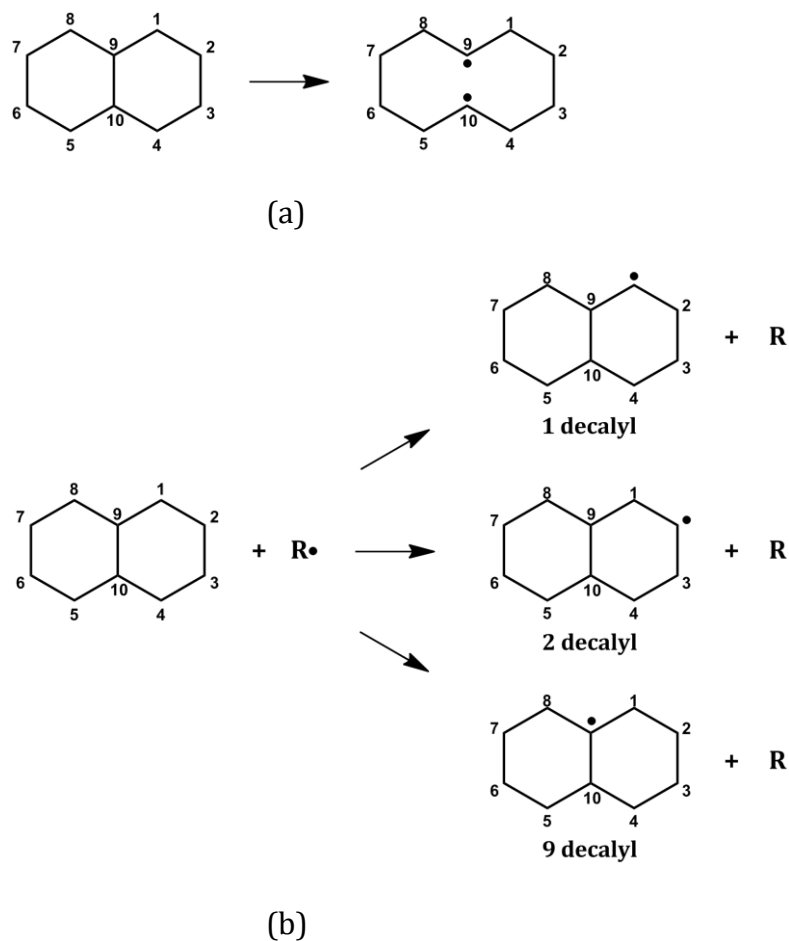


Figure 4.2 Initiation reactions of decalin breakdown mechanisms: (a) carbon - carbon bond cleavage, and (b) hydrogen abstractions.

### 4.3.1 Carbon - carbon bond cleavage reactions

Figure 4.3 shows the potential energy surface for the breakdown of decalin through C<sub>9</sub> - C<sub>10</sub> bond cleavage reactions. No transition state was identified to produce the intermediate 'b' (first order saddle point), and the reaction energy for 'a' → 'b' is 88.02 kcal/mol. Further Carbon - Carbon (C - C) bond cleavage leads to the formation of 'c' with an energy barrier of 38.11 kcal/mol.



The addition of hydrogen to the bi-radical 'c' produces the intermediate 'd' without any transition barrier. Radical 'd' undergoes C - C bond scission and produces C<sub>2</sub>H<sub>5</sub> and 'e'. The energy barrier for this step is 27.67 kcal/mol. Further C - C bond scission leads to the formation of the C<sub>5</sub>H<sub>9</sub> radical (f) and C<sub>3</sub>H<sub>5</sub>, followed by the formation of the allyl radical (g) and ethylene.

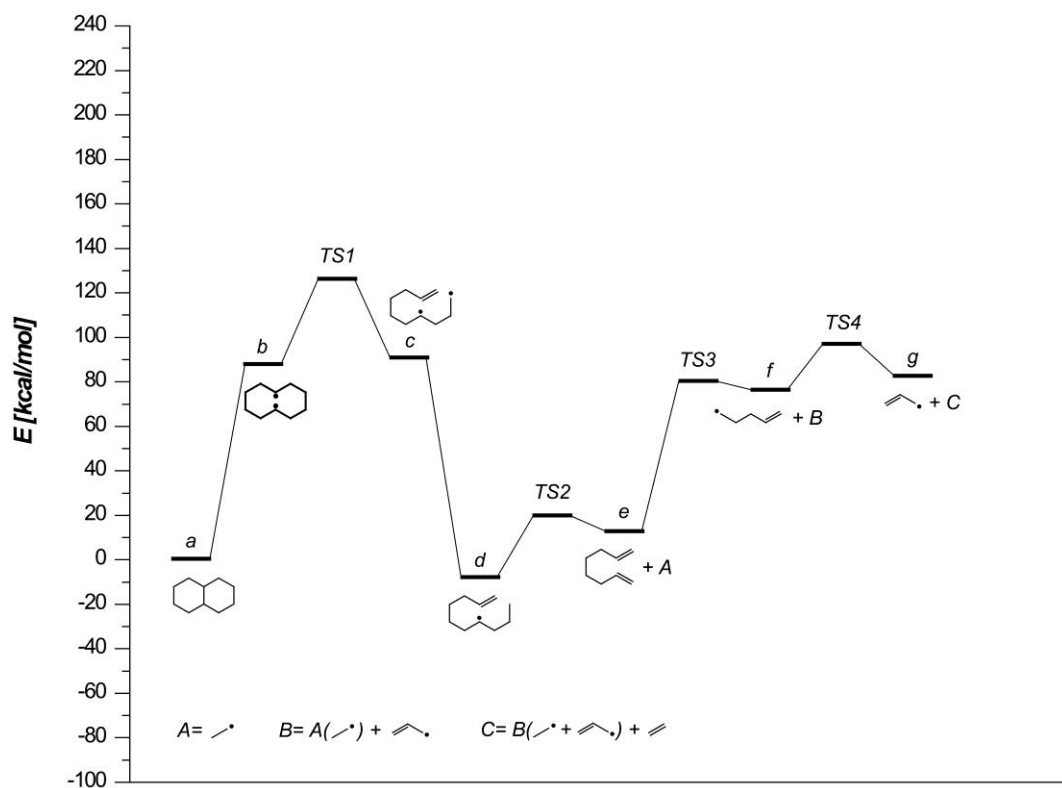


Figure 4.3 Potential energy diagram starting from C<sub>9</sub> - C<sub>10</sub> bond cleavage reaction.

### 4.3.2 Hydrogen abstraction reactions

Figure 4.4 reports the initiation steps for the formation of 1-, 2- and 9-decalyl radicals through hydrogen abstraction by CH<sub>3</sub> radical. The energy barrier to

produce 1-decalyl is 15.39 kcal/mol, higher than those of 2-decalyl and 9-decalyl, which are 14.81 and 13.52 kcal/mol, respectively.

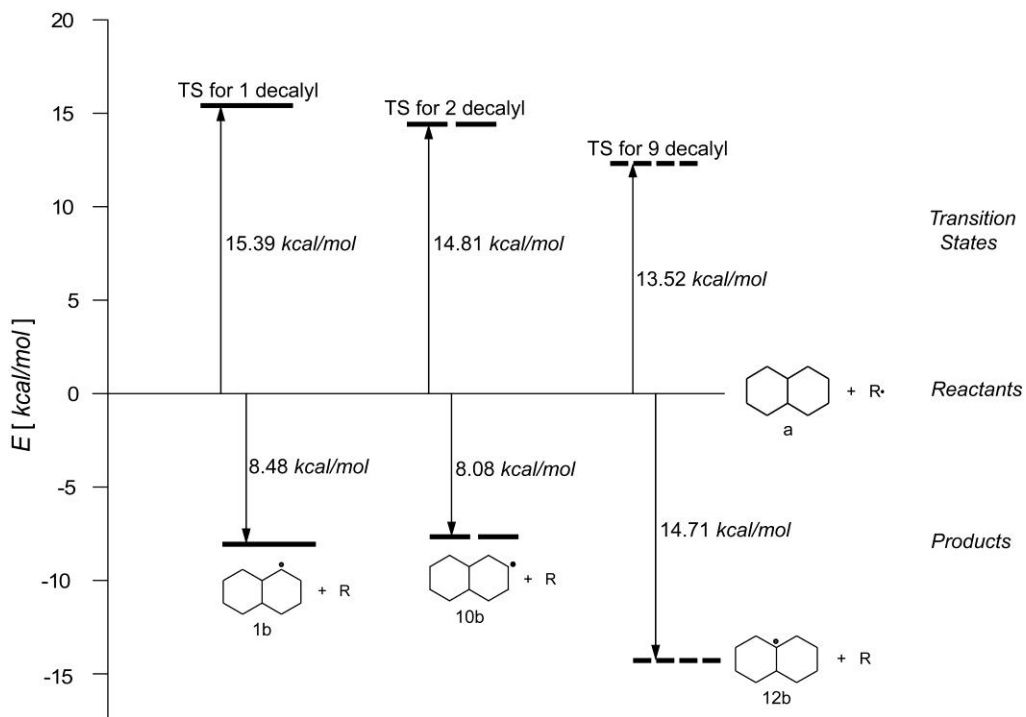


Figure 4.4 Energy barriers to produce 1-, 2-, and 9-decalyl radicals by hydrogen abstraction reaction.

### 4.3.3 Reaction pathways from 1-decalyl radical

Nine pathways were identified for the subsequent reactions of 1-decalyl radical (*1b*). Six of them (pathways 1 to 6) begin with the C<sub>8</sub> – C<sub>9</sub> bond scission and the others (pathways 7 to 9) start with the C<sub>2</sub> – C<sub>3</sub> bond scission.

Figure 4.5 reports pathways 1 and 2 that form toluene (C<sub>7</sub>H<sub>8</sub>). The energy barrier for the formation of radical '*1c*' is 34.62 kcal/mol and the following

hydrogen migration to produce '1d' has a transition energy of 11.32 kcal/mol. Subsequently, '1d' decomposes to form '1e' and the propyl (C<sub>3</sub>H<sub>7</sub>) radical. Hydrogen abstraction from the intermediate '1e' produces radical '1f' with a transition energy of 10.10 kcal/mol. From '1f' two different pathways were identified that lead to the formation of toluene. The '1f → 1g → 1h → toluene' route involves hydrogen addition, abstraction and further addition to produce toluene. From '1f', the most significant barrier is represented by '1f → 1g', which is 31.21 kcal/mol.

In pathway 2, '1f' undergoes two hydrogen abstraction reactions ('1f → 2g' and '2g → 2h') and hydrogen addition ('2h → toluene') to produce toluene. The energy barriers involved in this route are lower than the ones in pathway 1 and the intermediates are very stable.

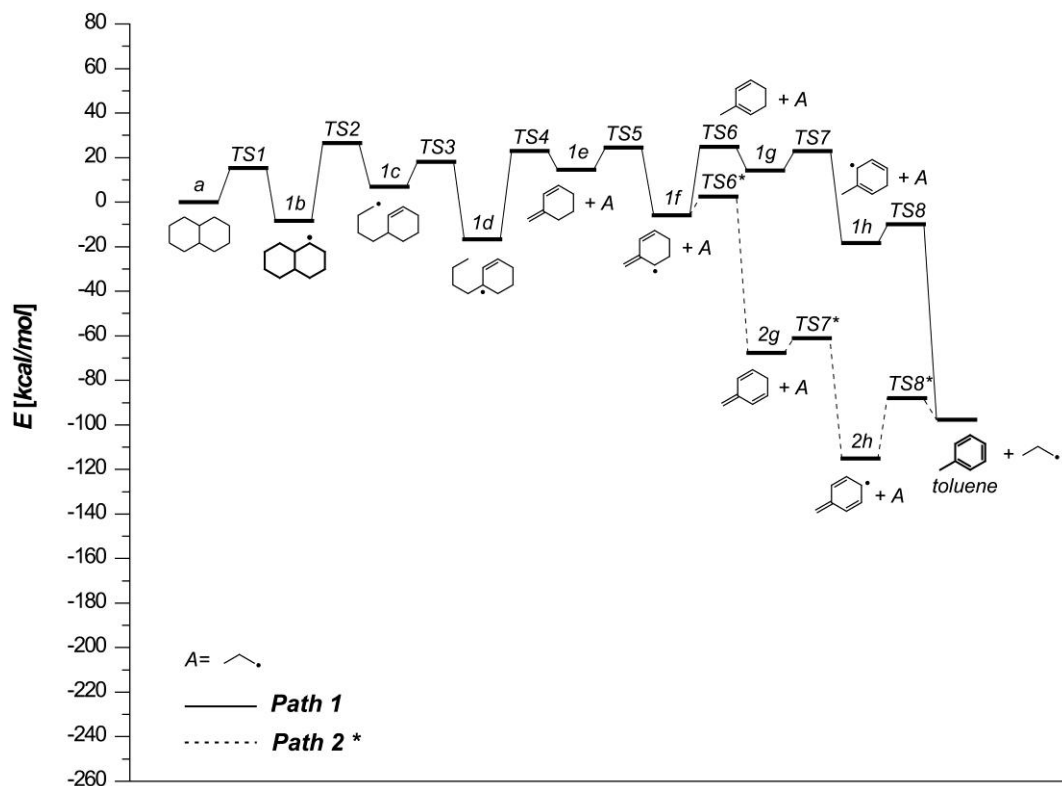


Figure 4.5 Potential energy diagrams for pathways 1 and 2.

As shown in Figure 4.6, three reaction pathways (pathways 3 to 5) start from the 1-decalyl radical (1b), which produce benzene and styrene. From the intermediate '1c', two subsequent  $\beta$ -scission reactions form '3d' and '3e'. The energy barriers of these reactions are 30.97 kcal/mol for '1c  $\rightarrow$  3d' and 22.48 kcal/mol for '3d  $\rightarrow$  3e'. Sequential hydrogen abstraction reactions, '3e  $\rightarrow$  3f  $\rightarrow$  3g  $\rightarrow$  benzene', lead to the formation of benzene.

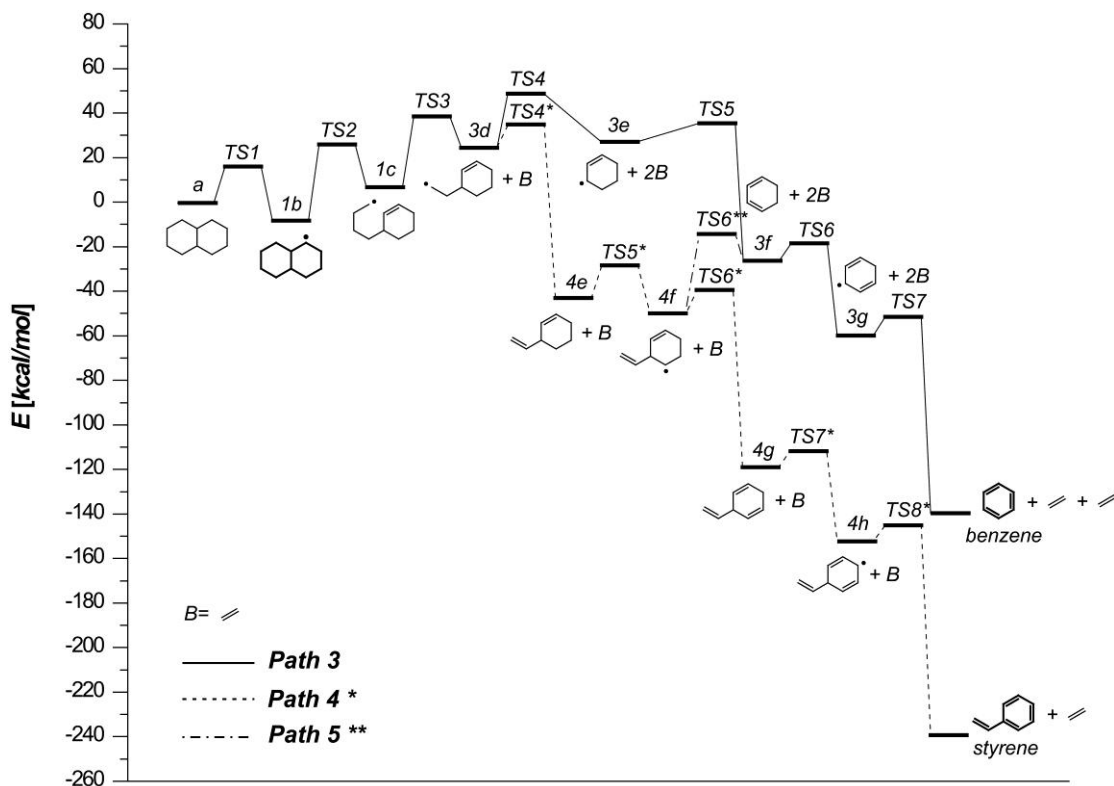


Figure 4.6 Potential energy diagrams for pathway 3, 4, and 5.

As an alternative, the species '3d' can undergo hydrogen abstraction to form the molecule '4e'. Styrene is then produced through hydrogen abstraction reactions, according to the route  $3d \rightarrow 4e \rightarrow 4f \rightarrow 4g \rightarrow 4h \rightarrow \text{styrene}$ . Decomposition of '4f' into '3f' and the vinyl radical ( $\text{C}_2\text{H}_3\cdot$ ) represents another pathway to form benzene (pathway 5). The energy barrier for  $4f \rightarrow 3f$  is 35.56 kcal/mol, higher than that of the  $3d \rightarrow 3e$  reaction, 22.48 kcal/mol. Benzene is then formed from '3f' following pathway 3 as previously described.

In Figure 4.7, pathway 6 that produces Ethylbenzene is illustrated. Intermediate '3d' undergoes hydrogen addition to produce '6e' with an energy

barrier of 20.92 kcal/mol energy. Subsequent hydrogen abstraction reactions produce ethylbenzene through the pathway '6e → 6f → 6g → 6h → ethylbenzene'.

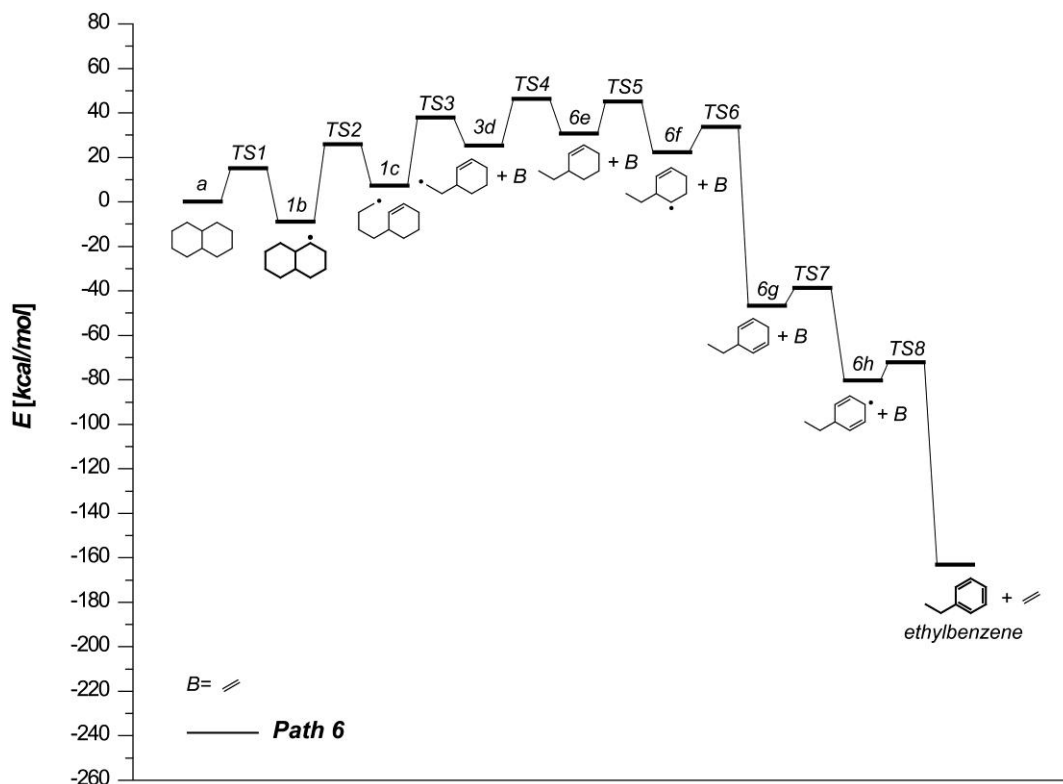


Figure 4.7 Potential energy diagram for pathway 6.

Pathways 7 and 8 that form benzene and styrene are illustrated in Figure 4.8. Radical '1b' undergoes C<sub>2</sub> – C<sub>3</sub> bond scission reaction to produce '7c'. This reaction has an energy barrier of 35.37 kcal/mol, similar to that of the C<sub>8</sub> – C<sub>9</sub> bond scission reaction of pathway 1, 34.62 kcal/mol. Two successive decomposition reactions first produce ethylene and '7d' and subsequently form the vinyl radical and '7e'. These are the peculiar steps of this pathway. The energy barrier for '7c → 7d' is 29.34 kcal/mol, which is very similar to that of reaction '1c → 3d' of pathway 3, 30.97

kcal/mol, but the '7d → 7e' reaction shows a high energy barrier, 35.49 kcal/mol. Subsequent hydrogen abstraction reactions produce benzene through the steps '7e → 7f → 7g → 3g → benzene'.

Pathway 8 proceeds from intermediate '7d' through hydrogen abstraction reactions to form styrene, through reactions '7d → 4e → 4f → 4g → 4h → styrene'.

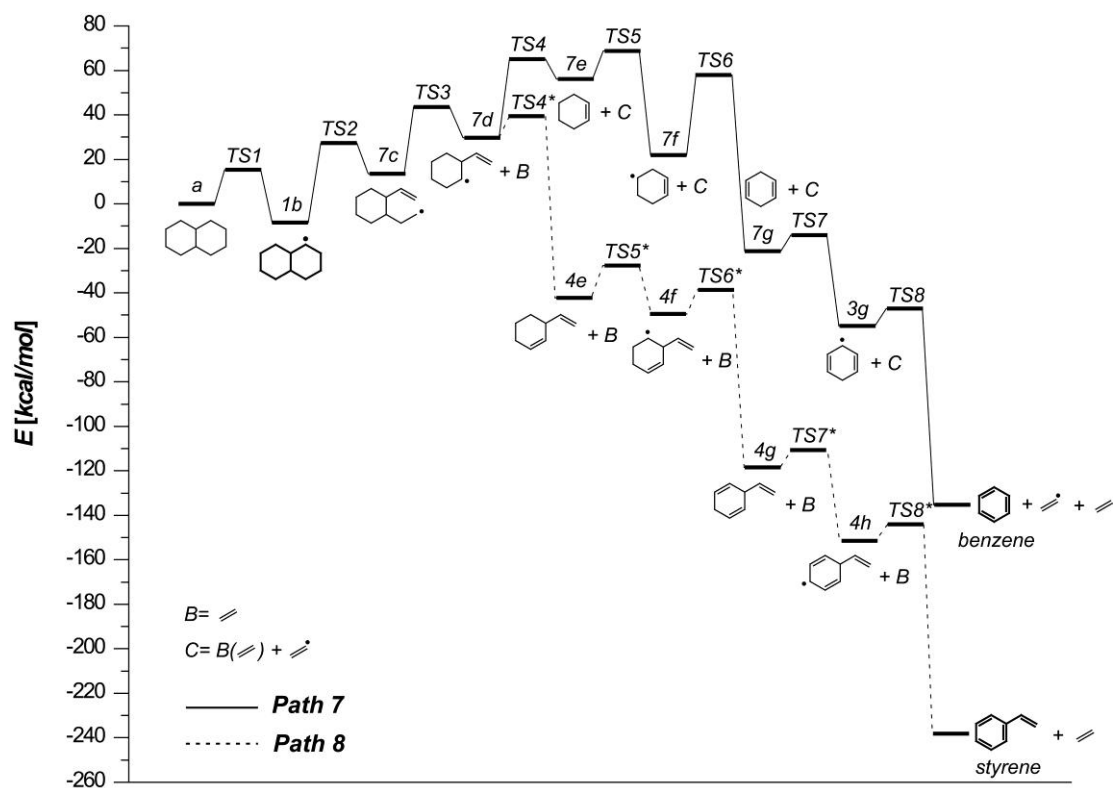


Figure 4.8 Potential energy diagrams for pathways 7 and 8.

Figure 4.9 reports the last decomposition pathway for the 1-decalyl radical. The '7c' undergoes hydrogen addition and abstraction to produce '9e'. The energies for reactions '7c → 9d' and '9d → 9e' are 22.46 kcal/mol and 14.75 kcal/mol, respectively. The '9e' decomposes to the vinyl radical and the species '9f', which has

a 34.88 kcal/mol energy barrier. Ethylbenzene is then produced through hydrogen abstraction reactions.

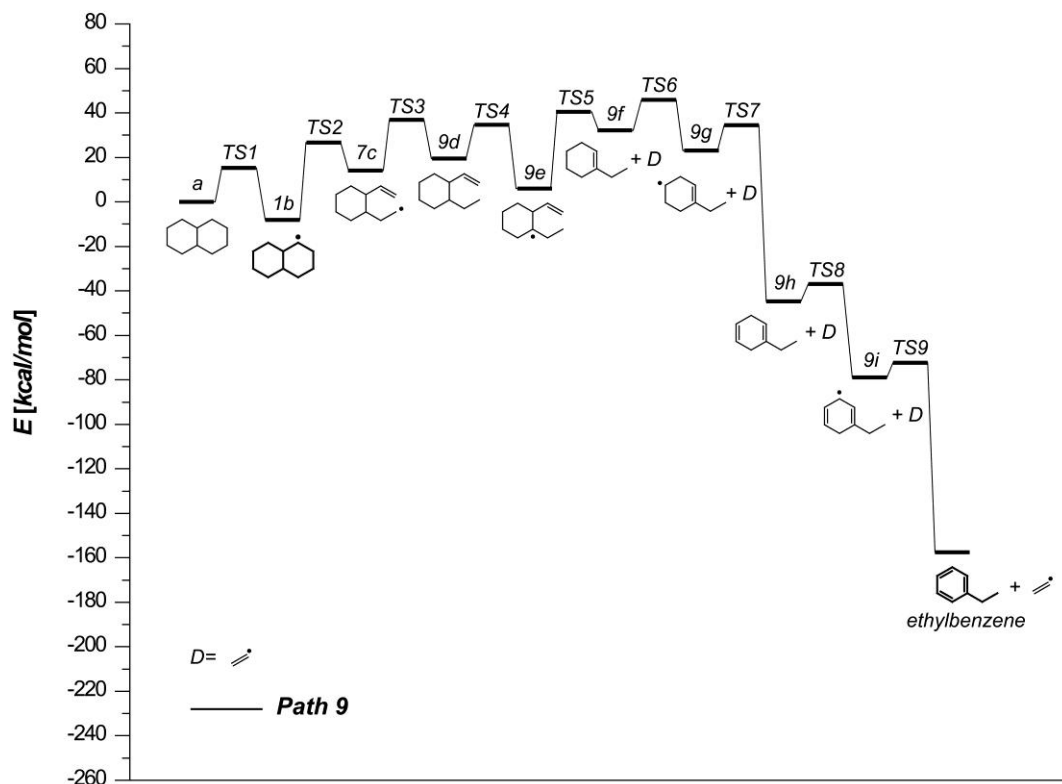


Figure 4.9 Potential energy diagram for pathway 9.

All identified reaction pathways from the 1-decalyl radical start with carbon – carbon bond scissions to open the ring structure. The products of these ring-opening reactions undergo several elementary reactions to form mono-aromatic molecules. Among these elementary reactions, hydrogen addition and migration are the key steps. The presence of either of those two reactions determines the products of their pathways. Benzene and styrene are obtained only from pathways that do



not include any hydrogen addition or migration reactions (pathways 3, 4, 5, 7 and 8). Conversely, hydrogen migration reactions are required to produce toluene (pathways 1 and 2). Similarly, ethylbenzene is produced from the pathways that include hydrogen addition reactions (pathways 6 and 9). These trends characterize the breakdown mechanisms of multi-ring cycloalkanes when compared with those of other hydrocarbon groups specifically, linear alkanes.

#### **4.3.4 Reaction pathways from 2-decalyl radical**

Two reaction pathways for the decomposition of the 2-decalyl radical are reported in Figure 4.10. The sequence begins with C<sub>3</sub> – C<sub>4</sub> bond scission (*'10b → 10c'*) to form *'10c'* and then undergoes hydrogen addition and abstraction to produce *'10e'*. An energy barrier of 17.81 kcal/mol is required to decompose *'10e'* into *'10f'* and the allyl radical (C<sub>3</sub>H<sub>5</sub>). Pathway 10 involves hydrogen abstraction reactions that lead to the formation of toluene, through the route *'10f → 10g → 10h → 10i → toluene'*.

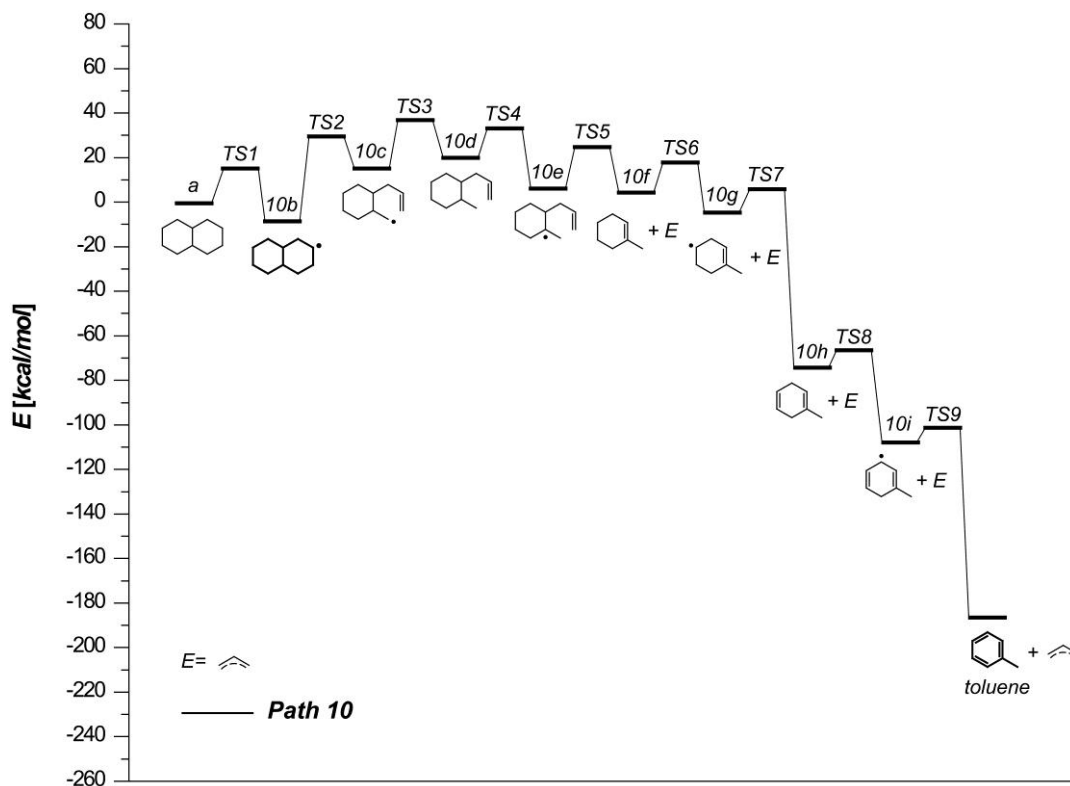


Figure 4.10 Potential energy diagram for pathway 10.

In Figure 4.11, the '10b' can produce '11c' through C<sub>1</sub> – C<sub>9</sub> bond scission. The energy barrier for this reaction, 34.64 kcal/mol, is slightly lower than that of '10b → 10c', 37.47 kcal/mol. The '11c' undergoes a decomposition reaction to produce C<sub>4</sub>H<sub>7</sub> and the '7e'. From the '7e', the pathway leads to the formation of benzene, analogous to pathway 7.

Similar to the pathways of the 1-decalyl radical, benzene is produced from a pathway which only consists of hydrogen abstraction and bond breaking reactions (pathway 11). However, the pathway for toluene includes hydrogen addition reactions right after C – C bond scission (pathway 10).

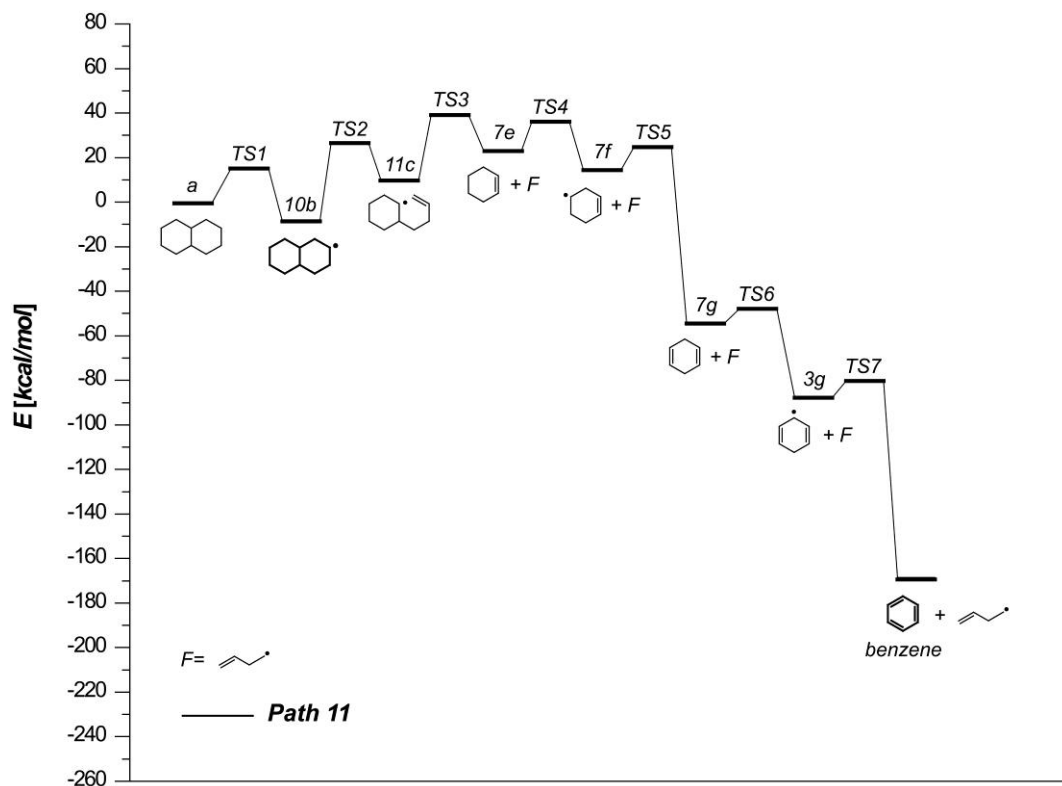


Figure 4.11 Potential energy diagram for pathway 11.

#### 4.3.5 Reaction pathways from 9-decalyl radical

Figure 4.12 shows reaction pathways for the 9-decalyl radical. The  $C_1 - C_2$  bond scission reaction ( $12b \rightarrow 12c$ ) requires 34.04 kcal/mol of energy to overcome the energy barrier and produce intermediate '12c'. This isomer radical ( $12c$ ) undergoes a decomposition reaction ( $12c \rightarrow 12d$ ) to form '12d' and ethylene. Successive hydrogen abstraction and addition reactions lead to the formation of xylene.

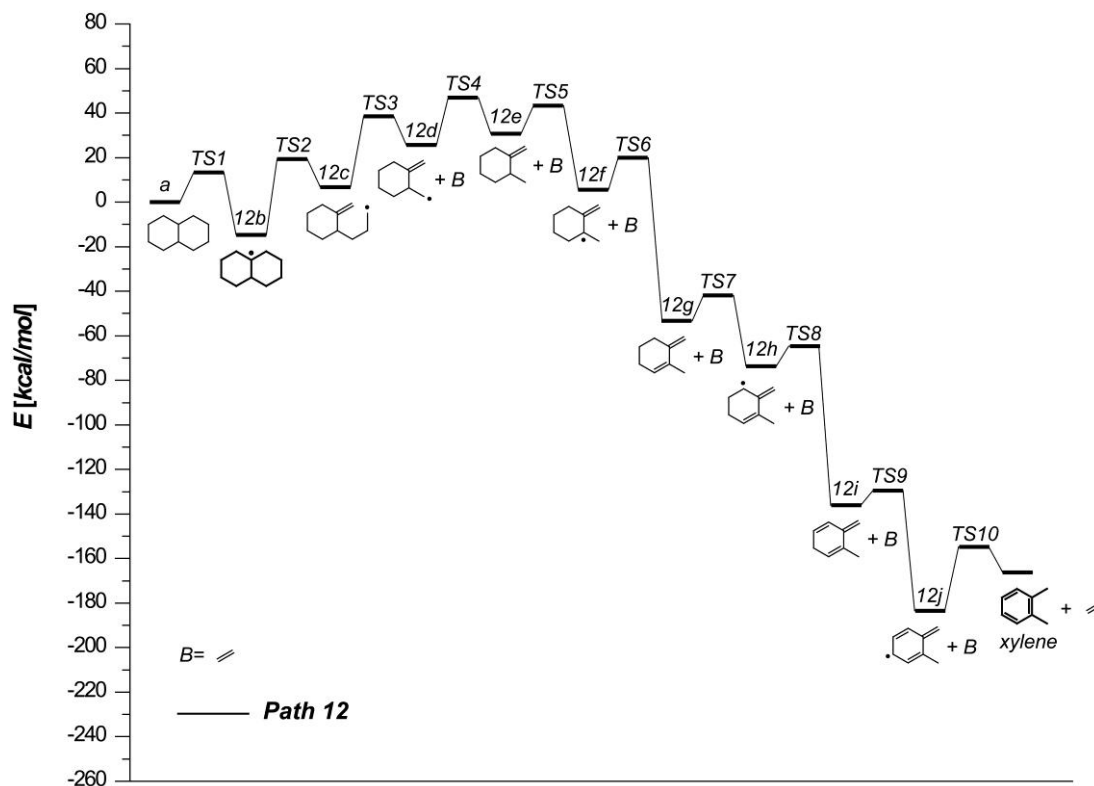


Figure 4.12 Potential energy diagram for pathway 12.

Alternatively, the '12c' can undergo hydrogen addition ( $12c \rightarrow 13d$ ), 21.87 kcal/mol, and hydrogen abstraction ( $13d \rightarrow 13e$ ), 14.86 kcal/mol, to produce the '13e'. Propyl and the '1e' are then formed from the decomposition of '13e'. From '1e', toluene is produced following the same reaction route described in pathways 1 and 2 (Figure 4.13).

The 9-decalyl radical produced xylene and toluene, and all of those pathways involve hydrogen addition reactions. From the reaction pathways of three decalyl radicals, we observed distinct features of the breakdown mechanisms of multi-ring cycloalkanes to form mono-aromatic ring molecules. As we showed, all decalyl radicals begin their breakdown with C - C bond scissions to open their aliphatic

rings. Subsequently based on their resultant structures, those radicals follow different pathways. Therefore obtaining accurate energy barriers of these ring opening reactions is critical in order to correctly identify reaction pathways of cycloalkane molecules. Another feature is the existence of hydrogen addition or hydrogen migration determines the aromatic products of their pathways. Benzene and styrene are produced only from the sequence of hydrogen abstractions and C – C bond breaking reactions. Most of toluene is obtained from the pathways that include a hydrogen migration reaction. The other products (ethylbenzene and xylene) contain hydrogen addition reactions in their pathways.

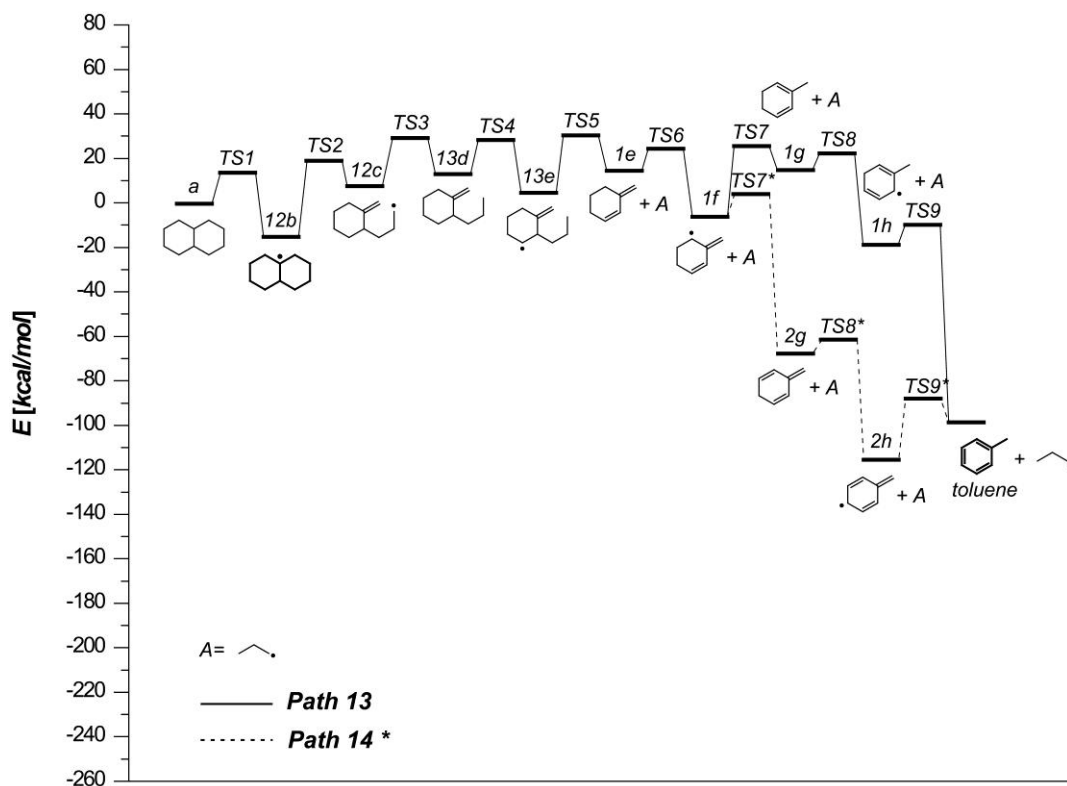


Figure 4.13 Potential energy diagram for pathways 13 and 14.

#### 4.4 Kinetic modeling

Reaction rate constants were obtained at different temperature condition by using the RRKM and TST methods. Computed high-pressure limit constants are listed in Tables C.1 to C.13 in the Appendix C. The resulting thermal rate constants are of reasonable accuracy as long as the high-pressure limit can adequately describe the target reaction conditions. For flame modeling at ambient pressure, the high-pressure limit approximation is generally valid, and therefore our computed rate constants can be used in detailed kinetic modeling of atmospheric combustion.

The newly identified reaction pathways for decalin breakdown and their relative reaction rates were implemented in a kinetic mechanism analysis code. The CHEMKIN software package<sup>[139, 140]</sup> was utilized to study the time-dependent chemical kinetics behavior of a closed homogeneous gas mixture system in the temperature range of 700K – 1500K and 1 atm. The mechanism includes all the reaction steps previously described. Table C.14 in the Appendix C reports the calculated product yields (%) of benzene, toluene, styrene, ethylbenzene and xylene as a function of temperature.

At low temperature conditions (700K), the major reaction product is benzene, which is formed mainly through pathways 3, 7 and 11. The pathway 11 accounts for most of the benzene production within the temperature ranges considered. At 700K, pathway 11 contributes 99% of benzene production and the value goes down to 76% at 1500K. The contribution of pathways 3 and 7 to benzene formation increases with temperature, reaching 8.55% and 14.69% at 1500K, respectively.

Toluene is produced through pathways 1 and 2. The other three routes leading to toluene, pathways 10, 13 and 14 are less significant. Pathways 13 and 14 compete with pathway 12 to form xylene and pathway 10 overcomes Path 11 to produce benzene. At low temperatures toluene is mainly formed through pathway 2 (99%). As the temperature increases the contribution of pathway 2 become less significant. As a result, pathway 1 contributes 67% and pathway 2 does 32% to the final yields of toluene at 1500K.

Benzene production reaches a minimum at 1000K, where the toluene yield peaks. The amounts formed of both of these two compounds are interdependent, as a result of the competition of pathways 1 and 7, in which the '1b' can form '1c' or '7c' to produce toluene or benzene, respectively.

Styrene is produced through pathway 8 and the overall yield is low compared with benzene and toluene. This result is due to the competition with pathways 3 and 7 that lead to the formation of benzene.

Ethylbenzene is formed through pathways 6 and 9. At low temperatures, pathway 9 represents the main production route for ethylbenzene. However at 1500K, pathway 6 accounts for 10% of the total yield. In the same way as styrene, ethylbenzene accounts for very small portion of products due to the competition with pathways 3 and 7.

Xylene is produced through pathway 12 and its yield increases as the temperature goes up. Its production, however, is below 1% in the temperature range analyzed.

The overall results demonstrate that hydrogen abstraction and C – C bond breaking reactions are energetically favorable than hydrogen abstraction and hydrogen migration reactions. These trends explain the preferential formation of benzene from the breakdown mechanisms of decalin.

#### **4.5 Conclusions**

Fourteen reaction pathways that connect decalin to five mono-aromatic species (benzene, toluene, styrene, ethylbenzene and xylene) were identified. The basic reactions for the new routes are carbon – carbon bond scission, dissociation, hydrogen abstraction and hydrogen addition. Reaction rate constant for each elementary reaction was computed and kinetic modeling analysis was also conducted to evaluate the relative importance of each pathway. The computed reaction pathways and their reaction rates can supply accurate kinetic data for combustion modeling under conditions where high pressure limit rates are applicable. Computed rate constants of decalin can be further incorporated in existing kinetic mechanisms for flame combustion and pyrolysis analysis to improve the prediction of aromatic concentrations.



## Chapter 5

### Conclusions

This study aimed at investigating molecular transport and chemical kinetic data of the components of jet fuel surrogates to improve the predictive capability of their combustion reaction mechanisms. We used molecular modeling approaches to compute and validate transport properties of various classes of hydrocarbons and employed *ab-initio* techniques to identify the breakdown mechanisms of decalin, a multi-ring cycloalkane component of fuel surrogates.

For molecular transport data, we first tested the validity of gas kinetic theory for polyatomic molecules. One major assumption in gas kinetic theory is the simplification of molecular configurations to spherical structures, which is potentially problematic for large polyatomic molecules. To understand the effect of this assumption, we compared gas kinetic theory with all-atom Molecular Dynamics simulations. Since atomistic level modeling treats all bonded and non-bonded interactions between atoms, it can be used to assess the effect of molecular

structures on transport properties. Therefore, we computed mutual mass diffusion coefficients of three hydrocarbon classes (linear alkanes, cycloalkanes and aromatic molecules) in nitrogen carrier gas using both MD simulations and the analytical equation of gas kinetic theory (Chapman-Enskog equation). This comparison reveals that the Chapman-Enskog (C-E) equation overestimates diffusion coefficients of the hydrocarbons considered in this study and the discrepancy increases as the molecules become non-spherical.

To better understand these results, we measured the effect of molecular configurations on mass diffusion coefficients by employing the radius of gyration (Rg). Since Rg reproduces the moment of inertia of the molecules, it is one of the simplest ways to represent vibrational and rotational information present in all-atom MD simulations. To measure the contribution of molecular structures to diffusion values, we related the computed Rg to the collision diameters obtained both from MD simulations ( $\sigma_{\text{MD}}$ ) and from the C-E equation ( $\sigma_{\text{C-E}}$ ). In this procedure, we observed that  $\sigma_{\text{C-E}}$  cannot be linearly related to the Rg. On the other hand,  $\sigma_{\text{MD}}$  produced much smaller deviations from the linear relation with Rg for all hydrocarbons. These results highlight the ability of MD simulations to take into account differences in molecular configurations and that the C-E equation cannot yield reliable diffusion coefficients especially for large molecules that have non-spherical structures.

To assess the relative importance on diffusion coefficients of molecular configurations with respect to the employed force field, we parameterized an equivalent single body potential from the multi body all atom force field. Free

energy calculations were conducted to identify the coexistence curves of systems in the liquid – gas transition region. From these data, we estimated the new potentials by using the correlations of corresponding state. Diffusion coefficients computed with these equivalent potentials were very similar to those from the C-E equation and showed large deviations from all-atom MD results. This comparison shows that although the equivalent spherical potentials were derived from the all-atom MD, thermodynamic properties cannot compensate for the lack of structural information. This also confirms that the assumption of spherical molecules in gas kinetic theory is not appropriate for polyatomic molecules and the molecular configurations have a dominant effect on transport properties. With our approach however, we were able to find a simple relation between molecular configuration and diffusion, relating  $R_g$  and collision diameters ( $\sigma_{MD}$  and  $\sigma_{C-E}$ ) for all the hydrocarbons. Hence we removed the limitations of the C-E equation by including the effect of molecular configurations.

The importance of this study lays not only in the improvement of existing data and methods but also in the fact that it suggests a simple general approach to deal correctly with new fuel components. Since standard gas kinetic theory and experiments can hardly give reliable or enough data for all the molecules that are of interest in hydrocarbon combustion or alternative fuels, accurate transport properties should be obtained through other methods. All-atom MD simulations can provide a simple and effective approach to overcome the above limitations and obtain diffusion coefficients for new realistic fuel components.

In the field of kinetic reactivity, we identified the breakdown mechanisms of decalin, a bi-cyclic naphthene commonly employed as a representative component of jet fuel surrogate. From *ab-initio* calculations, we obtained a total of fifteen possible reaction pathways that connect decalin to five mono-aromatic species (benzene, toluene, styrene, ethylbenzene and xylene). These reaction pathways are initiated by two elementary reactions, carbon bond cleavage reaction or hydrogen abstraction reactions. Each pathway connects the reactants to the products through a series of about ten reaction steps chosen among four elementary reactions (carbon bonds breaking reactions, dissociation reaction, hydrogen abstraction reactions, and hydrogen addition reaction). Electronic structures and energy states of all reactants, products, intermediates and transition states were explored for all the identified pathways. The activation energy of each reaction step and the geometry of all species were computed by using a hybrid density functional theory (B3LYP) and 6-31G(d,p) basis set.

From these data, we computed rate constants for the unimolecular and bimolecular reactions by using transition state theories in the temperature range of 700 – 1500K. The kinetic mechanism analysis shows the relative importance of each reaction pathways and concludes that benzene and toluene comprise around 99% in the product mixture. Computed rate constants of decalin can be further incorporated in existing kinetic mechanisms for flame combustion and pyrolysis analysis to improve the prediction of aromatic concentrations. Moreover, these findings can be used to understand the chemical reactions of cycloalkanes as a component of jet fuel surrogate.

## Appendices

### A. Supplementary tables of chapter 2

Table A.1 Mutual diffusion coefficients of  $n\text{-C}_7\text{H}_{16}/\text{N}_2$  mixtures for different system sizes at 1 atm.

Temp.	$D_{12}$ [ $\text{cm}^2/\text{s}$ ] [Number of molecules - $\text{C}_7\text{H}_{16}$ : $\text{N}_2$ ]			
	A (50 : 500)	B (100 : 1000)	C (300 : 3000)	D (500 : 5000)
500K	0.163	0.170	0.172	0.173
1000K	0.531	0.542	0.557	0.549

Table A.2 Mutual diffusion coefficients of  $n\text{-C}_3\text{H}_8/\text{N}_2$  and  $n\text{-C}_4\text{H}_{10}/\text{N}_2$  mixture at 1 atm and comparison with experimental data (MD: Molecular Dynamics simulations, EXP: experiment)

Temp.	$D_{12}$ [ $\text{cm}^2/\text{s}$ ]			
	$\text{C}_3\text{H}_8/\text{N}_2$		$\text{C}_4\text{H}_{10}/\text{N}_2$	
	MD	Exp	MD	Exp
573K	0.373±0.008	0.380	0.306±0.007	0.283
671K	0.483±0.009	0.502	0.401±0.010	0.351
725K	0.559±0.011	0.576		

Table A.3 Mutual diffusion coefficients of six heptane isomers in nitrogen at different temperatures, 1atm.

Mixture	$D_{12}$ [cm <sup>2</sup> /s]					
	500K	600K	700K	800K	900K	1000K
n-C <sub>7</sub> H <sub>16</sub> /N <sub>2</sub>	0.172	0.244	0.314	0.391	0.499	0.560
2-C <sub>7</sub> H <sub>16</sub> /N <sub>2</sub>	0.171	0.248	0.326	0.405	0.493	0.592
2,2-C <sub>7</sub> H <sub>16</sub> /N <sub>2</sub>	0.171	0.249	0.331	0.407	0.513	0.607
2,3-C <sub>7</sub> H <sub>16</sub> /N <sub>2</sub>	0.172	0.250	0.331	0.411	0.520	0.610
3,3-C <sub>7</sub> H <sub>16</sub> /N <sub>2</sub>	0.177	0.256	0.331	0.410	0.523	0.617
2,2,3-C <sub>7</sub> H <sub>16</sub> /N <sub>2</sub>	0.180	0.254	0.335	0.421	0.523	0.619

Table A.4 Mutual diffusion coefficients of normal alkanes in nitrogen as a function of temperature, at 1 atm, obtained from MD simulations.

Mixture	$D_{12}$ [cm <sup>2</sup> /s]	Mixture	$D_{12}$ [cm <sup>2</sup> /s]
CH <sub>4</sub> /N <sub>2</sub>	$1.588 \times 10^{-5} T^{1.679}$	C <sub>2</sub> H <sub>6</sub> /N <sub>2</sub>	$1.144 \times 10^{-5} T^{1.669}$
C <sub>3</sub> H <sub>8</sub> /N <sub>2</sub>	$9.319 \times 10^{-6} T^{1.667}$	C <sub>4</sub> H <sub>10</sub> /N <sub>2</sub>	$7.727 \times 10^{-6} T^{1.673}$
C <sub>5</sub> H <sub>12</sub> /N <sub>2</sub>	$6.706 \times 10^{-6} T^{1.669}$	C <sub>6</sub> H <sub>14</sub> /N <sub>2</sub>	$5.972 \times 10^{-6} T^{1.672}$
C <sub>7</sub> H <sub>16</sub> /N <sub>2</sub>	$5.295 \times 10^{-6} T^{1.674}$	C <sub>8</sub> H <sub>18</sub> /N <sub>2</sub>	$4.993 \times 10^{-6} T^{1.671}$
C <sub>9</sub> H <sub>20</sub> /N <sub>2</sub>	$4.678 \times 10^{-6} T^{1.667}$	C <sub>10</sub> H <sub>22</sub> /N <sub>2</sub>	$4.006 \times 10^{-6} T^{1.681}$
C <sub>11</sub> H <sub>24</sub> /N <sub>2</sub>	$3.560 \times 10^{-6} T^{1.688}$	C <sub>12</sub> H <sub>26</sub> /N <sub>2</sub>	$3.508 \times 10^{-6} T^{1.679}$
C <sub>13</sub> H <sub>28</sub> /N <sub>2</sub>	$3.309 \times 10^{-6} T^{1.678}$	C <sub>14</sub> H <sub>30</sub> /N <sub>2</sub>	$3.016 \times 10^{-6} T^{1.686}$
C <sub>15</sub> H <sub>32</sub> /N <sub>2</sub>	$2.667 \times 10^{-6} T^{1.691}$	C <sub>16</sub> H <sub>34</sub> /N <sub>2</sub>	$2.620 \times 10^{-6} T^{1.693}$

Table A.5 Mutual diffusion coefficients of cycloalkanes in nitrogen as a function of temperature, at 1 atm, obtained from MD simulations.

Mixture	$D_{12}$ [cm <sup>2</sup> /s]	Mixture	$D_{12}$ [cm <sup>2</sup> /s]
C <sub>7</sub> H <sub>14</sub> /N <sub>2</sub>	$2.695 \times 10^{-6} T^{1.7882}$	C <sub>11</sub> H <sub>22</sub> /N <sub>2</sub>	$1.852 \times 10^{-6} T^{1.7924}$
C <sub>8</sub> H <sub>16</sub> /N <sub>2</sub>	$2.492 \times 10^{-6} T^{1.7823}$	C <sub>12</sub> H <sub>24</sub> /N <sub>2</sub>	$1.764 \times 10^{-6} T^{1.7919}$
C <sub>9</sub> H <sub>18</sub> /N <sub>2</sub>	$2.239 \times 10^{-6} T^{1.7874}$	C <sub>13</sub> H <sub>26</sub> /N <sub>2</sub>	$1.611 \times 10^{-6} T^{1.7938}$
C <sub>10</sub> H <sub>20</sub> /N <sub>2</sub>	$2.041 \times 10^{-6} T^{1.7911}$	C <sub>14</sub> H <sub>28</sub> /N <sub>2</sub>	$1.520 \times 10^{-6} T^{1.7931}$

Table A.6 Mutual diffusion coefficients of aromatic molecules in nitrogen as a function of temperature, at 1 atm, obtained from MD simulations.

Mixture	$D_{12}$ [cm <sup>2</sup> /s]	Mixture	$D_{12}$ [cm <sup>2</sup> /s]
C <sub>6</sub> H <sub>6</sub> /N <sub>2</sub>	$3.599 \times 10^{-6} T^{1.7829}$	C <sub>16</sub> H <sub>10</sub> /N <sub>2</sub>	$1.744 \times 10^{-6} T^{1.7953}$
C <sub>10</sub> H <sub>8</sub> /N <sub>2</sub>	$2.539 \times 10^{-6} T^{1.7835}$	C <sub>18</sub> H <sub>12</sub> -a/N <sub>2</sub>	$1.501 \times 10^{-6} T^{1.7966}$
C <sub>14</sub> H <sub>10</sub> -a/N <sub>2</sub>	$1.902 \times 10^{-6} T^{1.7914}$	C <sub>18</sub> H <sub>12</sub> -b/N <sub>2</sub>	$1.592 \times 10^{-6} T^{1.7944}$
C <sub>14</sub> H <sub>10</sub> -b/N <sub>2</sub>	$1.961 \times 10^{-6} T^{1.7937}$	C <sub>18</sub> H <sub>12</sub> -c/N <sub>2</sub>	$1.572 \times 10^{-6} T^{1.7941}$
		C <sub>18</sub> H <sub>12</sub> -d/N <sub>2</sub>	$1.652 \times 10^{-6} T^{1.7937}$

Table A.7 Thermodynamic properties and derived potential parameters of linear alkanes

Molecules	$T_c$ [K]	$P_c$ [atm]	$T_b$ [K]	$\sigma$ [Å]	$\epsilon/k_B$ [K]
CH <sub>4</sub>	190.6	45.49	111.0	3.793	153.0
C <sub>2</sub> H <sub>6</sub>	305.3	48.35	184.6	4.274	266.2
C <sub>3</sub> H <sub>8</sub>	369.9	41.94	231.0	4.737	335.2
C <sub>4</sub> H <sub>10</sub>	425.0	37.50	273.0	5.102	400.8
C <sub>5</sub> H <sub>12</sub>	469.8	33.15	309.2	5.454	457.2
C <sub>6</sub> H <sub>14</sub>	507.6	29.80	341.9	5.747	511.5
C <sub>7</sub> H <sub>16</sub>	540.0	27.04	371.5	6.004	563.3
C <sub>8</sub> H <sub>18</sub>	568.9	24.57	398.7	6.256	611.4
C <sub>9</sub> H <sub>20</sub>	595.0	22.69	423.8	6.466	658.2
C <sub>10</sub> H <sub>22</sub>	617.8	20.82	447.2	6.680	703.2
C <sub>11</sub> H <sub>24</sub>	639.0	19.54	468.0	6.855	743.1
C <sub>12</sub> H <sub>26</sub>	658.2	17.76	489.0	7.096	782.6
C <sub>13</sub> H <sub>28</sub>	676.0	16.77	507.0	7.256	817.8
C <sub>14</sub> H <sub>30</sub>	693.0	15.79	523.0	7.455	841.7
C <sub>15</sub> H <sub>32</sub>	708.0	14.80	540.0	7.619	877.5
C <sub>16</sub> H <sub>34</sub>	722.0	13.83	554.0	7.841	895.8



Table A.8 Thermodynamic properties and derived potential parameters of cycloalkanes

Molecules	$T_c$ [K]	$P_c$ [atm]	$T_b$ [K]	$\sigma$ [Å]	$\epsilon/k_B$ [K]
$C_7H_{14}$	573.0	34.34	374.0	5.777	550.6
$C_8H_{16}$	609.0	30.00	405.0	6.144	594.1
$C_9H_{18}$	639.2	27.73	429.0	6.403	626.4
$C_{10}H_{20}$	667.1	25.36	453.0	6.675	659.6
$C_{11}H_{22}$	683.3	23.11	472.1	6.899	691.8
$C_{12}H_{24}$	700.2	21.36	493.8	7.065	737.5
$C_{13}H_{26}$	715.2	19.84	514.4	7.206	785.2
$C_{14}H_{28}$	728.6	18.52	534.1	7.321	836.1

Table A.9 Thermodynamic properties and derived potential parameters of aromatic molecules

Molecules	$T_c$ [K]	$P_c$ [atm]	$T_b$ [K]	$\sigma$ [Å]	$\epsilon/k_B$ [K]
$C_6H_6$	562	48.25	353.1	5.144	531.9
$C_{10}H_8$	748	40.46	490.0	5.907	753.5
$C_{14}H_{10}$ -a	873	28.62	613.0	6.764	983.5
$C_{14}H_{10}$ -b	869	28.62	609.2	6.764	974.0
$C_{16}H_{10}$	936	25.75	667.9	7.119	1079.3
$C_{18}H_{12}$ -a	987	23.58	716.2	7.387	1174.9

Table A.10 Mutual diffusion coefficients of linear alkanes in nitrogen as a function of temperature at 1 atm, obtained from the C-E equation.

Mixture	$D_{12}$ [cm <sup>2</sup> /s]	Mixture	$D_{12}$ [cm <sup>2</sup> /s]
CH <sub>4</sub> /N <sub>2</sub>	$1.483 \times 10^{-5} T^{1.6923}$	C <sub>2</sub> H <sub>6</sub> /N <sub>2</sub>	$8.982 \times 10^{-6} T^{1.7139}$
C <sub>3</sub> H <sub>8</sub> /N <sub>2</sub>	$6.668 \times 10^{-6} T^{1.7252}$	C <sub>4</sub> H <sub>10</sub> /N <sub>2</sub>	$5.354 \times 10^{-6} T^{1.7349}$
C <sub>5</sub> H <sub>12</sub> /N <sub>2</sub>	$4.469 \times 10^{-6} T^{1.7429}$	C <sub>6</sub> H <sub>14</sub> /N <sub>2</sub>	$3.844 \times 10^{-6} T^{1.7504}$
C <sub>7</sub> H <sub>16</sub> /N <sub>2</sub>	$3.376 \times 10^{-6} T^{1.7573}$	C <sub>8</sub> H <sub>18</sub> /N <sub>2</sub>	$3.001 \times 10^{-6} T^{1.7636}$
C <sub>9</sub> H <sub>20</sub> /N <sub>2</sub>	$2.716 \times 10^{-6} T^{1.7692}$	C <sub>10</sub> H <sub>22</sub> /N <sub>2</sub>	$2.471 \times 10^{-6} T^{1.7743}$
C <sub>11</sub> H <sub>24</sub> /N <sub>2</sub>	$2.285 \times 10^{-6} T^{1.7788}$	C <sub>12</sub> H <sub>26</sub> /N <sub>2</sub>	$2.082 \times 10^{-6} T^{1.7839}$
C <sub>13</sub> H <sub>28</sub> /N <sub>2</sub>	$1.949 \times 10^{-6} T^{1.7876}$	C <sub>14</sub> H <sub>30</sub> /N <sub>2</sub>	$2.083 \times 10^{-6} T^{1.7839}$
C <sub>15</sub> H <sub>32</sub> /N <sub>2</sub>	$1.723 \times 10^{-6} T^{1.7934}$	C <sub>16</sub> H <sub>34</sub> /N <sub>2</sub>	$1.833 \times 10^{-6} T^{1.7900}$

Table A.11 Mutual diffusion coefficients of cycloalkanes in nitrogen as a function of temperature at 1 atm, obtained from the C-E equation.

Mixture	$D_{12}$ [cm <sup>2</sup> /s]	Mixture	$D_{12}$ [cm <sup>2</sup> /s]
C <sub>7</sub> H <sub>14</sub> /N <sub>2</sub>	$3.604 \times 10^{-6} T^{1.7554}$	C <sub>11</sub> H <sub>22</sub> /N <sub>2</sub>	$2.377 \times 10^{-6} T^{1.7732}$
C <sub>8</sub> H <sub>16</sub> /N <sub>2</sub>	$3.137 \times 10^{-6} T^{1.7611}$	C <sub>12</sub> H <sub>24</sub> /N <sub>2</sub>	$2.190 \times 10^{-6} T^{1.7786}$
C <sub>9</sub> H <sub>18</sub> /N <sub>2</sub>	$2.844 \times 10^{-6} T^{1.7653}$	C <sub>13</sub> H <sub>26</sub> /N <sub>2</sub>	$2.028 \times 10^{-6} T^{1.7839}$
C <sub>10</sub> H <sub>20</sub> /N <sub>2</sub>	$2.585 \times 10^{-6} T^{1.7692}$	C <sub>14</sub> H <sub>28</sub> /N <sub>2</sub>	$1.888 \times 10^{-6} T^{1.7896}$

Table A.12 Mutual diffusion coefficients of aromatic molecules in nitrogen as a function of temperature at 1 atm, obtained from the C-E equation.

Mixture	$D_{12}$ [cm <sup>2</sup> /s]
C <sub>6</sub> H <sub>6</sub> /N <sub>2</sub>	$4.347 \times 10^{-6} T^{1.7530}$
C <sub>10</sub> H <sub>8</sub> /N <sub>2</sub>	$2.782 \times 10^{-6} T^{1.7799}$
C <sub>14</sub> H <sub>10-a</sub> /N <sub>2</sub>	$1.866 \times 10^{-6} T^{1.8043}$
C <sub>14</sub> H <sub>10-b</sub> /N <sub>2</sub>	$1.877 \times 10^{-6} T^{1.8036}$
C <sub>16</sub> H <sub>10</sub> /N <sub>2</sub>	$1.600 \times 10^{-6} T^{1.8139}$
C <sub>18</sub> H <sub>12-a</sub> /N <sub>2</sub>	$1.413 \times 10^{-6} T^{1.8221}$

Table A.13 Average radius of gyrations linear alkanes obtained with MD simulations.

Species	Rg [Å]	Species	Rg [Å]
CH <sub>4</sub>	0.549	C <sub>2</sub> H <sub>6</sub>	0.978
C <sub>3</sub> H <sub>8</sub>	1.299	C <sub>4</sub> H <sub>10</sub>	1.617
C <sub>5</sub> H <sub>12</sub>	1.932	C <sub>6</sub> H <sub>14</sub>	2.244
C <sub>7</sub> H <sub>16</sub>	2.541	C <sub>8</sub> H <sub>18</sub>	2.845
C <sub>9</sub> H <sub>20</sub>	3.134	C <sub>10</sub> H <sub>22</sub>	3.421
C <sub>11</sub> H <sub>24</sub>	3.693	C <sub>12</sub> H <sub>26</sub>	3.951
C <sub>13</sub> H <sub>28</sub>	4.228	C <sub>14</sub> H <sub>30</sub>	4.484
C <sub>15</sub> H <sub>32</sub>	4.730	C <sub>16</sub> H <sub>34</sub>	4.978

Table A.14 New collision diameters ( $\sigma_{MD}$ ) of linear alkanes.

Species	$\sigma_{MD}$ [Å]	Species	$\sigma_{MD}$ [Å]
CH <sub>4</sub>	3.849	C <sub>2</sub> H <sub>6</sub>	4.481
C <sub>3</sub> H <sub>8</sub>	4.935	C <sub>4</sub> H <sub>10</sub>	5.288
C <sub>5</sub> H <sub>12</sub>	5.821	C <sub>6</sub> H <sub>14</sub>	6.094
C <sub>7</sub> H <sub>16</sub>	6.517	C <sub>8</sub> H <sub>18</sub>	6.812
C <sub>9</sub> H <sub>20</sub>	7.147	C <sub>10</sub> H <sub>22</sub>	7.441
C <sub>11</sub> H <sub>24</sub>	7.747	C <sub>12</sub> H <sub>26</sub>	8.081
C <sub>13</sub> H <sub>28</sub>	8.427	C <sub>14</sub> H <sub>30</sub>	8.598
C <sub>15</sub> H <sub>32</sub>	8.973	C <sub>16</sub> H <sub>34</sub>	9.099

Table A.15 New collision diameters ( $\sigma_{MD}$ ) of cycloalkanes.

Species	$\sigma_{MD}$ [Å]	Species	$\sigma_{MD}$ [Å]
C <sub>7</sub> H <sub>14</sub>	6.135	C <sub>11</sub> H <sub>22</sub>	7.516
C <sub>8</sub> H <sub>16</sub>	6.545	C <sub>12</sub> H <sub>24</sub>	7.736
C <sub>9</sub> H <sub>18</sub>	6.859	C <sub>13</sub> H <sub>26</sub>	8.059
C <sub>10</sub> H <sub>20</sub>	7.187	C <sub>14</sub> H <sub>28</sub>	8.350

Table A.16 Average radius of gyration of cycloalkanes obtained with MD simulations.

Species	Rg [Å]	Species	Rg [Å]
C <sub>7</sub> H <sub>14</sub>	1.856	C <sub>11</sub> H <sub>22</sub>	3.084
C <sub>8</sub> H <sub>16</sub>	2.129	C <sub>12</sub> H <sub>24</sub>	3.391
C <sub>9</sub> H <sub>18</sub>	2.446	C <sub>13</sub> H <sub>26</sub>	3.695
C <sub>10</sub> H <sub>20</sub>	2.765	C <sub>14</sub> H <sub>28</sub>	3.988

Table A.17 New collision diameters ( $\sigma_{MD}$ ) of aromatic molecules.

Species	$\sigma_{MD}$ [Å]	Species	$\sigma_{MD}$ [Å]
C <sub>6</sub> H <sub>6</sub>	5.110	C <sub>18</sub> H <sub>12</sub> -a	7.991
C <sub>10</sub> H <sub>8</sub>	6.279	C <sub>18</sub> H <sub>12</sub> -b	7.708
C <sub>14</sub> H <sub>10</sub> -a	7.158	C <sub>18</sub> H <sub>12</sub> -c	7.803
C <sub>14</sub> H <sub>10</sub> -b	6.858	C <sub>18</sub> H <sub>12</sub> -d	7.534
C <sub>16</sub> H <sub>10</sub>	7.297		

Table A.18 Average radius of gyration of aromatic molecules obtained with MD simulations.

Species	Rg [Å]	Species	Rg [Å]
C <sub>6</sub> H <sub>6</sub>	1.528	C <sub>18</sub> H <sub>12</sub> -a	3.586
C <sub>10</sub> H <sub>8</sub>	2.196	C <sub>18</sub> H <sub>12</sub> -b	3.402
C <sub>14</sub> H <sub>10</sub> -a	2.883	C <sub>18</sub> H <sub>12</sub> -c	3.333
C <sub>14</sub> H <sub>10</sub> -b	2.744	C <sub>18</sub> H <sub>12</sub> -d	3.082
C <sub>16</sub> H <sub>10</sub>	2.778		

## B. Supplementary tables of chapter 3

Table B.1 Estimated errors for all  $\lambda$  of Figure 3.1.

$\lambda$	$\frac{\partial U(\lambda)}{\partial \lambda}$ [KJ/mol]	Error [KJ/mol]
0.0	3.074	0.260
0.1	2.849	0.223
0.2	2.669	0.175
0.3	2.411	0.160
0.4	2.168	0.136
0.5	2.032	0.168
0.6	1.645	0.145
0.7	1.325	0.142
0.8	0.886	0.176
0.9	0.199	0.242
1.0	-0.331	0.242
Integration	1.756	

Table B.2 Equilibrium vapor pressure ( $P_{\text{sat}}$ ), liquid ( $\rho_{\text{liq}}$ ) and vapor densities ( $\rho_{\text{vap}}$ ) of linear alkanes obtained from MD simulations.

	CH <sub>4</sub>			C <sub>2</sub> H <sub>6</sub>		
Temp [K]	150	160	170	270	280	290
$P_{\text{sat}}$ [bar]	9.7	15.4	22.5	21.4	27.1	33.4
$\rho_{\text{liq}}$ [kg/m <sup>3</sup> ]	222.7	214.9	206.2	245.8	237.2	226.5
$\rho_{\text{vap}}$ [kg/m <sup>3</sup> ]	13.9	22.3	33.2	33.9	42.2	52.3
	C <sub>3</sub> H <sub>8</sub>			C <sub>4</sub> H <sub>10</sub>		
Temp [K]	330	340	350	380	390	400
$P_{\text{sat}}$ [bar]	18.4	22.5	27.2	15.9	19.2	22.3
$\rho_{\text{liq}}$ [kg/m <sup>3</sup> ]	271.7	263.7	252.5	281.5	273.5	263.1
$\rho_{\text{vap}}$ [kg/m <sup>3</sup> ]	33.9	42.7	51.4	34.1	40.2	45.9
	C <sub>5</sub> H <sub>12</sub>			C <sub>6</sub> H <sub>14</sub>		
Temp [K]	420	430	440	450	460	470
$P_{\text{sat}}$ [bar]	13.6	16.3	19.1	11.0	13.1	15.5
$\rho_{\text{liq}}$ [kg/m <sup>3</sup> ]	303.5	294.3	282.9	320.9	311.6	301.1
$\rho_{\text{vap}}$ [kg/m <sup>3</sup> ]	33.5	39.5	45.5	27.9	32.4	37.2
	C <sub>7</sub> H <sub>16</sub>			C <sub>8</sub> H <sub>18</sub>		
Temp [K]	500	510	520	530	540	550
$P_{\text{sat}}$ [bar]	13.7	16.2	18.5	13.0	15.1	17.6
$\rho_{\text{liq}}$ [kg/m <sup>3</sup> ]	300.2	290.3	276.0	327.5	309.6	286.8
$\rho_{\text{vap}}$ [kg/m <sup>3</sup> ]	39.9	48.8	56.9	42.1	48.4	55.6

	C <sub>9</sub> H <sub>20</sub>			C <sub>10</sub> H <sub>22</sub>		
Temp [K]	540	550	560	560	570	580
P <sub>sat</sub> [bar]	9.4	10.9	12.3	8.2	9.6	11.5
ρ <sub>liq</sub> [kg/m <sup>3</sup> ]	326.4	317.6	305.9	274.0	266.8	259.9
ρ <sub>vap</sub> [kg/m <sup>3</sup> ]	31.3	37.0	41.7	30.1	35.7	43.4
	C <sub>11</sub> H <sub>24</sub>			C <sub>12</sub> H <sub>26</sub>		
Temp [K]	580	590	600	610	620	630
P <sub>sat</sub> [bar]	7.4	8.8	10.0	8.4	9.9	11.2
ρ <sub>liq</sub> [kg/m <sup>3</sup> ]	299.1	292.2	283.3	301.1	292.9	280.9
ρ <sub>vap</sub> [kg/m <sup>3</sup> ]	27.5	33.1	38.1	33.6	40.5	45.8
	C <sub>13</sub> H <sub>28</sub>			C <sub>14</sub> H <sub>30</sub>		
Temp [K]	630	640	650	650	660	670
P <sub>sat</sub> [bar]	8.1	9.2	10.5	8.0	9.3	10.7
ρ <sub>liq</sub> [kg/m <sup>3</sup> ]	286.7	278.0	268.4	286.2	275.0	260.4
ρ <sub>vap</sub> [kg/m <sup>3</sup> ]	33.4	38.4	44.2	35.1	40.9	46.6
	C <sub>15</sub> H <sub>32</sub>			C <sub>16</sub> H <sub>34</sub>		
Temp [K]	650	660	670	670	680	690
P <sub>sat</sub> [bar]	6.0	7.1	8.0	6.2	7.1	8.1
ρ <sub>liq</sub> [kg/m <sup>3</sup> ]	293.4	286.9	278.1	298.3	289.3	277.7
ρ <sub>vap</sub> [kg/m <sup>3</sup> ]	26.0	31.7	36.2	28.6	34.3	39.3



Table B.3 Equilibrium vapor pressure ( $P_{\text{sat}}$ ), liquid ( $\rho_{\text{liq}}$ ) and vapor densities ( $\rho_{\text{vap}}$ ) of cycloalkanes obtained from MD simulations.

	C <sub>7</sub> H <sub>14</sub>			C <sub>8</sub> H <sub>16</sub>		
Temp [K]	530	540	550	560	570	580
$P_{\text{sat}}$ [bar]	17.0	20.1	22.7	15.0	17.1	19.0
$\rho_{\text{liq}}$ [kg/m <sup>3</sup> ]	354.7	341.8	322.9	369.5	356.3	339.7
$\rho_{\text{vap}}$ [kg/m <sup>3</sup> ]	46.3	54.2	59.8	42.9	47.9	52.3
	C <sub>9</sub> H <sub>18</sub>			C <sub>10</sub> H <sub>20</sub>		
Temp [K]	590	600	610	620	630	640
$P_{\text{sat}}$ [bar]	14.3	16.1	17.9	13.9	15.7	17.4
$\rho_{\text{liq}}$ [kg/m <sup>3</sup> ]	336.1	325.3	313.2	349.5	336.5	321.1
$\rho_{\text{vap}}$ [kg/m <sup>3</sup> ]	44.1	48.6	53.8	45.6	50.3	55.4
	C <sub>11</sub> H <sub>22</sub>			C <sub>12</sub> H <sub>24</sub>		
Temp [K]	630	640	650	650	660	670
$P_{\text{sat}}$ [bar]	10.5	12.2	13.5	8.7	10.4	11.7
$\rho_{\text{liq}}$ [kg/m <sup>3</sup> ]	350.7	342.5	331.1	364.8	351.9	338.7
$\rho_{\text{vap}}$ [kg/m <sup>3</sup> ]	35.9	41.7	45.7	34.1	37.0	41.6
	C <sub>13</sub> H <sub>26</sub>			C <sub>14</sub> H <sub>28</sub>		
Temp [K]	660	670	680	670	680	690
$P_{\text{sat}}$ [bar]	8.1	9.3	10.5	7.7	8.9	10.1
$\rho_{\text{liq}}$ [kg/m <sup>3</sup> ]	367.9	356.5	343.2	347.9	339.2	328.7
$\rho_{\text{vap}}$ [kg/m <sup>3</sup> ]	31.2	35.6	39.7	31.7	36.6	41.0

Table B.4 Equilibrium vapor pressure ( $P_{\text{sat}}$ ), liquid ( $\rho_{\text{liq}}$ ) and vapor densities ( $\rho_{\text{vap}}$ ) of aromatic molecules obtained from MD simulations.

	C <sub>6</sub> H <sub>6</sub>			C <sub>10</sub> H <sub>8</sub>		
Temp [K]	520	530	540	700	710	720
$P_{\text{sat}}$ [bar]	26.8	29.9	34.2	22.5	24.2	26.7
$\rho_{\text{liq}}$ [kg/m <sup>3</sup> ]	455.9	432.5	406.1	458.9	440.1	420.9
$\rho_{\text{vap}}$ [kg/m <sup>3</sup> ]	56.5	61.5	69.1	57.5	60.4	65.9
	C <sub>14</sub> H <sub>10</sub> -a			C <sub>14</sub> H <sub>10</sub> -b		
Temp [K]	830	840	850	830	840	850
$P_{\text{sat}}$ [bar]	16.7	18.5	20.3	16.6	18.5	20.2
$\rho_{\text{liq}}$ [kg/m <sup>3</sup> ]	489.6	471.1	449.1	488.9	471.1	450.2
$\rho_{\text{vap}}$ [kg/m <sup>3</sup> ]	50.1	55.1	59.7	50.0	55.1	59.6
	C <sub>16</sub> H <sub>10</sub>			C <sub>18</sub> H <sub>12</sub> -a		
Temp [K]	890	900	910	910	920	930
$P_{\text{sat}}$ [bar]	14.9	16.5	18.2	10.7	11.7	12.9
$\rho_{\text{liq}}$ [kg/m <sup>3</sup> ]	478.6	459.8	437.4	501.6	486.9	471.5
$\rho_{\text{vap}}$ [kg/m <sup>3</sup> ]	46.8	51.7	56.0	36.0	39.6	43.9
	C <sub>18</sub> H <sub>12</sub> -b			C <sub>18</sub> H <sub>12</sub> -c		
Temp [K]	910	920	930	910	920	930
$P_{\text{sat}}$ [bar]	10.9	11.8	13.0	10.8	11.7	13.0
$\rho_{\text{liq}}$ [kg/m <sup>3</sup> ]	500.7	487.4	472.3	501.8	487.2	471.8
$\rho_{\text{vap}}$ [kg/m <sup>3</sup> ]	35.9	39.5	44.0	36.0	39.7	44.0
	C <sub>18</sub> H <sub>12</sub> -d					
Temp [K]	910	920	930			
$P_{\text{sat}}$ [bar]	10.8	11.8	12.9			
$\rho_{\text{liq}}$ [kg/m <sup>3</sup> ]	501.2	486.8	472.1			
$\rho_{\text{vap}}$ [kg/m <sup>3</sup> ]	35.8	39.5	43.8			

Table B.5 Critical pressures ( $P_c$ ), critical temperatures ( $T_c$ ) and normal boiling temperatures ( $T_b$ ) of linear alkanes. MD denotes Molecular Dynamics simulations and EXP represents experimental data.

	MD			EXP		
	$T_c$ [K]	$P_c$ [atm]	$T_b$ [K]	$T_c$ [K]	$P_c$ [atm]	$T_b$ [K]
CH <sub>4</sub>	195.5	47.0	112.4	190.6	46.0	111.7
C <sub>2</sub> H <sub>6</sub>	314.2	47.9	171.1	305.3	48.7	184.5
C <sub>3</sub> H <sub>8</sub>	379.6	40.8	228.2	369.8	42.5	231.1
C <sub>4</sub> H <sub>10</sub>	440.6	38.1	262.7	425.1	37.9	272.6
C <sub>5</sub> H <sub>12</sub>	482.4	32.9	304.7	469.7	33.7	309.2
C <sub>6</sub> H <sub>14</sub>	530.2	30.7	334.3	507.6	30.3	341.9
C <sub>7</sub> H <sub>16</sub>	548.6	26.0	364.1	540.2	27.4	371.6
C <sub>8</sub> H <sub>18</sub>	572.5	23.6	405.5	568.7	24.9	398.8
C <sub>9</sub> H <sub>20</sub>	609.4	22.2	424.9	594.6	22.9	423.9
C <sub>10</sub> H <sub>22</sub>	626.0	19.1	451.2	617.7	21.1	447.3
C <sub>11</sub> H <sub>24</sub>	654.3	18.9	465.3	639.0	19.5	469.1
C <sub>12</sub> H <sub>26</sub>	668.4	17.4	475.9	658.0	18.2	489.5
C <sub>13</sub> H <sub>28</sub>	694.5	16.9	501.7	675.0	16.8	508.6
C <sub>14</sub> H <sub>30</sub>	701.1	15.0	526.5	693.0	15.7	526.7
C <sub>15</sub> H <sub>32</sub>	725.5	14.1	544.4	708.0	14.8	543.8
C <sub>16</sub> H <sub>34</sub>	733.4	13.5	557.7	723.0	14.0	560.1

Table B.6 Critical pressures ( $P_c$ ), critical temperatures ( $T_c$ ) and normal boiling temperatures ( $T_b$ ) of cycloalkanes. MD denotes Molecular Dynamics simulations and EXP represents experimental data.

	MD			EXP		
	$T_c$ [K]	$P_c$ [atm]	$T_b$ [K]	$T_c$ [K]	$P_c$ [atm]	$T_b$ [K]
C <sub>7</sub> H <sub>14</sub>	581.7	32.3	374.4	573.0	34.3	374.0
C <sub>8</sub> H <sub>16</sub>	621.6	28.2	390.4	609.0	30.0	405.0
C <sub>9</sub> H <sub>18</sub>	655.5	27.6	422.1	639.2	27.7	429.0
C <sub>10</sub> H <sub>20</sub>	679.0	25.7	451.9	667.0	25.4	453.0
C <sub>11</sub> H <sub>22</sub>	707.1	22.8	466.8			
C <sub>12</sub> H <sub>24</sub>	721.3	20.5	512.7			
C <sub>13</sub> H <sub>26</sub>	733.5	18.5	527.7			
C <sub>14</sub> H <sub>28</sub>	749.2	17.6	526.7			

Table B.7 Critical pressures ( $P_c$ ), critical temperatures ( $T_c$ ) and normal boiling temperatures ( $T_b$ ) of aromatic molecules. MD denotes Molecular Dynamics simulations and EXP represents experimental data.

	MD			EXP		
	$T_c$ [K]	$P_c$ [atm]	$T_b$ [K]	$T_c$ [K]	$P_c$ [atm]	$T_b$ [K]
C <sub>6</sub> H <sub>6</sub>	569.1	47.9	361.3	562.0	48.3	353.1
C <sub>10</sub> H <sub>8</sub>	763.5	38.9	489.5	748.0	40.5	490.0
C <sub>14</sub> H <sub>10</sub> -a	894.2	30.8	622.8	873.0	28.6	613.0
C <sub>14</sub> H <sub>10</sub> -b	894.8	30.8	622.1	869.0	28.6	609.2
C <sub>16</sub> H <sub>10</sub>	953.4	26.8	687.0	936.0	25.8	667.9
C <sub>18</sub> H <sub>12</sub> -a	996.7	24.0	731.2	987.0	23.6	716.2
C <sub>18</sub> H <sub>12</sub> -b	995.8	23.8	730.6			
C <sub>18</sub> H <sub>12</sub> -c	996.3	24.0	730.8			
C <sub>18</sub> H <sub>12</sub> -d	996.2	24.0	730.5			

Table B.8 L-J 12-6 potential parameters for linear alkanes obtained from MD simulations.

	$\sigma$ [Å]	$\epsilon/k_B$ [K]
CH <sub>4</sub>	3.771	154.9
C <sub>2</sub> H <sub>6</sub>	4.515	227.9
C <sub>3</sub> H <sub>8</sub>	4.915	315.6
C <sub>4</sub> H <sub>10</sub>	5.314	356.3
C <sub>5</sub> H <sub>12</sub>	5.648	425.2
C <sub>6</sub> H <sub>14</sub>	5.993	457.1
C <sub>7</sub> H <sub>16</sub>	6.288	513.6
C <sub>8</sub> H <sub>18</sub>	6.311	629.8
C <sub>9</sub> H <sub>20</sub>	6.637	649.6
C <sub>10</sub> H <sub>22</sub>	6.997	681.2
C <sub>11</sub> H <sub>24</sub>	7.184	685.0
C <sub>12</sub> H <sub>26</sub>	7.482	688.9
C <sub>13</sub> H <sub>28</sub>	7.591	738.1
C <sub>14</sub> H <sub>30</sub>	7.719	820.1
C <sub>15</sub> H <sub>32</sub>	7.884	840.2
C <sub>16</sub> H <sub>34</sub>	8.064	869.9

Table B.9 L-J 12-6 potential parameters for cycloalkanes obtained from MD simulations.

	$\sigma$ [Å]	$\epsilon/k_B$ [K]
C <sub>7</sub> H <sub>14</sub>	5.997	532.6
C <sub>8</sub> H <sub>16</sub>	6.417	540.7
C <sub>9</sub> H <sub>18</sub>	6.629	578.7
C <sub>10</sub> H <sub>20</sub>	6.766	638.6
C <sub>11</sub> H <sub>22</sub>	7.142	666.3
C <sub>12</sub> H <sub>24</sub>	7.197	770.7
C <sub>13</sub> H <sub>26</sub>	7.520	774.9
C <sub>14</sub> H <sub>28</sub>	7.725	779.2

Table B.10 L-J 12-6 potential parameters for aromatic molecules obtained from MD simulations.

	$\sigma$ [Å]	$\epsilon/k_B$ [K]
C <sub>6</sub> H <sub>6</sub>	5.149	550.9
C <sub>10</sub> H <sub>8</sub>	6.115	724.5
C <sub>14</sub> H <sub>10</sub> -a	6.667	1001.2
C <sub>14</sub> H <sub>10</sub> -b	6.678	999.4
C <sub>16</sub> H <sub>10</sub>	6.966	1149.0
C <sub>18</sub> H <sub>12</sub> -a	7.256	1240.2
C <sub>18</sub> H <sub>12</sub> -b	7.277	1237.7
C <sub>18</sub> H <sub>12</sub> -c	7.257	1239.4
C <sub>18</sub> H <sub>12</sub> -d	7.255	1238.8

### C. Supplementary tables of chapter 4

Tables C.1 to C.14 list reaction rates constants.

$F$  denotes forward reaction and  $R$  represents reverse reaction,  $E_a$  [kcal/mol] is the activation energy of each reaction.

Arrhenius format,  $k(T) = AT^n \exp(-E_a/RT)$ ,

Table C.1 The reaction rate constants of pathway 1.

	Reaction	Direction	Arrhenius constants		
			A	n	$E_a$
1-1		F	2.671E+12	0.31573	18.707
		R	7.925E+11	0.33150	27.450
1-2		F	5.752E+14	-0.30744	42.923
		R	1.235E+12	-0.37251	25.155
1-3		F	9.057E+11	-0.11915	17.029
		R	1.082E+12	-0.08198	40.868
1-4		F	1.844E+16	-0.28498	48.546
		R	1.257E+13	-0.30436	19.868
1-5		F	2.113E+12	0.28600	13.756
		R	3.513E+12	0.30680	34.454
1-6		F	1.623E+13	0.33178	35.400
		R	5.800E+12	0.29452	14.407
1-7		F	2.297E+12	0.25650	11.764
		R	4.517E+12	0.28643	45.063
1-8		F	2.338E+11	0.10499	11.868
		R	1.817E+12	0.31475	94.098



Table C.2 The reaction rate constants of pathway 2.

	Reaction	Direction	Arrhenius constants		
			A	n	E <sub>a</sub>
	<i>From '1-5' reaction</i>				
2-6		F	9.972E+10	0.12649	12.718
		R	1.790E+12	0.29685	76.410
2-7		F	1.209E+13	0.21989	9.815
		R	5.013E+13	0.28842	58.179
2-8		F	8.112E+12	0.32867	31.255
		R	5.949E+11	0.29221	13.738

Table C.3 The reaction rate constants of pathway 3.

	Reaction	Direction	Arrhenius constants		
			A	n	E <sub>a</sub>
	<i>From '1-2' reaction</i>				
3-3		F	1.258E+15	-0.30286	39.263
		R	6.522E+12	-0.31250	23.283
3-4		F	2.615E+14	-0.24370	28.612
		R	5.852E+12	-0.21731	29.665
3-5		F	1.622E+11	0.16830	11.370
		R	4.161E+12	0.32652	66.643
3-6		F	5.007E+12	0.25421	11.081
		R	1.480E+13	0.28425	45.005
3-7		F	1.504E+11	0.12669	11.123
		R	2.425E+13	0.33921	93.567

Table C.4 The reaction rate constants of pathway 4.

	Reaction	Direction	Arrhenius constants		
			A	n	E <sub>a</sub>
	From '3-3' reaction				
4-4		F	1.944E+10	0.14242	12.420
		R	7.473E+11	0.33513	83.036
4-5		F	5.392E+11	0.31820	17.638
		R	4.671E+11	0.33086	24.758
4-6		F	9.172E+10	0.12427	14.298
		R	2.574E+12	0.29891	85.560
4-7		F	3.511E+12	0.24637	11.979
		R	1.091E+13	0.29287	45.581
4-8		F	5.865E+10	0.12088	10.727
		R	1.701E+12	0.32594	99.985

Table C.5 The reaction rate constants of pathway 5.

	Reaction	Direction	Arrhenius constants		
			A	n	E <sub>a</sub>
	From '4-5' reaction				
5-6		F	6.387E+14	-0.16959	41.826
		R	8.166E+12	-0.17896	16.490
	To '3-6' reaction				

Table C.6 The reaction rate constants of pathway 6.

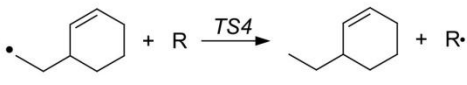
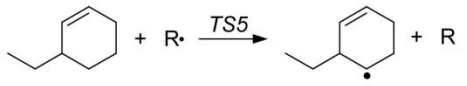
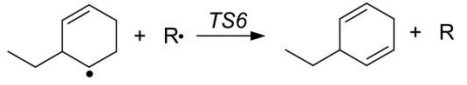
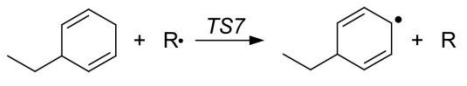

	Reaction	Direction	Arrhenius constants		
			A	n	E <sub>a</sub>
	From '3-3' reaction				
6-4		F	7.281E+11	0.32328	24.201
		R	2.380E+12	0.32214	18.693
6-5		F	6.431E+11	0.31917	17.906
		R	5.307E+11	0.33619	26.427
6-6		F	9.978E+10	0.12523	14.525
		R	2.252E+12	0.29925	85.758
6-7		F	2.668E+12	0.24728	12.266
		R	8.563E+12	0.29549	46.118
6-8		F	3.606E+10	0.11008	11.290
		R	1.131E+12	0.30724	96.707

Table C.7 The reaction rate constants of pathway 7.

	Reaction	Direction	Arrhenius constants		
			A	n	E <sub>a</sub>
From '1-1' reaction					
7-2		F	1.230E+15	-0.29374	44.091
		R	3.660E+12	-0.35229	18.991
7-3		F	2.214E+15	-0.31624	37.454
		R	6.552E+12	-0.31085	24.817
7-4		F	1.223E+15	-0.20230	42.283
		R	2.343E+13	-0.21973	18.759
7-5		F	2.252E+12	0.31905	16.259
		R	1.037E+12	0.32647	25.016
7-6		F	1.045E+11	0.12735	13.552
		R	9.816E+12	0.30235	84.666
7-7		F	1.156E+13	0.24735	11.250
		R	2.126E+13	0.28685	45.243
7-8		F	1.862E+11	0.09502	11.117
		R	3.072E+12	0.30608	93.587

Table C.8 The reaction rate constants of pathway 8.

	Reaction	Direction	Arrhenius constants		
			A	n	E <sub>a</sub>
From '7-3' reaction					
8-4		F	8.925E+10	0.13348	13.312
		R	5.123E+12	0.30551	87.110
To '4-5' reaction					

Table C.9 The reaction rate constants of pathway 9.

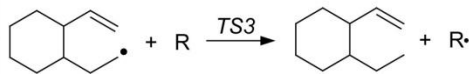
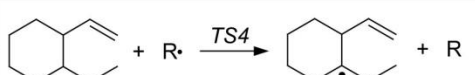
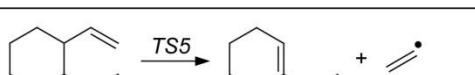
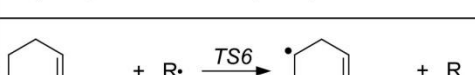


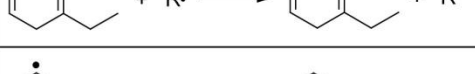
	Reaction	Direction	Arrhenius constants		
			A	n	E <sub>a</sub>
	<i>From '7-2' reaction</i>				
9-3		F	9.828E+11	0.32043	25.652
		R	1.929E+12	0.31914	19.627
9-4		F	3.366E+11	0.30187	18.218
		R	5.333E+10	0.32231	32.825
9-5		F	9.315E+14	-0.28587	43.495
		R	1.160E+13	-0.30492	19.909
9-6		F	1.212E+12	0.31916	17.378
		R	1.116E+12	0.32493	26.208
9-7		F	1.056E+11	0.12633	14.497
		R	1.780E+12	0.30174	85.560
9-8		F	2.726E+12	0.24500	12.283
		R	1.289E+13	0.28117	46.813
9-9		F	9.406E+10	0.10393	10.380
		R	1.243E+12	0.31491	90.885

Table C.10 The reaction rate constants of pathway 10.

	Reaction	Direction	Arrhenius constants		
			A	n	E <sub>a</sub>
10-1		F	7.010E+12	0.31069	18.280
		R	1.317E+12	0.23602	26.546
10-2		F	9.051E+14	-0.30982	46.118
		R	5.010E+12	-0.36605	20.744
10-3		F	7.004E+11	0.33509	25.433
		R	1.478E+12	0.32234	19.883
10-4		F	4.661E+11	0.29960	17.123
		R	2.073E+11	0.31290	31.692
10-5		F	4.730E+14	-0.30610	25.850
		R	6.124E+12	-0.30189	31.652
10-6		F	1.246E+12	0.31506	16.851
		R	1.080E+12	0.32187	25.612
10-7		F	1.152E+11	0.12698	13.897
		R	2.844E+12	0.30224	85.182
10-8		F	5.596E+12	0.24484	11.765
		R	1.822E+13	0.28487	46.257
10-9		F	1.691E+11	0.07343	9.980
		R	8.630E+11	0.28355	90.686

Table C.11 The reaction rate constants of pathway 11.

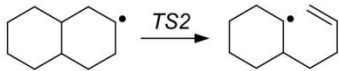
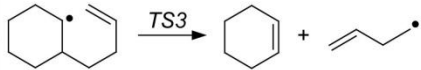
	Reaction	Direction	Arrhenius constants		
			A	n	E <sub>a</sub>
	From '10-1' reaction				
11-2		F	4.693E+14	-0.31601	42.919
		R	1.278E+12	-0.37025	22.910
11-3		F	7.389E+14	-0.29418	37.117
		R	1.079E+12	-0.30405	26.804
	To '7-5' reaction				

Table C.12 The reaction rate constants of pathway 12.

	Reaction	Direction	Arrhenius constants		
			A	n	E <sub>a</sub>
12-1		F	7.190E+11	0.29892	17.042
		R	1.183E+12	0.32814	32.487
12-2		F	2.189E+15	-0.28067	42.939
		R	1.598E+12	-0.34842	17.932
12-3		F	1.291E+15	-0.30703	39.402
		R	1.599E+13	-0.32284	23.704
12-4		F	6.154E+11	0.32422	24.261
		R	2.057E+12	0.32235	18.701
12-5		F	5.616E+11	0.30409	16.408
		R	1.469E+11	0.32753	42.124
12-6		F	5.769E+10	0.12463	17.823
		R	5.271E+12	0.29789	78.665
12-7		F	2.229E+12	0.28517	14.395
		R	4.000E+12	0.30761	35.229
12-8		F	9.545E+10	0.12968	12.774
		R	1.702E+12	0.29818	76.737
12-9		F	4.134E+12	0.21851	10.374
		R	1.377E+13	0.28536	58.378
12-10		F	8.226E+12	0.33200	32.249
		R	4.944E+12	0.29090	14.773



Table C.13 The reaction rate constants of pathway 13.

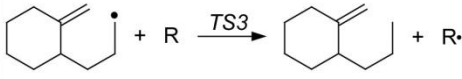
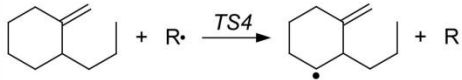
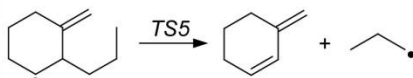
	Reaction	Direction	Arrhenius constants		
			A	n	E <sub>a</sub>
	From '12-2' reaction				
13-3		F	5.154E+11	0.32096	24.976
		R	1.457E+12	0.31932	19.550
13-4		F	5.245E+11	0.31123	18.179
		R	3.129E+11	0.33032	26.725
13-5		F	1.260E+15	-0.28112	33.779
		R	9.701E+11	-0.29149	26.387
	To '1-5' reaction				

Table C.14 Calculated product yields (%) of benzene, toluene, styrene, ethylbenzene, and xylene as a function of temperature

	Species		Temperature (K)								
			700	800	900	1000	1100	1200	1300	1400	1500
Relative yields of products	Benzene ( $C_6H_6$ )		93.73	84.18	70.81	68.42	71.37	75.13	78.79	81.91	84.68
	Toluene ( $C_7H_8$ )		6.25	15.81	29.17	31.47	28.44	24.60	20.86	17.64	14.78
	Styrene ( $C_8H_8$ )		0.02	0.0004	~ 0	~ 0	~ 0	~ 0	~ 0	~ 0	~ 0
	Ethylbenzene ( $C_8H_{10}$ )		~ 0	~ 0	~ 0	~ 0	~ 0	~ 0	~ 0	~ 0	~ 0
	Xylene ( $C_8H_{10}$ )		~ 0	0.0006	0.02	0.11	0.19	0.27	0.35	0.45	0.54
Contribution of each pathways to the products	Benzene	Path 3	0.03	0.13	0.41	1.03	2.01	3.33	4.91	6.70	8.55
		Path 5	~ 0	~ 0	~ 0	~ 0	~ 0	~ 0	~ 0	~ 0	~ 0
		Path 7	0.26	1.12	2.93	5.95	9.07	11.52	13.10	14.10	14.69
		Path 11	99.71	98.75	96.66	93.02	88.92	85.15	81.99	79.20	76.76
	Toluene	Path 1	0.71	9.60	20.69	31.55	39.74	47.59	55.40	62.05	67.83
		Path 2	99.29	91.40	79.31	68.45	60.26	52.41	44.60	37.95	32.17
		Path 10	~ 0	~ 0	~ 0	~ 0	~ 0	~ 0	~ 0	~ 0	~ 0
		Path 13	~ 0	~ 0	~ 0	~ 0	~ 0	~ 0	~ 0	~ 0	~ 0
		Path 14	~ 0	~ 0	~ 0	~ 0	~ 0	~ 0	~ 0	~ 0	~ 0
	Styrene	Path 4	~ 0	~ 0	~ 0	~ 0	~ 0	~ 0	~ 0	~ 0	~ 0
		Path 8	100	100	100	100	100	100	100	100	100
	Ethylbenzene	Path 6	0.49	0.99	1.45	2.02	2.80	3.94	5.54	7.45	9.58
		Path 9	99.51	99.01	98.55	97.98	97.20	96.06	94.46	92.55	90.42
	Xylene	Path 12	100	100	100	100	100	100	100	100	100

## References

- [1] A. T. Holley, Y. Dong, M. G. Andac, F. N. Egolfopoulos, T. Edwards *Proc. Combust. Inst.* **2007**, 31, 1205-1213.
- [2] J. A. Cooke, M. Bellucci, M. D. Smooke, A. Gomez, A. Violi, T. Faravelli, E. Ranzi *Proc. Combust. Inst.* **2005**, 30, 439-446.
- [3] T. Edwards, L. Q. Maurice *Journal of Propulsion and Power.* **2001**, 17, 461-466.
- [4] J. T. Farrell, N. P. Cernansky, F. L. Dryer, D. G. Friend, H. C. A., C. K. LAw, R. M. McDavid, M. C. J., A. K. Patel, H. Pitsch *SAE international.* **2007**.
- [5] A. Violi, S. Yan, E. G. Eddings, F. Sarofim, S. Granata, T. Faravelli, E. Ranzi *Combustion Science and Technology.* **2002**, 174, 399-417.
- [6] M. Colket, T. Edwards, S. Williams, N. P. Cemansky, D. L. Miller, F. Egolfopoulos, P. Lindstedt, K. Seshadri, F. L. Dryer, C. K. LAw, D. Friend, D. B. Lenhert, H. Pitsch, A. Sarofim, M. Smooke, W. Tsang *45th AIAA Aerospace Science Meeting.* **2007**, AIAA-2007-0770.
- [7] A. T. Ingemarsson, J. R. Pedersen, J. O. Olsson *Journal of Physical Chemistry A.* **1999**, 103, 8222-8230.

- [8] H. R. Zhang, E. G. Eddings, A. F. Sarofim, C. K. Westbrook *Energy & Fuels*. **2007**, 21, 1967-1976.
- [9] V. Calemme, S. Peratello, F. Stroppa, R. Giardino, C. Perego *Industrial & Engineering Chemistry Research*. **2004**, 43, 934-940.
- [10] W. Vincenti, C. H. J. Kruger *Introduction to physical gas dynamics*. **1975**.
- [11] J. Millat, J. H. Dymond, C. A. N. d. Castro, Transport Properties of Fluids: Their correlation, prediction and estimation, Cambridge university press, **1996**.
- [12] K. K. Kuo, Principles of Combustion, John Wiley & Sons, **1986**.
- [13] S. R. Turns, An Introduction to Combustion: Concepts and Applications, McGraw-Hill, **2000**.
- [14] B. J. Alder, D. M. Gass, Wainwrig.Te *Journal of Chemical Physics*. **1970**, 53, 3813
- [15] T. R. Marrero, E. A. Mason *Aiche Journal*. **1973**, 19, 498-503.
- [16] W. A. Wakeham, D. H. Slater *Journal of Physics B-Atomic Molecular and Optical Physics*. **1973**, 6, 886-896.
- [17] D. M. Heyes *Physical Review B*. **1988**, 37, 5677-5696.
- [18] H. Wang, M. Frenklach *Combustion and Flame*. **1994**, 96, 163-170.
- [19] D. Gavril, K. R. Atta, G. Karaiskakis *Fluid Phase Equilibria*. **2004**, 218, 177-188.

- [20] G. Karaiskakis, D. Gavril *Journal of Chromatography A*. **2004**, 1037, 147-189.
- [21] R. C. Reid, J. M. Prausnitz, B. E. Poling, *The Properties of Gases and Liquids*, McGraw-Hill, **1987**.
- [22] B. A. Williams *Combustion and Flame*. **2001**, 124, 330-333.
- [23] A. Ern, V. Giovangigli *Combustion Science and Technology*. **1999**, 149, 157-181.
- [24] P. Middha, B. H. Yang, H. Wang *Proc. Combust. Inst.* **2002**, 29, 1361-1369.
- [25] Y. F. Dong, A. T. Holley, M. G. Andac, F. N. Egolfopoulos, S. G. Davis, P. Middha, H. Wang *Combustion and Flame*. **2005**, 142, 374-387.
- [26] A. T. Holley, Y. Dong, M. G. Andac, F. N. Egolfopoulos *Combustion and Flame*. **2006**, 144, 448-460.
- [27] A. T. Holley, X. Q. You, E. Dames, H. Wang, F. N. Egolfopoulos *Proc. Combust. Inst.* **2009**, 32, 1157-1163.
- [28] C. S. McEnally, D. M. Ciuparu, L. D. Pfefferle *Combustion and Flame*. **2003**, 134, 339-353.
- [29] K. C. Hunter, A. L. L. East *Journal of Physical Chemistry A*. **2002**, 106, 1346-1356.
- [30] J. A. Miller, R. J. Kee, C. K. Westbrook *Annual Review of Physical Chemistry*. **1990**, 41, 345-387.

- [31] N. M. Marinov, W. J. Pitz, C. K. Westbrook, A. E. Lutz, A. M. Vincitore, S. M. Senkan, Chemical kinetic modeling of a methane opposed-flow diffusion flame and comparison to experiments, **1998**.
- [32] S. M. Hsu, C. I. Chen *Tribology Letters*. **2003**, 14, 91-97.
- [33] E. J. Silke, W. J. Pitz, C. K. Westbrook, M. Ribaucour *Journal of Physical Chemistry A*. **2007**, 111, 3761-3775.
- [34] T. Lu, C. K. Law *5th US combustion meeting*. **2007**.
- [35] K. E. Niemeyer, M. P. Raju, C. Sung *AIAA joint propulsion conference*. **2009**.
- [36] H. J. Curran, P. Gaffuri, W. J. Pitz, C. K. Westbrook *Combustion and Flame*. **1998**, 114, 149-177.
- [37] C. K. Westbrook, W. J. Pitz, H. J. Curran, J. Boercker, E. Kunrath *International Journal of Chemical Kinetics*. **2001**, 33, 868-877.
- [38] C. K. Westbrook, W. J. Pitz, J. E. Boercker, H. J. Curran, J. F. Griffiths, C. Mohamed, M. Ribaucour *Proc. Combust. Inst.* **2002**, 29, 1311-1318.
- [39] C. K. Westbrook, W. J. Pitz, O. Herbinet, H. J. Curran, E. J. Silke *Combustion and Flame*. **2009**, 156, 181-199.
- [40] Y. Sakai, A. Miyoshi, M. Koshi, W. J. Pitz *Proc. Combust. Inst.* **2009**, 32, 411-418.
- [41] W. J. Pitz, C. V. Naik, T. N. Mhaolduin, C. K. Westbrook, H. J. Curran, J. P. Orme, J. M. Simmie *Proc. Combust. Inst.* **2007**, 31, 267-275.

- [42] N. Taxman *Physical Review*. **1958**, 110, 1235-1239.
- [43] C. S. Wang Chang, G. E. Uhlenbeck *Michigan University Engineering Research Institute Report*. **1951**, CM-681.
- [44] L. Waldmann *Zeitschrift Fur Naturforschung Part a-Astrophysik Physik Und Physikalische Chemie*. **1957**, 12, 660-662.
- [45] R. F. Snider *Journal of Chemical Physics*. **1960**, 32, 1051-1060.
- [46] L. Monchick, E. A. Mason *Journal of Chemical Physics*. **1961**, 35, 1676.
- [47] R. C. Reid, J. M. Prausnitz, T. K. Sherwood, *The Properties of Gases and Liquids*, 4th ed., McGraw-Hill, New York, **1987**.
- [48] L. S. Tee, S. Gotoh, W. E. Stewart *Industrial & Engineering Chemistry Fundamentals*. **1966**, 5, 356.
- [49] B. I. Lee, M. G. Kesler *Aiche Journal*. **1975**, 21, 510-527.
- [50] R. Kubo *Journal of the Physical Society of Japan*. **1957**, 12, 570-586.
- [51] R. Kubo, M. Yokota, S. Nakajima *Journal of the Physical Society of Japan*. **1957**, 12, 1203-1211.
- [52] R. Zwanzig *Annual Review of Physical Chemistry*. **1965**, 16, 67.
- [53] D. Chandler, *Introduction to modern statistical mechanics*, Oxford University Press, New York, **1987**.

- [54] R. Sharma, K. Tankeshwar *Journal of Chemical Physics*. **1998**, 108, 2601-2607.
- [55] Y. H. Zhou, G. H. Miller *Journal of Physical Chemistry*. **1996**, 100, 5516-5524.
- [56] A. Olivet, L. F. Vega *Journal of Physical Chemistry C*. **2007**, 111, 16013-16020.
- [57] J. M. Stoker, R. L. Rowley *Journal of Chemical Physics*. **1989**, 91, 3670-3676.
- [58] M. G. Martin, J. I. Siepmann *Journal of Physical Chemistry B*. **1999**, 103, 4508-4517.
- [59] S. K. Nath, J. J. De Pablo *Molecular Physics*. **2000**, 98, 231-238.
- [60] J. R. Errington, A. Z. Panagiotopoulos *Journal of Physical Chemistry B*. **1999**, 103, 6314-6322.
- [61] G. D. Smith, D. Y. Yoon *Journal of Chemical Physics*. **1994**, 100, 649-658.
- [62] J. Chang, J. Han, L. Yang, R. L. Jaffe, D. Y. Yoon *Journal of Chemical Physics*. **2001**, 115, 2831-2840.
- [63] W. L. Jorgensen, D. S. Maxwell, J. TiradoRives *Journal of the American Chemical Society*. **1996**, 118, 11225-11236.
- [64] J. Petravac, J. Delhommelle *Chemical Physics*. **2003**, 286, 303-314.
- [65] L. Zhang, Q. Wang, Y. C. Liu, L. Z. Zhang *Journal of Chemical Physics*. **2006**, 125.
- [66] Q. Y. Yang, C. Y. Xue, C. L. Zhong, J. F. Chen *Aiche Journal*. **2007**, 53, 2832-2840.



- [67] M. L. P. Price, D. Ostrovsky, W. L. Jorgensen *Journal of Computational Chemistry*. **2001**, 22, 1340-1352.
- [68] L. L. Thomas, T. J. Christakis, W. L. Jorgensen *Journal of Physical Chemistry B*. **2006**, 110, 21198-21204.
- [69] H. A. Lorentz *Ann. der Phys. and Chemie*. **1881**, 12, 127.
- [70] D. C. R. Berthelot *Hebd. Seanc Acad. Sci.(Paris)*. **1898**, 126, 1703.
- [71] E. Lindahl, B. Hess, D. van der Spoel *Journal of Molecular Modeling*. **2001**, 7, 306-317.
- [72] S. Nose *Journal of Chemical Physics*. **1984**, 81, 511-519.
- [73] W. G. Hoover *Physical Review A*. **1985**, 31, 1695-1697.
- [74] D. Frenkel, B. Smit, Understanding molecular simulation; from algorithms to applications Academic press, **1996**.
- [75] G. Fernandez, J. Vrabec, H. Hasse *International Journal of Thermophysics*. **2005**, 26, 1389-1407.
- [76] J. A. Manion, W. S. McGivern *Combustion Institute 2008 spring technical meeting, Western states sections*. **2008**.
- [77] E. Grushka, Schnipel.P *Journal of Physical Chemistry*. **1974**, 78, 1428-1431.
- [78] E. Grushka, V. R. Maynard *Journal of Physical Chemistry*. **1973**, 77, 1437-1442.

- [79] M. Y. Lobanov, N. S. Bogatyreva, O. V. Galzitskaya *Molecular Biology*. **2008**, 42, 623-628.
- [80] A. J. Barrett, J. Skolnick *Macromolecules*. **1988**, 21, 1141-1145.
- [81] M. Costa, R. C. S. Dias *Polymer*. **2007**, 48, 1785-1801.
- [82] J. A. Manion, W. S. McGivern *6th US national combustion meeting*. **2009**.
- [83] E. D. B. Sirjean, D. A. Sheen, X.-Q. You, C. Sung, A. T. Holley, F. N. Egolfopoulos, H. Wang, S. S. Vasu, D. F. Davidson, R. K. Hanson, H. Pitsch, C. T. Bowman, A. Kelley, C. K. Law, W. Tsang, N. P. Cernansky, D. L. Miller, A. Violi, R. P. Lindstedt *A high-temperature chemical kinetic model of n-alkane oxidation, JetSurF version 0.2* , September 08, 2008. **2008**.
- [84] B. S. Haynes, H. G. Wagner *Progress in Energy and Combustion Science*. **1981**, 7, 229-273.
- [85] H. F. Calcote *Combustion and Flame*. **1981**, 42, 215-242.
- [86] C. D. Bruce, M. L. Berkowitz, L. Perera, M. D. E. Forbes *Journal of Physical Chemistry B*. **2002**, 106, 3788-3793.
- [87] E. A. Guggenheim *Journal of Chemical Physics*. **1945**, 13, 253-261.
- [88] P. Ungerer, C. Nieto-Draghi, B. Rousseau, G. Ahunbay, V. Lachet *Journal of Molecular Liquids*. **2007**, 134, 71-89.

- [89] A. Z. Panagiotopoulos *Molecular Physics*. **1987**, 61, 813-826.
- [90] D. Moller, J. Fischer *Molecular Physics*. **1990**, 69, 463-473.
- [91] I. Szalai, J. Liszi, D. Boda *Chemical Physics Letters*. **1995**, 246, 214-220.
- [92] I. Brovchenko, A. Geiger, A. Oleinikova *Journal of Chemical Physics*. **2005**, 123.
- [93] S. T. Cui, P. T. Cummings, H. D. Cochran *Fluid Phase Equilibria*. **1997**, 141, 45-61.
- [94] B. Smit, D. Frenkel *Journal of Chemical Physics*. **1991**, 94, 5663-5668.
- [95] H. Okumura, F. Yonezawa *Journal of Non-Crystalline Solids*. **2002**, 312, 256-259.
- [96] J. G. Kirkwood *Journal of Chemical Physics*. **1935**, 3, 300-313.
- [97] C. Chipot, A. Pohorille, Free energy calculations, Springer, New York, **2007**.
- [98] H. Hu, R. H. Yun, J. Hermans *Molecular Simulation*. **2002**, 28, 67-80.
- [99] B. Knopp, U. W. Suter, A. A. Gusev *Macromolecules*. **1997**, 30, 6107-6113.
- [100] B. Hess, C. Peter, T. Ozal, N. F. A. van der Vegt *Macromolecules*. **2008**, 41, 2283-2289.
- [101] T. C. Beutler, A. E. Mark, R. C. Vanschaik, P. R. Gerber, W. F. Vangunsteren *Chemical Physics Letters*. **1994**, 222, 529-539.
- [102] H. Flyvbjerg, H. G. Petersen *Journal of Chemical Physics*. **1989**, 91, 461-466.

- [103] B. Hess *Journal of Chemical Physics*. **2002**, 116, 209-217.
- [104] B. Smit, P. Desmedt, D. Frenkel *Molecular Physics*. **1989**, 68, 931-950.
- [105] J. V. Sengers, J. Sengers *Annual Review of Physical Chemistry*. **1986**, 37, 189-222.
- [106] J. H. Chen, M. E. Fisher, B. G. Nickel *Physical Review Letters*. **1982**, 48, 630-634.
- [107] S. Meyerson, A. W. Weitkamp *Organic Mass Spectrometry*. **1968**, 1, 659.
- [108] N. Hiyoshi, T. Inoue, C. Rode, O. Sato, M. Shirai *Catalysis Letters*. **2006**, 106, 133-138.
- [109] M. H. Gollis, L. I. Belenyessy, B. J. Gudzinowicz, S. D. Koch, J. O. Smith, R. J. Wineman *J. Chem. Eng. Data*. **1962**, 7, 311 - 316.
- [110] J. S. Heyne, A. L. Boehman, S. Kirby *Energy & Fuels*. **2009**, 23, 5879-5885.
- [111] H. Ogawa, T. Ibuki, T. Minematsu, N. Miyamoto *Energy & Fuels*. **2007**, 21, 1517-1521.
- [112] L. M. Balster, E. Corporan, M. J. DeWitt, J. T. Edwards, J. S. Ervin, J. L. Graham, S. Y. Lee, S. Pal, D. K. Phelps, L. R. Rudnick, R. J. Santoro, H. H. Schobert, L. M. Shafer, R. C. Striebich, Z. J. West, G. R. Wilson, R. Woodward, S. Zabarnick *Fuel Processing Technology*. **2008**, 89, 364-378.

- [113] E. Corporan, D. K. Minus, T. Williams *AIAA joint propulsion conference*. **1999**, 99-2213.
- [114] T. Edwards, W. Harrison, H. H. Schobert *33rd AIAA/ASME/SAE Joint Propulsion Conference and Exhibition*. **1997**, 97-2848.
- [115] L. Q. Maurice, H. Lander, T. Edwards, W. E. Harrison *Fuel*. **2001**, 80, 747-756.
- [116] J. Pajak, V. Krebs, J. F. Mareche, G. Furdin *Fuel Processing Technology*. **1996**, 48, 73-81.
- [117] J. Stewart, K. Brezinsky, I. Glassman *Combustion Science and Technology*. **1998**, 136, 373-390.
- [118] A. Agosta, N. P. Cernansky, D. L. Miller, T. Faravelli, E. Ranzi *Experimental Thermal and Fluid Science*. **2004**, 28, 701-708.
- [119] E. Ranzi *Energy & Fuels*. **2006**, 20, 1024-1032.
- [120] E. G. Eddings, S. H. Yan, W. Ciro, A. F. Sarofim *Combustion Science and Technology*. **2005**, 177, 715-739.
- [121] A. D. Becke *Journal of Chemical Physics*. **1992**, 96, 2155-2160.
- [122] A. D. Becke *Journal of Chemical Physics*. **1992**, 97, 9173-9177.
- [123] C. T. Lee, W. T. Yang, R. G. Parr *Physical Review B*. **1988**, 37, 785-789.
- [124] T. N. Truong, W. Duncan *Journal of Chemical Physics*. **1994**, 101, 7408-7414.

- [125] Q. Zhang, R. Bell, T. N. Truong *Journal of Physical Chemistry*. **1995**, 99, 592-599.
- [126] A. Violi, T. N. Truong, A. F. Sarofim *Journal of Physical Chemistry A*. **2004**, 108, 4846-4852.
- [127] L. K. Huynh, A. Ratkiewicz, T. N. Truong *Journal of Physical Chemistry A*. **2006**, 110, 473-484.
- [128] D. Wang, A. Violi, D. H. Kim, J. A. Mullholland *Journal of Physical Chemistry A*. **2006**, 110, 4719-4725.
- [129] M. J. T. Frisch, G. W.; Schlegel, H. B.; Scuseria, G. E.; Robb, J. R. M. M. A.; Cheeseman, J. A., Jr.; T. V.; Kudin, K. N.; J. C. M. Burant, J. M.; Iyengar, S. S.; Tomasi, J.; Barone, V.; B. C. Mennucci, M.; Scalmani, G.; Rega, N.; Petersson, G. A.; H. H. Nakatsuji, M.; Ehara, M.; Toyota, K.; Fukuda, R.; Hasegawa, J.; M. N. Ishida, T.; Honda, Y.; Kitao, O.; Nakai, H.; Klene, M.; Li, J. E. H. X.; Knox, H. P.; Cross, J. B.; Adamo, C.; Jaramillo, J.; R. S. Gomperts, R. E.; Yazyev, O.; Austin, A. J.; Cammi, R.; C. O. Pomelli, J. W.; Ayala, P. Y.; Morokuma, K.; Voth, G. A.; P. D. Salvador, J. J.; Zakrzewski, V. G.; Dapprich, S.; Daniels, M. C. F. A. D.; Strain, O.; Malick, D. K.; Rabuck, A. D.; K. F. Raghavachari, J. B.; Ortiz, J. V.; Cui, Q.; Baboul, A. G.; S. C. Clifford, J.; Stefanov, B. B.; Liu, G.; Liashenko, A.; Piskorz, I. M. P.; Komaromi, R. L.; Fox, D. J.; Keith, T.; Al-Laham, M. A.; C. Y. N. Peng, A.; Challacombe, M.; Gill, P. M. W.; Johnson, W. W. B.; Chen, M. W.; Gonzalez, C.; Pople, J. A. *Gaussian 03 Revision A.1*. **2003**, Gaussian, Inc.
- [130] S. Glasstone, L. K. J., H. Eyring, *The theory of rate processes*, McGraw-Hill, New York, **1941**.

- [131] W. Frost, *Theory of Unimolecular Reactions*, Academic Press, New York, **1973**.
- [132] D. G. Truhlar, B. C. Garrett, S. J. Klippenstein *Journal of Physical Chemistry*. **1996**, 100, 12771-12800.
- [133] T. N. Truong, M. Nayak, H. H. Huynh, T. Cook, P. Mahajan, L. T. Tran, J. Bharath, S. Jain, H. B. Pham, C. Boonyasirawat, N. Nguyen, E. Andersen, Y. Kim, S. Choe, J. Choi, T. E. Cheatham, J. C. Facelli *Journal of Chemical Information and Modeling*. **2006**, 46, 971-984.
- [134] W. H. Miller *Journal of the American Chemical Society*. **1979**, 101, 6810-6814.
- [135] W. Hillebrand, W. Hodek, G. Kolling *Fuel*. **1984**, 63, 756-761.
- [136] B. Ondruschka, G. Zimmermann, M. Remmler, M. Sedlackova, J. Pola *Journal of Analytical and Applied Pyrolysis*. **1990**, 18, 19-32.
- [137] B. Ondruschka, G. Zimmermann, U. Ziegler *Journal of Analytical and Applied Pyrolysis*. **1990**, 18, 33-39.
- [138] F. Billaud, P. Chaverot, E. Freund *Journal of Analytical and Applied Pyrolysis*. **1987**, 11, 39-53.
- [139] A. E. Lutz, R. J. Kee, J. A. Miller *SENKIN: A Fortran program for predicting homogeneous gas phase chemical kinetics with sensitivity analysis; Sandia National Laboratories Report No. SAND-87-8248; Sandia National Laboratories: Albuquerque, NM*. **1988**.

[140] R. J. Kee, F. M. Rupley, J. A. Miller *CHEMKIN 2: A Fortran Chemical kinetics Package for the analysis of gas phase chemical kinetics; Sandia National Laboratories Report No. SAND-89-8009B; Sandia National Laboratories: Albuquerque, NM. 1989.*